A Microreactor System for High-Pressure, Multiphase Homogeneous and Heterogeneous Catalyst Measurements under Continuous Flow

By

Jaroslav Keybl

B. S. in Eng. Chemical Engineering, University of Pennsylvania (2006)
B. S. in Econ. Finance, the Wharton School at the University of Pennsylvania (2006)

Submitted to the Department of Chemical Engineering
in partial fulfillment of the requirements for the degree of
Doctor of Philosophy in Chemical Engineering
at the

Massachusetts Institute of Technology

September 2011

Author ....
Jaroslav Keybl
Department of Chemical Engineering
September 1, 2011

Certified by ....
Klavs F. Jensen
Department Head, Chemical Engineering
Warren K. Lewis Professor of Chemical Engineering
Professor of Materials Science and Engineering
Thesis Supervisor

Accepted by ....
William M. Deen
Carbon P. Dubbs Professor of Chemical Engineering
Chairman, Committee for Graduate Students

A Microreactor System for High-Pressure, Multiphase Homogeneous and Heterogeneous Catalyst Measurements under Continuous Flow

by
Jaroslav Keybl

Submitted to the Department of Chemical Engineering
on September 1, 2011 in partial fulfillment of the requirements
for the degree of Doctor of Philosophy in Chemical Engineering

Abstract

The shift towards biomass and lower quality fossil fuel feedstocks will require new conversion approaches. Catalysis will be critical in the processing of these new feedstocks. By studying catalysis at industrially relevant conditions, it may be possible to reduce the time and cost of developing new catalyst systems. Microreactors enable the study of multiphase catalyst systems at pressures that were previously difficult to attain on the laboratory scale. The reduced length scales, characteristic of microchemical systems, provide additional benefits such as enhanced heat and mass transfer and a reduction of hazardous waste. The improved heat and mass transfer allow for kinetics to be probed at isothermal conditions in the absence of complicating mass transfer effects.

A high-pressure microreactor system for catalyst study was designed, fabricated, and tested. The system allows for the multiphase study of homogenously and heterogeneously catalyzed systems, with a unique reactor designed for each application. A multicomponent gas phase is delivered simultaneously with a liquid stream, resulting in regular segmented (slug) flow. The isobaric system is operated at pressures of up to 100 bar. Gas and liquid flow rates, and therefore residence time, are specified independently of pressure. The system is capable of being operated at temperatures of up to 350 °C and residence times of up to 15 minutes. Inline analysis, using an attenuated total reflection FTIR flow cell, and sample collection for offline analysis can be performed simultaneously.

Both homogeneous and heterogeneous catalysis were demonstrated in the high-pressure system. A kinetic expression was derived for the homogeneous hydroformylation of terminal alkenes, catalyzed by Wilkinson's catalyst. The empirical reaction orders for the dependence on catalyst, hydrogen, and carbon monoxide were determined, along with the activation energy and pre-exponential factor. These results were then reconciled with a mechanistic model. The hydrogenation of cyclohexene over platinum catalysts was chosen to demonstrate the performance of the heterogeneous reactor. This reaction proceeded rapidly allowing mass transfer to be characterized in the microreactor. Observed mass transfer rates were two orders of magnitude higher than in traditional systems.

Thesis Supervisor:	Klavs F. Jensen
Title:	Department Head, Chemical Engineering Warren K. Lewis Professor of Chemical Engineering Professor of Materials Science and Engineering

Acknowledgments

Without the support, guidance, and encouragement of my advisor, Professor Klavs Jensen, this thesis would not have been possible. On countless occasions, I came to Klavs looking for advice about a particular problem. He had the uncanny ability to have just the right resource to help answer my question. Typically, he would walk to his massive wall of books and theses, select one, thumb to the correct page, and hand it to me with a smile. I will miss this support.

I would also like to thank my thesis committee members, Professors William Green and Christopher Cummins, for their insightful comments and suggestions. Their input has strengthened my kinetic analysis. I am also grateful to the staff of the Microsystems Technology Laboratory for their assistance with microfabrication. In particular, Dennis Ward, Bob Biccheiri, and Donal Jamieson have provided invaluable instruction and support during fabrication.

I thank BP for providing funding for this research. In particular, I have enjoyed my conversations with Dr. Sander Gaemers, Dr. George Huff, and Dr. Drew Braden at all points in the research. In addition, I am grateful to Randall Fields for coordinating the program.

I am deeply indebted to the students and postdoctoral researchers in the Jensen group. The depth and breadth of knowledge in the group has been impressive and exceedingly valuable. In particular, I would like to thank Dr. Bariş Ünal for his suggestions during the heterogeneous microreactor design and fabrication phases as well as his aid in performing the pulse chemisorption experiments. Dr. Christopher Martin was tremendously helpful during our frequent conversations and by always being willing to lend a hand. I would also like to thank Dr. Samuel Marre for his early guidance in operating high-pressure silicon reactors. In addition, I would like to thank Dr. Andrea Adamo, Dr. Chris Smith, Jason Moore, Dr. Lei Gu, Patrick Heider, Dr. Soubir Basak, Kevin Nagy, Tanya Shatova, and Vicki Dydek for their support as colleagues and friends.

During my time at MIT, I have made a number of great friends who I would like to acknowledge: David and Becky, CJ and Stef, Kevin and Sara, Diana and Trevor, Jordi and Becca, Nate, Mahriah, Anita, Kevin, Ben, and Ken. You all have made my time at MIT about more than just school.

I dedicate this thesis to my wife Meredith, who has provided me with never ending love, encouragement, and joy. I would also like thank my parents, Jaroslav and Alina, and brother, Alex, for their support and love throughout my life.

Table of Contents

Chapter 1. Introduction 17
- 1.1. Alternate Energy Sources will Require New Catalyst Approaches 17
- 1.2. Laboratory-based Research and Development 19
  - 1.2.1. New Compound Discovery 20
  - 1.2.2. Parameter Screening 21
  - 1.2.3. Kinetic Study 21
  - 1.2.4. Understanding Chemical Mechanisms 22
- 1.3. Historic Methods for Catalyst Screening 22
  - 1.3.1. Common System Limitations 23
  - 1.3.2. Addressing Pressure Limitations 25
- 1.4. Microreactors 28
  - 1.4.1. Overview 28
  - 1.4.2. Material Considerations 29
  - 1.4.3. Benefits Realized in Silicon Microreactors 31
    - 1.4.3.1. Mass Transport 31
    - 1.4.3.2. High Pressure 32
    - 1.4.3.3. Heat Transfer and High Temperature Operation 33
    - 1.4.3.4. Improved Safety 33
    - 1.4.3.5. Continuous Operation 34
  - 1.4.4. Microreactor Applications 34
- 1.5. Motivation 36
- 1.6. Thesis Objectives and Overview 39

Chapter 2. Microreactor Design and Construction 41
- 2.1. Segmented Flow 41
  - 2.1.1. Formation 42
  - 2.1.2. Mixing and Residence Time Distribution 45
  - 2.1.3. Stability of Segmented Flow 48
  - 2.1.4. Mass Transfer Model 51
- 2.2. Gas-Liquid Flow over Packed Beds 52
  - 2.2.1. Micro Packed Beds 53

2.2.2. Mass Transfer Model 56
2.3. Microreactor Designs 57
2.3.1. Homogeneous Reactors 57
2.3.1.1. Initial Design 57
2.3.1.2. Initial Reactor Performance 62
2.3.1.3. Redesigned Reactor 66
2.3.1.4. Second Generation Reactor Performance 68
2.3.2. Heterogeneous Reactors 69
2.3.2.1. Initial Design 69
2.3.2.2. Initial Reactor Performance 71
2.3.2.3. Second Generation Heterogeneous Reactor 72
2.3.2.4. Second Generation Reactor Performance 76
2.4. Reactor Fabrication 77
Chapter 3. System Components and Construction 81
3.1. Requirements 81
3.2. Overall System Design 82
3.3. Pressure Control System 83
3.4. Gas Handling System 86
3.5. Liquid Handling System 90
3.6. Microreactor Fluidic Connections 92
3.7. Temperature Control 95
3.8. Gas-Liquid Separation 98
3.9. Offline Sampling 102
3.10. Computer Control 105
3.11. System Enclosure 106
Chapter 4. System Operation and Analytics 110
4.1. Experimental Preparation 110
4.1.1. Gas Mixtures 111
4.1.2. Liquid Mixtures 112
4.1.3. Solid Catalyst Loading 114
4.1.4. Reactor Packaging 115

4.2. Experimental Operation 116
4.3. Analytics 118
4.3.1. Inline – Fourier Transform Infrared Spectroscopy 118
4.3.1.1. Operation 121
4.3.1.2. Analytic Approaches 122
4.3.1.3. Gas-Liquid Effects 129
4.3.2. Offline – Gas Chromatography and Sample Collection 131
4.3.2.1. Sample Crossover during Collection 133
Chapter 5. Homogeneous Catalysis – Hydroformylation 135
5.1. Introduction and Reaction Literature 135
5.2. Experimental 139
5.2.1. Analytic Considerations 140
5.3. Kinetic Results of Hydroformylation 144
5.3.1. Differential Reactor Analysis 145
5.3.2. Reactor Model 146
5.3.3. Mechanistic Model 151
5.4. Absence of Mass Transfer Limitations 156
5.5. Octene Isomerization 158
Chapter 6. Heterogeneous Catalysis – Hydrogenation 161
6.1. Introduction and Reaction Literature 161
6.2. Catalyst Preparation 163
6.3. Catalyst Deactivation 170
6.3.1. Cyclohexene Hydrogenation 171
6.3.2. Analysis of Spent Catalyst 176
6.3.3. Discussion of Deactivation Characteristics 177
6.4. Kinetic and Mass Transfer Analysis 179
Chapter 7. Conclusion 186
7.1. Accomplishments 186
7.2. Challenges and Recommendations 189
7.3. Outlook 192
References 194

Appendix A. Microfabrication 207

List of Figures

Figure 1.1. Typical system setup for a bomb reactor capable of high-pressure experimentation. The contents of the reactor are magnetically stirred and the temperature is controlled by an oven. The liquid is loaded first and then pressurized with gas. From Jessop et al.[19] 26

Figure 1.2. A typical silicon microreactor. From Ratner et al.[27] 29

Figure 1.3. Segmented flow in a meandering serpentine microchannel. Gas bubbles, with rounded caps, are dispersed in the continuous liquid phase. 32

Figure 2.1. (a) Photographic examples of the three flow regimes typically found in multiphase laminar flow.[102] (b) An example flow map of the various flow regimes as functions of liquid and gas velocities.[85] From Hessel.[103] 42

Figure 2.2. Geometric scheme used in empirical slug flow size prediction. From Fries et al.[106] . 43

Figure 2.3. Cross section of a dispersed gas bubble in a continuous liquid phase. The liquid fills the corners of the square channel, reducing the expected length of the liquid slug and enabling diffusion between adjacent slugs. 45

Figure 2.4. Micro particle image velocimetry (PIV) measurements of a 2D velocity field showing recirculation motion inside a liquid slug after the average velocity was subtracted from flow field. From Gunther et al.[49] 46

Figure 2.5. Comparison of streamlines for straight (left) and curved (right) channels showing that the center line of symmetry is disturbed in curved channels. From Gunther et al.[50] 46

Figure 2.6. Residence time distribution for a tracer injected into (a) single phase flow and (b) segmented flow. The residence time in both cases was comparable. From Kreutzer et al.[109] 47

Figure 2.7. Visualization of particle trajectories (left half) and velocity vectors (right half) for (a) coalescing flow with bypass and (b) stable recirculating flow. From Thulasidas et al.[115] 51

Figure 2.8. Initial homogeneous reactor design. The top of the reactor is heated, while the bottom of the reactor is cooled. 58

Figure 2.9. Temperature profiles in two 3-dimensional simulations showing the effect of the halo etched region on reducing the power required to sustain a temperature gradient. Power required: No halo = 40.5 W, Halo = 14.1 W... 59

Figure 2.10. Simulation to verify the length of the quenching zone. (a) Simplified simulation diagram with boundary conditions. (b) Temperature of center of fluid channel, from

heated zone to cooled zone. (c) The temperature difference between the wall and center of the channel. ... 61

Figure 2.11. Completed homogeneous microreactor. ... 62

Figure 2.12. (a) Segmented flow comprised of nitrogen bubbles and water slugs. The segmented flow was very regular and did not coalesce over the length of the reactor. (b) When toluene was used as the liquid phase, significant coalescence was observed in the reactor. ... 63

Figure 2.13. As the gas-to-liquid ratio is increased, the apparent liquid slug length decreases even as the overall liquid flow rate is held constant. Stability decreased with increasing gas-to-liquid ratios. ... 65

Figure 2.14. Third T-junction in the original design where the segmented flow typically formed. The bubbles extended to the start of the expansion zone prior to being pinched off. ... 66

Figure 2.15. The three second generation reactor designs introduced new inlet and mixing zones as well as an increased reactor volume. ... 67

Figure 2.16. Eight channel, four inlet reactor for studying high-pressure gas phase heterogeneous catalysis. (Photo courtesy of Bariş Ünal) ... 69

Figure 2.17. Initial heterogeneous reactor design. Eight parallel 45 mm long reaction channels allow up to 58 µl of catalyst bed volume to be loaded. ... 70

Figure 2.18. Completed multiphase heterogeneous microreactor. ... 71

Figure 2.19. Detailed view of the inlet section of the first generation multiphase heterogeneous reactor. Pairs of channels share a common liquid inlet and the gas inlet allows communication between adjacent pairs of channels. ... 72

Figure 2.20. To determine the length of the pressure drop channel, the ratio of the pressure drop in the gas inlet to the pressure drop across the bed was calculated for various gas-to-liquid ratios. ... 75

Figure 2.21. Detailed view of the 300 mm (a.) and 12 mm (b.) pressure reduction channels. The entire second generation reactor design is also shown (c.). ... 76

Figure 2.22. Photograph showing stable gas-liquid flow, at 30 bar, in a multichannel heterogeneous reactor. ... 77

Figure 2.23. Key steps in the microfabrication of homogeneous silicon microreactors. ... 80

Figure 3.1. Schematic of the high-pressure system interfaced with a homogeneous microreactor. ... 83

Figure 3.2. Two primary components of pressure control system: a) EL-PRESS back pressure regulator, consisting of a controller (left) and valve (right). b) Teledyne Isco 100DM high-pressure pump capable of pulse-less flow at flow rates of 1 µl/min and pressures of over 600 bar. ... 85

Figure 3.3. Schematic of gas handling system illustrates the required valves, transducers, and control system. 87

Figure 3.4. SolidWorks representation of gas handling system which provides a spatial model. 89

Figure 3.5. Assembled gas handling system. 90

Figure 3.6. Schematic of the interface between the gas handling system and the gas syringe pump. 91

Figure 3.7. Schematic of the liquid handling system, highlighting the nitrogen and vacuum connections. This system enables the exclusion of oxygen during liquid loading. 91

Figure 3.8. Left: Four-port compression chuck with coned ports. Right: Eight-port compression chuck with flat-bottomed ports. 93

Figure 3.9. Geometric parameters required for calculating reactor deformation in a high-pressure reactor chuck.[52] 94

Figure 3.10. Schematic of the heating chuck attached to a reactor 96

Figure 3.11. Finite elements simulation demonstrates the temperature uniformity across the silicon microreactor in contact with the heating chuck. 97

Figure 3.12. Temperature profile along the base of the reactor in Figure 3.11. The temperature in the heated zone averages 353.7 ± 0.7 K with a maximum temperature difference of 2.7 K. 98

Figure 3.13. CAD model for the degassing gas-liquid separator. 99

Figure 3.14. Capillary gas-liquid separator. Liquid wets and passes through the membrane while the gas is retained on the inlet side. 101

Figure 3.15. CAD model for the capillary gas-liquid membrane separator. 102

Figure 3.16. Photograph of the two integrated two-position six-port valves. 103

Figure 3.17. Schematic of the two-position six-port valves showing the connections between the two valves. 103

Figure 3.18. LabVIEW interface for the high-pressure system. This program controlled all pump, gas handling, pressure, sampling, and temperature systems and could be accessed remotely. 106

Figure 3.19. Turbulent simulation showing face velocities and particle traces for the case when two doors are open. All velocities are above the required 80 ft/min (0.4 m/s). 108

Figure 3.20. Completed system enclosure with six doors per side. 109

Figure 4.1. Flow cell module connected to the iC10 FTIR. Fluidic connections are made to a removable head, which is heated. 119

Figure 4.2. Schematic of the flow path in the head of the flow cell. The flow enters on through the lower port, impinges on the window, and exits through the upper port. [Courtesy of Mettler Toledo] 120

Figure 4.3. Top: Raw reaction data as temperature is varied showing both height and area data associated with nonanal and 1-octene. Bottom: The same data is plotted showing that a linear relationship exists between height and area. (A.U. abbreviates arbitrary unit). 125

Figure 4.4. The iC Quant concentration results from an experimental run, as temperature is varied. While the mass balance closure is perfect, the model makes little physical sense due to the negative concentration of the nonanal product. 126

Figure 4.5. ConcIRT concentration profiles are compared to the peak-height based profile completed manually (Ht). 127

Figure 4.6. A comparison of the ConcIRT pure component spectra against the directly measured pure component spectra shows that Component #1 is correlated with nonanal and Component #3 is correlated with 1-Octene. Component #2 appears to be positively correlated with 1-octene and negatively correlated with nonanal. 128

Figure 4.7. Raw IR data for a multiphase samples is noisy. The peaks and valleys are correlated between 1-octene and nonanal suggesting the magnitude of the entire spectra is varying. 130

Figure 4.8. Raw IR data for a liquid stream only. The variability in peak height is greatly reduced when compared to the multiphase data in Figure 4.7. 130

Figure 4.9. The measured concentration of 1-octene varied during multiphase flow. The concentration of all samples was 0.54 M, as measured in single phase flow. 131

Figure 4.10. Crossover contamination was observed during offline sampling. When two successive samples were analyzed, the first sample was influenced by the previous reaction condition. This was not the case for the second sample. Numbers represent sample order, “d” represents a lower temperature than the previous sample, and “u” represents a higher temperature than the previous sample. 134

Figure 5.1. Widely accepted mechanism for alkene hydroformylation. Steps 2-6 are the dominant cycle and result in the linear aldehyde product. Steps 9-10 represent a similar cycle whose product is the branched aldehyde. 136

Figure 5.2. Raw data for 1-octene hydroformylation at standard conditions. The three measured species are 1-octene (+), aldehydes (■), and 2-octene (◆) measured by FTIR (red filled) and GC (blue open). The circles are the sum of the measurements of all of the GC data and demonstrate good mass balance. 140

Figure 5.3. Prepared calibrations for 1-octene, 2-octene, and nonanal. All calibrations have near zero intercepts and high correlation coefficients. 141

Figure 5.4. IR spectra of the hydroformylation reaction at standard conditions, after solvent subtraction. The 1-octene (0.5 M) is consumed more rapidly at higher temperature to evolve the aldehyde products. The peak at 1642 cm^{-1} corresponds to the C=C stretch of a vinyl group, while 1740 cm^{-1} corresponds to C-O stretch of an aldehyde. 142

Figure 5.5. The spectra for 0.5 hexanal and 2-methylpentanal are nearly identical, with 2-methylpentanal having a 3.5% stronger response. 143

Figure 5.6. Comparison of model (○) to experimental (×) data show good agreement for both the empirical (a-c) and mechanistic (d-f) models. 150

Figure 5.7. Simplified reaction mechanism used for kinetic analysis. 152

Figure 5.8. The mechanistic and power law models show a similar dependence on P_{CO} over the experimental P_{CO} range. 155

Figure 5.9. Alkene coordination on rhodium catalyst can occur at two possible carbon attachment points. When an internal carbon is coordinated, the reverse reaction can result in an internal alkene being produced. 159

Figure 5.10. Left: The conversion of 1-octene to 2-octene is plotted as a function of temperature. At lower temperatures, an exponential relationship exists, while at higher temperature, significant catalyst deactivation is observed. Right: An activation energy of 16.7 kcal/mol is calculated using low temperature data. 160

Figure 6.1. Block diagram of hydrocarbon conversion over platinum catalysts shows the approximate reaction rate range and the most commonly studied temperatures.[164] .. 163

Figure 6.2. Comparison of silica support size profiles before and after sieving show that fine particles are removed. 166

Figure 6.3. Neat cyclohexene was reacted with hydrogen at 30 bar. This room temperature reaction exhibited strong catalytic deactivation over time. 171

Figure 6.4. Spectral comparison of neat cyclohexene data. Contamination is evident in the red spectrum due to an OH stretch around 3300 cm^{-1}. 172

Figure 6.5. Four oxygen-containing contaminant peaks were identified using GC/MS analysis. The sample, which had been exposed to air longer (May 4), had more contamination. 173

Figure 6.6. When cyclohexene is reacted with the platinum on silica catalyst in the absence of oxygen, significantly less deactivation is observed. No deactivation is observed as the temperature is increased. 175

Figure 6.7. Rate of cyclohexene deactivation as the reaction temperature was varied. The three parallel red lines illustrate the rate of catalyst deactivation and show that temperature has no effect on reaction rate during kinetically limited operation. 175

Figure 6.8. Pulse chemisorption results comparing fresh and spent catalyst. The fresh catalyst absorbs significantly more catalyst than the spent catalyst, which is consistent with the observed catalyst deactivation. 177

Figure 6.9. A kinetic study (in the order: ♦, ■, ▲) was performed. Significant deactivation occurred while operating in the mass transfer control region. While the reaction rate had decreased, the slope was similar for both kinetic regions. 179

Figure 6.10. Kinetic (♦) and mass transfer (■) limited data for the hydrogenation of cyclohexene over platinum on silica catalyst. The kinetically controlled data corresponds to E_a = 5.2 kcal/mol. 181

Figure 6.11. Comparison of two days of experiments at the same conditions. The mass transfer limit occurred at the same absolute rate on both days even though the activity of the catalyst varied. 182

Figure 6.12. At constant temperature (50 °C) and cyclohexene flow rate (20 µl/min), the flow rate of hydrogen was varied allowing the reaction rate to transition from mass transfer control to kinetic control. 185

List of Tables

Table 1.1. Comparison of common microreactor materials capable of pressurized operation and exposure to organic solvents. 30

Table 2.1. Property comparison of water, toluene, and squalane at 20 °C.[121] 63

Table 3.1. Summary of conditions that must be attainable in system. 81

Table 3.2. Total displacement deformation for the eight-port chuck constructed from a variety of machinable materials. 94

Table 3.3. Procedure for collecting samples for offline analysis without disturbing system flow using high-pressure valves. 104

Table 5.1. Parameters for the differential equation based power law model, as determined by nonlinear least squares. 149

Table 5.2. Parameters (with 95% confidence intervals) for the mechanistic model assuming equilibrium between the active and inactive rhodium complexes. 154

Table 6.1. Key process parameters required to prepare 5% platinum on silica or alumina catalyst. 169

Table 6.2. Comparison of the contamination level from two samples. The majority of the samples remain cyclohexene. Aldrich's specification was 99% cyclohexene. 173

Table 6.3. Mass transfer coefficients for cyclohexene and 1-octene hydrogenation over platinum on alumina catalyst. 183

Table 6.4. Differences in the diffusivity of hydrogen in the two solvents[178] are consistent with the variation in the measured mass transfer rates. 184

Chapter 1. Introduction

1.1. Alternate Energy Sources will Require New Catalyst Approaches

For over a century, the United States has relied predominantly on fossil fuels as an energy source. Petroleum provides heating, electricity, and most importantly transportation fuels to an increasingly energy intensive country. Natural gas consumption has increased as a cleaner alternative for heating and electricity production. Domestic production of petroleum and natural gas has declined as consumption increased. Currently, 85% of United States energy comes from fossil fuels. The United States imports 61% of the petroleum and 17% of the natural gas that it consumes.[1]

Rapid economic growth in the developing world is sharply increasing overall demand for petroleum and natural gas, increasing the real cost of these feedstocks. The supply of recoverable reserves is not expected to increase significantly in the coming years. Currently, recoverable reserves contain 190 billion tons of oil and 140 billion tons of natural gas, including recent shale gas discoveries.[2] At current consumption rates, the reserve life is 55 years for oil and 110 years for natural gas. Coal, on the other hand, has recoverable reserves of 925 billion tons (carbon basis) which is projected to last 400 years at current consumption levels.

Given the world's strong demand for fossil fuels and how limited petroleum is in particular, the energy landscape is going to undergo significant change in the coming decades. As oil becomes more expensive and begins to be phased out, new sources and forms of energy will be required to replace light petroleum. The world will turn to ever heavier feedstocks such as heavy oils, tar sands, and coal. These feedstocks contain increased amounts of nitrogen and sulfur, as well as higher carbon to hydrogen ratios. This higher carbon content also represents a strong regulatory risk because the world is becoming increasingly concerned with carbon dioxide emissions and it is likely that these emissions will come under stricter control. Methane, the lightest component of natural gas, produces 53 kg of carbon dioxide per million BTU of heat, whereas coal combustion produces over >90 kg of carbon dioxide to produce the same heat.[3]

Biomass is an increasingly popular alternative source of energy. Biomass production captures atmospheric carbon dioxide and is often considered approximately carbon neutral. Recently, the United States was found to have the capacity to replace 30% of gasoline using biomass grown and converted domestically.[4] Biomass presents a challenge because it is chemically different from fossil fuels. Cellulosic and lignin-derived biomass is abundant but requires the development of new techniques and infrastructure to process it. For example, for biomass derived fuels to have the same energy density as gasoline, oxygen must be removed and is typically replaced with hydrogen.

The shift towards biomass and lower quality fossil fuel feedstocks will require new approaches during conversion to the desired products. Catalysis will be critical in the processing of these new feedstocks, much as it has been in the processing of petroleum and natural gas. However, catalysts will now have to deal with complex polyaromatic molecules and enable pathways for producing smaller molecules that have been traditionally found in light petroleum. This will mean increasing the average hydrogen-carbon ratio and removing metals, sulfur, and nitrogen. Novel catalysts will also be required to process lignocellulosic biomass into fuels that are compatible with current infrastructure, such as ethanol and butanol. Catalysis will be the enabling technology, allowing the world to continue consuming energy during the transition away from light petroleum. But before tackling a problem on such a large scale, one must first think small: catalysis development begins in the laboratory.

1.2. Laboratory-based Research and Development

When studying a chemical system, it makes the most sense to start at the laboratory scale. A lot of information can be gathered at this scale, such as identifying the optimal system to complete the desired chemistry at the lowest cost possible. In the case of chemical catalysis, development consists of three distinct steps. The first stage is the laboratory phase during which a catalyst is discovered, studied, and optimized. The second step is proving the catalyst in a pilot plant under commercially realistic, albeit harsh conditions. A pilot plant operates very similar to a final commercial solution, but at a smaller scale. This step is much more expensive than laboratory research due to the required scale of operation. Finally, the catalyst is introduced to a commercial system. At this point, significant capital has been dedicated to this catalyst system and there is very little left to be learned about it. Catalyst development typically takes 3-5 years at a cost of $2-3 million.[5] Since laboratory research is the least expensive type of research, as much information as possible should be gathered at this stage. Specifically, there are four general goals for studies of chemical systems in laboratories: new compound discovery, parameter screening, chemical kinetic determination, and chemical mechanism understanding.

1.2.1. New Compound Discovery

One goal of chemical research is to develop new, more economical ways of making a desired compound. An alternative goal might be to produce new, innovative materials. In the context of catalysis, this type of research could attempt to form a known product with a new reactant or involve creating a new catalyst that would enable the desired product to be produced faster and at lower cost.

There are two general strategies for chasing new discoveries. The first is to use a strong understanding of chemical fundamentals to direct experimentation towards reactants and catalysts that make the desired product. This knowledge is often acquired through an understanding of chemistry fundamentals and by looking at the rich chemical literature. Some understanding can also be provided through increasingly complex chemical simulations, such as density functional theory (DFT) calculations[6] which have been enabled using modern information technology. Recent efforts have included using DFT to inform solid catalyst designs.[7] The second strategy is to develop large libraries of potential reactants and catalysts. This technique does not rely on a researcher's intuition. Instead it uses quick, cheap experiments to screen thousands of possible combinations and hopefully discover a combination that makes the desired catalyst or product.[8] Commercial systems are available to automate this process. For example, instruments from Symyx have been used to discover and optimize new olefin polymerization catalysts.[9] While most discoveries have historically been accidental, these two techniques hope to improve the probability of discovery.

1.2.2. Parameter Screening

Once a reaction has been identified, the goal often shifts to finding a set of conditions that optimizes a certain objective. One approach to this optimization is to perform many experiments varying the relevant parameters. For example, reactant concentrations, temperature, solvent, stoichiometric ratios and other process parameters can all be varied. From these reactions, a set of conditions can be selected that best satisfies the design objective. These methods have found wide application in catalysis, from polymer research[10] to enantioselective catalyst development.[11] Parameter screenings are typically cheap and quick to perform, but do not provide very much information about the chemical system other than a performance surface related to the optimization. Parameter studies are most useful when performed in the final system. They are not sophisticated enough to separate system effects from chemistry effects.

1.2.3. Kinetic Study

Performing a kinetic study is similar to parameter screening but aims to provide a model of the system.[12] Parameter screening is a simpler challenge because the desired outcome is only an optimized set of conditions. Kinetic studies, on the other hand, attempt to provide a mathematical expression that relates reaction rate to all of the parameters that influence it, such as pressure, temperature, and concentration. There are two types of kinetic expressions that can be commonly found in the literature: empirical or mechanistically based. Empirical rate laws are fit to a well-designed set of experiments using regression analysis.[13] The validity of empirical rate laws is limited to the range of experimental conditions. The second method uses an understanding of the chemical mechanism to formulate a series of elementary rate expressions. By making assumptions about the nature of the rate determining step, it is often possible to arrive at a kinetic expression that captures a substantial part of the variability of the data.[14] Kinetic information is often used to design bigger systems for performing a given chemistry, a process known as scale-up.

1.2.4. Understanding Chemical Mechanisms

The final goal of chemical research is to understand the mechanism of chemical reactions. Even for the simplest overall reaction, the identity of intermediate steps is initially unknown. Intermediates are typically short-lived and are difficult to observe. Understanding a kinetic mechanism can help design a better chemical system. For example, during the water gas shift reaction over platinum, carboxyl (COOH) was found to be the key intermediate rather than formate (HCOO).[15] Identifying a desirable reactant characteristic could enable the design of better reagents. Alternately, a catalyst could be designed that lowers the transition state energy required to break the key bond. Mechanistic understanding can also lead to more accurate and robust kinetic expressions.

1.3. Historic Methods for Catalyst Screening

Catalysts come in one of two main types, homogeneous and heterogeneous.[16] Homogeneous catalysts react in the same phase as the reactants and are typically found in the liquid phase. Homogeneous reactions have typically been studied in batch. Heterogeneous catalysts react in a separate phase. These catalysts are often solid and immobilized in a reactor. As the complexity of the chemistries studied increases, new demands are placed on experimental setups that begin to expose the limitations of the current systems.

1.3.1. Common System Limitations

Batch catalyst screening has typically been carried out in laboratories at conditions accessible in glass vessels. Glass round-bottom flasks have been the tool of choice for carrying out batch experiments for years because they have excellent chemical compatibility and are visibly transparent, enabling researchers to observe the reaction as it progresses. Glass is a cheap material and flasks have been devised for all types of purposes, including the rigorous exclusion of air or the ability to operate at reflux.

Batch operation allows for studying time dependent reactions, but requires that every experiment be run independently of the previous. For example, a typical kinetic study requires that a number of parameters be varied, such as temperature, concentrations, and pressure. A typical factorial design of experiment[17] with four parameters (concentrations of two reactants, temperature, and pressure) at each of three conditions would require $3^4 = 81$ experiments. Between each experiment the reactor must be cleaned and prepped for the next experiment. Results from batch reactions are also subject to more variability between experiments since all results are transient. This variability highlights the need for repeat experiments, which only magnifies the inefficiency of batch experimentation. Through clever design of experiments, it is possible to reduce the number of required experiments while minimizing the lost information.[17] It is also possible to increase the efficiency of batch experiments by running them in parallel, which requires devoting substantial resources to the task.

Heterogeneous catalysis has been traditionally studied under continuous flow conditions in stainless steel tubes filled with packed catalyst beds. These systems require significantly more infrastructure than glass flasks, but are more versatile. Tubular reactors are run continuously, enabling reactions samples to be collected more quickly. However, continuous operation at the laboratory scale can require larger quantities of expensive reagents than would be required in batch.

Traditional systems often suffer from mass transfer limitations. For most chemical reactions to occur, two species must interact. This simple step is known as an elementary reaction. Reactions require two things to happen: the reacting atoms must be in close proximity and the reaction must be thermodynamically favorable. The proximity requirement is tied to the idea of mass transfer. Mass transfer is a function of reactor design and geometry, while reaction kinetics are a function of parameters such as temperature and pressure. Mass transfer limitations occur when all species are neither well mixed nor at uniform concentration. For these limitations to occur, the rate of mass transfer must be slower or similar to the rate of reaction. These gradients result in reaction conditions that vary spatially. When mass transfer limitations are present, the results reflect mixing rather than reaction rate. Since the mixing rate is related to the geometry of the reactor, attempting to scale up the process using these results would fail.

Batch reactions carried out in stirred glass flasks are particularly susceptible to mass transfer limitations. The surface area of the phase interface is small relative to the volume of the reacting phase. Flow reactors, with length scales on the order of ¼ inch, are only likely to experience mass transfer limitations when the reaction is rapid. In general, better mass transfer is observed in flow reactors than in batch reactors.

Heat transfer limitations also exist in traditional laboratory scale reactors. Similar to concentration gradients, temperature gradients can form. Reaction rates are typically very sensitive to the local temperature. For batch experiments, temperature control is provided by submerging a glass flask in a temperature bath. This bath is then held at a constant temperature. Heat transfer into the reaction vessel occurs across the glass walls. This heat transfer scales with the surface area of the vessel which is proportional to the square of the radius. Since the volume of the fluid scales with the cube of radius, the efficiency of heat transfer decreases as the vessel increases in size. The scale of a typical flask can support gradients within the fluid. Additionally, glass has a low thermal conductivity, restricting the magnitude of the heat flux. For heterogeneous experiments, heat transfer once again occurs across the walls of the reactor. Metal displays improved heat transfer and the length scales over which heat transfer occurs are reduced when compared to a glass flask. Even so, heat transfer limitations may be observed during rapid reactions. For this reason, very fast, energetic reactions are challenging to study. If the heat is not removed from the system, a runaway reaction could result from the temperature increase. At the very least, gradients would likely exist in the system making gathering kinetic data difficult.

1.3.2. Addressing Pressure Limitations

An additional challenge in typical chemical research is the operation at high temperature and pressure. Chemical reactions typically take place more quickly at higher temperature and pressure making it possible to increase efficiency by raising the temperature and pressure of an experiment. In practice, many homogeneous reactions in the laboratory become limited to the conditions that can be run in glass. If the vessel could be pressurized, the same solvent could be used at higher temperature without boiling. In fact, most industrial gas-liquid processes are run under pressure. Higher pressures increase the concentration of dissolved gases in the liquid phase, which typically increases the reaction rates. Low pressure gas reactors must also be very large, which is not economically practical.[18] Given the commercial importance of chemical systems, it is advantageous to study them in the laboratory at similar conditions.

Alternate techniques have addressed this need. High pressures have been accessible in the laboratory setting using traditional bomb type batch reactors. Bomb reactors are operated similarly to glass bottom flasks, but at high pressure. Jessop et al.[19] describe a typical bomb system (Figure 1.1), which is built around a 50 ml stainless steel reactor. The reactor is placed in a furnace to control the temperature. During operation, the liquid phase is charged to the reactor. Gas is then loaded on top of the liquid phase to pressurize the system. A reservoir is

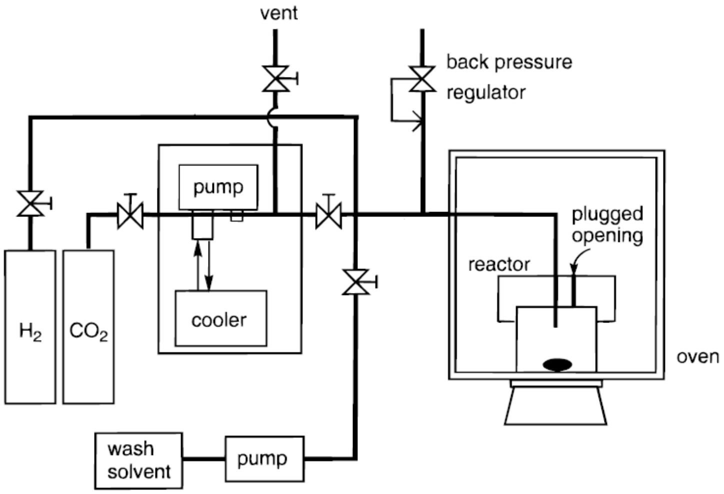

Figure 1.1. Typical system setup for a bomb reactor capable of high-pressure experimentation. The contents of the reactor are magnetically stirred and the temperature is controlled by an oven. The liquid is loaded first and then pressurized with gas. From Jessop et al.[19]

present upstream of a pressure regulator to ensure that the pressure in the reactor remains constant as gas is consumed by the reaction. To address mass transfer limitations, a magnetic stir bar is used to stir the reacting liquid phase.

While this system is able to reach high pressures and temperature due to its stainless steel construction, it still has many of the same challenges that were described above in Section 1.3.1. The system has similar mass transfer limitations and can be subject to very high heat transfer limitations given the thick walls required to support the pressure. Batch operation also reduces throughput by requiring experimentation downtime when conditions are varied. The reactor is no longer transparent, so observation of the reaction becomes more limited. Precise sampling is also more challenging than in a glass flask.

Heterogeneous continuous flow systems have typically been able to operate at high pressure.[20] Stainless steel tubing is strong and can withstand pressure with relatively thin walls. The maximum operating pressure for tubing is a function of tube diameter, with large tubing having a lower maximum pressure. The ability of tubular reactors to operate at high pressure is a welcome benefit of the material selection.

A number of commercial systems have been developed for high pressure catalyst screening. In general, they are targeted at heterogeneous continuous flow catalyst systems where catalyst particles can be loaded into the system. Fewer systems target homogenous continuous flow catalysts because catalyst recovery is challenging and catalyst costs can make these systems unattractive. Instead, systems with parallel batch reactors and a common head space have been developed for high-pressure homogeneous catalysis. Symyx has developed a system for screening 100-150 samples at a time.[21] Symyx has also developed a platform for the complete heterogeneous catalysis workflow.[22] These systems include software to design experiments, catalyst synthesis automation, batch and flow reactors to test chemistry, and software to analyze results. The system to prepare catalyst has a volume on the order of 10 ml, while the reactor volumes are 65-250 µl per channel. ThalesNano has an alternate bench top system for catalyst testing.[23] Catalyst is loaded into cartridges and the system's volume is 6 ml. The system is capable of handling liquid and gas feeds at pressures up to 100 bar. The HEL Group has developed a range of products for heterogeneous catalysis, from low cost, batch-mode catalyst screening in parallel to flow chemistry systems.[24] The volumes of the flow system are on the order of milliliters and can be used at pressures of up to 100 bar. All of these systems provide off the shelf ease of use, but most do not have scales small enough to enjoy all of the microscale benefits. Many of these systems allow for parallel experimentation to address the required down time between experiments.

It is desirable to design new systems that do not suffer from the mass and heat transfer limitations of traditional systems and allow for continuous operation at industrially relevant temperatures and pressures. The system must still be chemically inert and provide optical transparency. Microreactors provide a platform for such a system.

1.4. Microreactors

1.4.1. Overview

Research into the field of microreactors began in earnest in the 1990s to address limitations in traditional chemistry methods.[25, 26] While the earliest microreactors were constructed before this period, technological advances in supporting fields, such as silicon computer chip manufacturing, enabled microreactor technologies. The term microreactor (Figure 1.2) is typically applied to devices that have features that are sub-millimeter in scale, on the order of 50-500 microns. Microreactors, a subset of a class known as microdevices, enable chemical reaction. Other microdevices include detection devices and separators. Microreactors are often compact with external dimensions on the order of centimeters, and depths are often sub millimeter. The defining features of a microreactor are channels, which could be a single long, serpentine channel or perhaps many short channels fed using a manifold. Depending on the overall length of the channel, volumes of up to hundreds of microliters can be attained with high surface area and small cross-sectional areas.

Figure 1.2. A typical silicon microreactor. From Ratner et al.[27]

1.4.2. Material Considerations

Microreactors have been constructed from a variety of materials, allowing the cost and ease of production to be optimized to the application.[28] Polymeric materials such as polydimethylsiloxane (PDMS)[29-31] and Poly(methyl methacrylate) (PMMA)[32, 33] have found wide use as cheap materials for the production of microreactors. Disposable PDMS microdevices have found use in biological research. However these materials are not well suited to harsh chemicals or elevated pressure. Glass,[34] silicon,[35] metal,[36] and ceramic[37] have all been used to fabricate more robust microreactors.

Ultimately, the choice of materials comes down to competing interests of chemical compatibility, ease of machinability, strength, and thermal conductivity. Table 1.1 summarizes the most common material options. While glass is generally desirable, it suffers from very low thermal conductivity. Stainless steel is difficult to micromachine and there is no way to observe the interior of the reactor during operation. Silicon microreactors make the fewest compromises in these parameters.

	Silicon	Stainless Steel	Glass
Thermal Conductivity (W/m-K)[38]	✓✓✓ (153)	✓✓ (17)	✗ (1.1)
Strength	✓	✓✓	✓
Observable	✓ (Pyrex cap)	✗	✓
Ease of Micromachining	✓✓✓	✓✓	✓

Table 1.1. Comparison of common microreactor materials capable of pressurized operation and exposure to organic solvents.

Silicon and Pyrex (borosilicate glass) were chosen as the microreactor materials for the work in this thesis. Silicon's chemical compatibility can be improved through surface coatings of silicon oxide or silicon nitride. Silicon has a high thermal conductivity, and when paired with Pyrex, allows for observation of the internal volume of the microreactor. Silicon micromachining is very established, allowing for a great deal of flexibility in design.[39] Designs that can be imagined and represented in two dimensions can be etched into a third dimension with very high aspect ratios using standard photolithography[40] and deep reactive ion etching (DRIE)[41] techniques. Depending on the requirements, a unique microreactor can be designed for each application.

1.4.3. Benefits Realized in Silicon Microreactors

Microreactors excel in a number of dimensions such as improved mass and heat transport, ability to access high pressures, and improved safety.[42] These benefits have led microreactors to augment traditional techniques. Specifically, microreactors can be used to directly address each of the traditional limitations outlined in section 1.3.1 above. Most benefits originate from the small sizes inherent to microreactor technology.[43]

1.4.3.1. Mass Transport

Mass transport limitations remain one of the challenges of traditional systems. Microreactors allow much faster reactions to be studied before encountering mass transfer limitations. Fast mixing and diffusion can be achieved in microreactors due to reduced characteristic length scales. Diffusion must only occur across sub millimeter distances. Micromixers[44] can also be designed to further enhance mixing. Interdigitated micromixers have been developed which split and recombine streams to reduce diffusional length scales.[45, 46] Active micromixing has also been explored using such techniques as acoustic and periodic flow switching.[47] For reactions that are mass transfer limited in traditional systems, the improved mass transfer can lead to higher observed reaction rates and process intensification.[48]

Mixing has also been shown to improve through the addition of a second immiscible phase. Under specific ratios of the flow rates of the two phases, a stable segmented (slug) flow can be achieved. Segmented flow is shown in Figure 1.3. In the presence of a second phase, internal recirculation has been observed in the liquid slugs, which increases mixing.[48] The addition of meandering sections in the channel can further increase this mixing.[49, 50] Segmented flow also

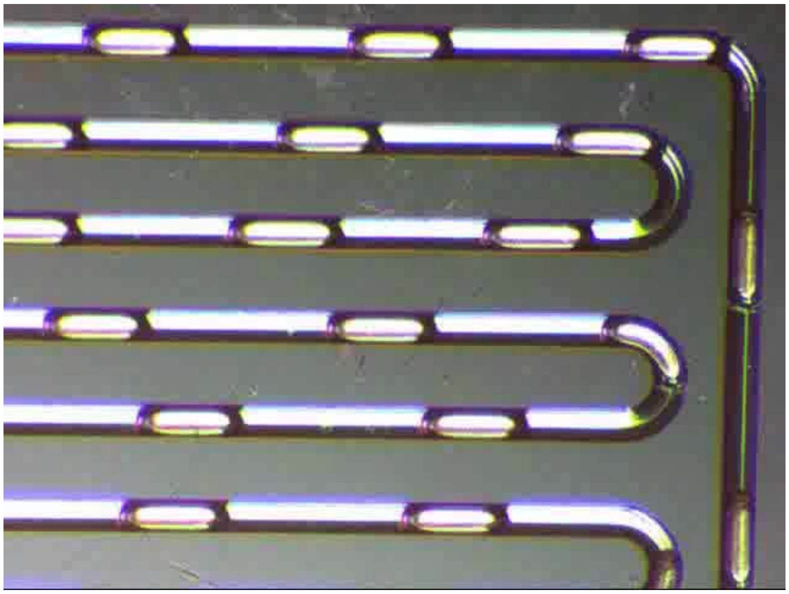

Figure 1.3. Segmented flow in a meandering serpentine microchannel. Gas bubbles, with rounded caps, are dispersed in the continuous liquid phase.

reduces axial dispersion in the flow.[50] This effect can easily be shown using residence time distribution (RTD) techniques.[51] Even though the system is operating in flow, the reduced axial dispersion allows results to be approximated using an ideal plug flow reactor (PFR) model, which is highly analogous to a batch model.

1.4.3.2. High Pressure

The yield strength of a material is an intrinsic property. However, the maximum operating pressure of a reactor is a function of both material properties and the reactor's design. By reducing the internal volume, less force is loaded on the reactor's walls, enabling higher pressure operation. This reduction of force reduces the required thickness of the wall and also reduces the risks associated with catastrophic failure. Microreactors are an extreme example of small volume reactors and are able to withstand very high pressures. The high mechanical strength of silicon, combined with sub-millimeter channels, has enabled extreme conditions such as super critical water (250 bar and 400 °C) to be achieved in microreactors.[52] The accessibility of these conditions have allowed quantum dots to be synthesized in microreactors in both pressurized[53] and supercritical[54] fluids. A number of techniques have been developed for interfacing silicon microreactors to external systems at high pressure including solder and compression schemes.[35, 52, 55]

1.4.3.3. Heat Transfer and High Temperature Operation

The temperature in reactors is controlled by transferring heat across boundaries to the internal fluid. Microreactors benefit from high surface area to volume ratios, which increase the area available for heat transfer to occur. In addition, silicon has a high thermal conductivity (151 W/m K), further improving heat transfer. When high-temperature operation is combined with high-pressure operation, reactions can be studied at temperatures above the normal solvent boiling point. Since high-temperature operation is often associated with faster reaction rates, more reaction pathways become accessible in the laboratory.

Removing heat transfer limitations in reactors has two benefits: safe operation of highly exothermic reactions and isothermal operation. Isothermal operation is a common goal during quantitative study of chemical reactions because it simplifies the extraction of kinetic data.

1.4.3.4. Improved Safety

Microreactors are safer to operate than similar traditional systems for two reasons. First, the required amount of any hazardous chemicals is significantly smaller than would be required at the laboratory scale. This reduction is beneficial when the reaction contains hazardous reactants, intermediates, or waste. The safety of the reaction of chlorine, a hazardous gas, to form phosgene has been improved in microreactors by limiting the amount of chlorine gas in the system.[56] Secondly, good process temperature control enables operation of highly exothermic reactions. If sufficient heat is not removed from the system, the temperature rise in the reactor could lead to a runaway reaction. Direct fluorination[57, 58] is a highly exothermic reaction that would be particularly dangerous to run without sufficient cooling. Chemistries with highly energetic intermediates also have been successfully studied in microreactors.[59] These intermediates would have posed an explosion risk had they been formed in higher quantities in a traditional system.

1.4.3.5. Continuous Operation

Continuous operation of a microreactor reduces the time required to perform an additional experiment. The system does not have to be stopped and cleaned after each experiment. With the addition of real-time analytic equipment, continuous operation allows a parameter to be varied, the system to be monitored until steady state is reached, and a sample to be collected in the minimum possible time. Concentration and temperature are particularly easy to vary in a well-designed system. In addition, there is less ambiguity during scale up to industrial scale. Most industrial processes are operated continuously, making continuous results more desirable than batch results.

1.4.4. Microreactor Applications

Micro total analysis systems have been used in research for a number of different applications including portable energy,[60-62] biological analysis of cells,[63] and assays of proteins.[64] In the chemistry realm, microreactors have enabled high throughput screening of a variety of compounds.[65] They have also been employed for kinetic and mechanistic studies.[66-68] Optimization,[69, 70] including the use of automation,[71] has been efficiently explored in microreactors. Reactions could also be run sequentially to build libraries of known compounds and catalysts.[72, 73] Single microreactors also have been paired to extend to multiple reactions[74] in miniature chemical plants.

Separation is another realm where the benefits of the microscale can complement with traditional techniques. Techniques such as distillation[75] and crystallization[76] have been demonstrated at the microscale. Electrophoretic separation has been applied to charged molecules, such as protein, to develop new separation techniques.[77, 78] Additionally, membranes have been integrated into microreactors during fabrication.[79-83] The absence of gravity-based phase separation required new techniques to be developed for the microscale. Phase separation has been enabled by leveraging the increased importance of surface phenomena, such as surface tension, at the microscale.[84, 85]

Analysis of chemical species has long been a challenge for microreactor systems due to the small volume of samples produced. A variety of schemes has been introduced over time to integrate analytical equipment both inline and onchip. A number of chemical systems have been successfully integrated with micro reactors including ultraviolet/visible spectroscopy,[86] Raman spectroscopy,[87] attenuated total reflectance infrared (ATR-IR) spectroscopy,[67] and nuclear magnetic resonance (NMR).[88] Temperature sensors, which can also act as resistive heaters, have also been integrated onchip,[89, 90] as have microflow[91-93] and pressure[94] sensors.

To date, microreactors have been primarily used as research tools. However, there has been interest in commercializing microreactor technology. Rather than scaling up a reaction that had been successfully studied in a microreactor, the concept of scaling out or numbering up was developed. This concept achieves increased production at the performance of a single microreactor through replication of individual microreactor units. This increased production comes at great cost and control complexity. Bulk chemical production and the challenges facing the energy industry will be difficult to solve using scale out techniques. Microreactors have also been used for production where small quantities of products are required, such as in the pharmaceutical and specialty chemical industries and when safety is a particular concern.[95, 96] Finally, microreactors have become a preferred technology for process intensification.[97] During process intensification, the size of a plant is shrunk by one to two orders of magnitude while maintaining desired production levels. Switching from batch to continuous operation and reducing the number and size of required units are examples of methods that lead to process intensification.

1.5. Motivation

As the world's energy mix shifts towards more challenging feedstocks, there will be a need for new catalyst systems to be identified, studied, and applied to commercial production. Improvements to the traditional methods for catalyst study are possible. These traditional methods excel at providing experimental methods that are widely applied across many types of chemistries. Their largest drawback is the limited range of conditions that can be accessed efficiently in the system. A large gap exists between laboratory conditions and ultimate commercial operation. Once a catalyst is optimized at standard conditions, testing is conducted at the pilot plant scale at increased cost. Shifting more experimentation to the laboratory could greatly reduce the cost of catalyst development.

Even the initial optimization can require hundreds of experiments that take substantial time when conducted in batch. Shifting homogeneous catalysis to continuous flow operation can reduce the time required to perform these experiments. Further driving interest in continuous flow experiments is the increased automation that can be achieved. Non-parallelized batch experimentation requires manual labor to clean and restart the reactor between each experiment. The study of heterogeneous catalysts has benefited from continuous flow for decades.

Advances in catalysis will require a number of different approaches. Both homogeneous and heterogeneous catalysts will be needed. Kinetic modeling of reactions is required to understand the rate behavior of chemical reactions. The kinetics of a catalyst system are scale independent and therefore form the core of scale-up reaction-engineering studies. While the kinetics of heterogeneously catalyzed systems are often studied, only limited information exists for the homogeneous kinetics.[98] Instead, studies focus on the chemical aspects of the catalysts, such as ligand selection.[99] Typical homogeneous catalysts are organometallic compounds whose activity is greatly affected by the attached ligands. Different products can be formed from a single substrate and metal center by varying the attached ligand.[100] Homogeneous catalysts often have higher activity and selectivity than their heterogeneous counterparts. Many novel homogeneous catalysts are being developed in chemistry laboratories because of the wide availability of ligands that can be tuned to particular applications. Homogeneous catalysts in continuous flow systems are at a distinct disadvantage due to the difficulty recycling them. Heterogeneous catalysis has been preferred industrially due to its lower cost and ability to stay confined to the reactor. These catalysts have traditionally consisted of metal alloys, oxides, or sulfides on a porous support. Enzymes are sometimes considered a separate group since they possess characteristics of both homogeneous and heterogeneous catalysts.[101] An ideal analysis system would be able to support both types of catalyst. In either homogeneous or heterogeneous catalysis, the reaction can involve more than one phase. Many liquid phase reactions that upgrade biomass require hydrogen gas. Microreactors have far higher multiphase mass transfer ensuring that the kinetics can be observed directly.

Microreactors have been previously used to study catalysis, but at lower pressures than are used industrially. Many of the inherent capabilities of microreactors make them well suited to catalytic analysis, but the systems that support the microreactors remain a hidden challenge. It is nontrivial to interface a microreactor with fluid delivery and analysis systems. Overcoming these limitations remains an interesting research area. In particular, high-pressure fluid-delivery systems remain orders of magnitude larger than the microreactor that they support. There is an opportunity to design a system that takes new approaches to enable rapid experimentation.

For any reaction studied, catalyzed or not, the goal is to collect correct information, irrespective of the system used. Limitations of the experimental apparatus cannot cause any artifacts in the data. The goal of an experimental setup is to be transparent to the researcher, neither obfuscating the data nor preventing experimentation at the desired conditions. Both within academia and in industry, there is a strong desire for such systems that reliably probe the kinetics and mechanisms of catalytic systems. Thus there is a need to develop a laboratory system capable of reliable kinetic study, in multiple phases, at industrially relevant conditions.

1.6. Thesis Objectives and Overview

To address the need for new systems that enable the study of catalysis, a system was designed, constructed, and demonstrated on both homogeneous and heterogeneous catalysts. The system is capable of study at industrially relevant conditions, such as temperatures from room temperature to 350 °C and pressures from atmospheric to 100 bar. It has been built around multiple analysis techniques that provide complementary information. The system is designed to enable very fast mass transfer to ensure that the observed reaction rates are kinetically limited. This system is capable of more efficient kinetic experimentation than traditional batch systems and is more versatile than commercially available catalyst screening systems.

Principles of microreactor design and their application to two and three phase microreactors are discussed in detail in Chapter 2. A discussion of the final system components, construction, and their interactions are discussed in Chapter 3. Chapter 4 contains details of the system operation and analytic infrastructure.

The completed system was validated by studying homogeneously catalyzed hydroformylation of alkenes to aldehydes by Wilkinson's catalyst. The conditions for this chemistry were well within the capabilities of the designed system and fully explore its capabilities with multiphase operation. A kinetic expression for the hydroformylation of 1-octene along with mechanistic and system insights are presented in Chapter 5.

The system was further expanded to study heterogeneous catalysis. The system was demonstrated on the very rapid hydrogenation of alkenes to alkanes. A 5% platinum on alumina catalyst and a 5% platinum on silica catalyst were synthesized, studied, and compared. These results are summarized in Chapter 6.

In the final chapter, Chapter 7, the work and its contributions are summarized. In addition, characteristics of chemistries suitable to be studied in microreactors are discussed. Areas for future research are also indicated.

Chapter 2. Microreactor Design and Construction

At the core of the high-pressure analysis system lies the microreactor. Microreactors, due to their characteristic length scales, can leverage improved heat and mass transfer and high-pressure operation, which have been highlighted in detail in Section 1.4.3. The microreactor must be designed intelligently to take advantage of these benefits, requiring an understanding of the specific phenomenon that will be harnessed. For multiphase operation, segmented flow provides the advantage of improved mass transfer but also the challenge of maintaining stable flow. An understanding of segmented flow enables efficient design and operation. To study heterogeneous catalysis, a packed bed is often used which ultimately requires new reactor designs. A set of reactors were designed for homogeneous catalysis as well as heterogeneous catalysis. All reactors were then fabricated using standard MEMS (microelectromechanical systems) fabrication techniques.

2.1. Segmented Flow

Segmented flow refers to a distributed flow with a continuous wetting phase and an immiscible dispersed phase (Figure 2.1a). It occurs when the flow rates of the wetting and non-wetting phases are of similar order. The dispersed phase forms bubbles that span the width of the channel. A slug is found in the continuous phase between two consecutive bubbles. Segmented flow is not the only flow regime that can be observed in laminar multiphase reactors. Figure 2.1 shows photographic examples and a flow map of the various flow regimes. Bubbly flow occurs when the flow rate of the wetting phase is much larger than the flow rate of the non-wetting phase. Droplets form with a diameter less than the channel width. Annular

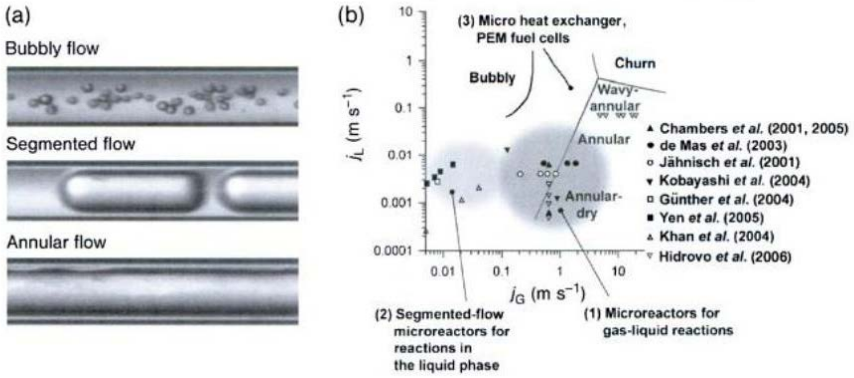

Figure 2.1. (a) Photographic examples of the three flow regimes typically found in multiphase laminar flow.[102] (b) An example flow map of the various flow regimes as functions of liquid and gas velocities.[85] From Hessel.[103]

flow represents the other extreme. It occurs when the flow rate of the wetting phase is much smaller than the flow rate of the non-wetting phase. Under this regime, the wetting phase is confined to the region adjacent to the walls while the non-wetting phase populates the center of the channel. Depending on the shape of channel cross-section, significant non-uniformity might exist in the wetting phase thickness.

2.1.1. Formation

Segmented flow typically forms at a T-junction in a microdevice. The continuous phase flows down a straight channel, while the non-wetting phase impinges perpendicularly on this flow. Capillary instability leads to the formation of segmented flow. Garstecki et al. identified four stages in the formation of segmented flow: (1) the disperse phase enters the main channel, (2) the disperse phase completely blocks the main channel, (3) the bubble elongates down the length of the main channel, and (4) the bubble separates from inlet stream.[104] They also demonstrated a simple scaling expression for the length of a bubble,

$$L_B/w = 1 + \alpha\, Q_d/Q_c \qquad (2\text{-}1)$$

where L_B is the bubble length, w is the width of the channel, $Q_{c/d}$ are the flow rates of the continuous and dispersed phases, and α is a fitted constant of order 1.

Geometry plays a large role in the ultimate size of the bubbles and slugs, which is not captured in Equation 2-1. For example, significant leakage occurs in the corner of square channels as bubbles form, which elongates the final bubble.[105] Fries et al. developed a correlation for determining slug and bubble length to improve estimates for square channels and when the flow rate of gas is greater than the liquid flow rate.[106] It extends Equation 2-1 by estimating a value for α based on geometric considerations

$$\alpha = 17.2131\gamma^{-1}\beta^{-0.5} \qquad \mathbf{(2\text{-}2)}$$

where γ is the ratio of the width of the main channel to the gas inlet width (w/w_{gas}) and β is the impingement angle (see Figure 2.2). While traditional junctions to form segmented flow are T-shaped, this correlation allows the gas to impinge at an arbitrary angle β.

Liquid slug length has traditionally been calculated from the bubble length using the simple scaling ratio,

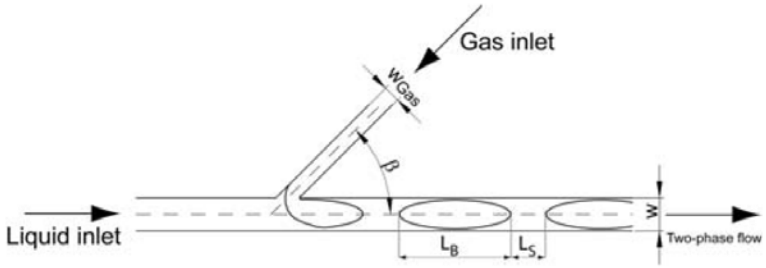

Figure 2.2. Geometric scheme used in empirical slug flow size prediction. From Fries et al.[106]

$$\frac{L_B}{L_S} = \frac{Q_d}{Q_c} \tag{2-3}$$

However, this fails to account for the liquid that wets the corners of a square channel alongside a gas bubble. A typical bubble cross section can be found in Figure 2.3. Thus, to develop an estimate of the length of liquid slugs, a separate correlation is required that can take fluid properties into account, since they affect the shape of the bubble, specifically R_c. Fries et al. developed the following correlation for liquid slug length

$$\frac{L_s}{w} = k \cdot l \cdot n \left[\left(\frac{\mathrm{Re}}{\mathrm{Ca}} \right)^{0.33} \frac{\varepsilon_L^*}{\gamma^l \beta^m} \right] + n \tag{2-4}$$

$k = 0.369$ $l = 2.5$ $m = 1$ $n = 3.15$

$$\mathrm{Re} = \frac{\rho V D_h}{\mu} \tag{2-5}$$

$$\mathrm{Ca} = \frac{\mu V}{\gamma_{cd}} \tag{2-6}$$

$$D_h = \frac{4A}{P} = \frac{4wh}{2(w+h)} \tag{2-7}$$

$$\varepsilon_L^* = \frac{Q_c}{Q_c + Q_d} \tag{2-8}$$

where Re is the Reynolds number, Ca is the capillary number, D_h is the hydraulic diameter, ε_L^* is the ratio of liquid to total volumetric flow, ρ is the density, V is the superficial bubble velocity, μ is the fluid viscocity, γ_{cd} is the surface tension between the continuous and dispersed phases, and ratio w and h are the channel width and height. For the case of a square channel, the hydraulic diameter is equal to width of the channel.

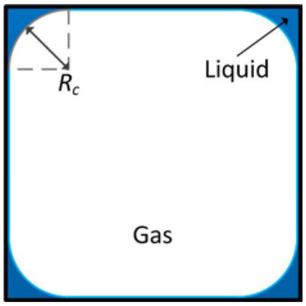

Figure 2.3. Cross section of a dispersed gas bubble in a continuous liquid phase. The liquid fills the corners of the square channel, reducing the expected length of the liquid slug and enabling diffusion between adjacent slugs.

From these correlations, a number of trends can be identified. For example, the liquid slug length increases when surface tension increases or viscosity decreases. The unit cell length - the total length of one bubble and slug unit - increases as liquid holdup decreases, the gas inlet width increases, and the inlet angle β decreases. The unit cell length is also directly proportional to the channel width.

A theoretical, closed-form expression for the size of bubbles was recently proposed by van Steijn et al.[107] The expression is based on continuity, geometry, and an understanding of the mechanism of droplet formation. The expression was validated using experimental results and provides an alternative to the correlation above for determining bubble size.

2.1.2. Mixing and Residence Time Distribution

Segmented flow enhances mixing in the continuous phase by introducing recirculating flow. The recirculation results from the different boundary conditions in the slug: nonslip at the walls and slip at the dispersed/continuous phase boundary. A stagnation point can be observed at the phase boundary on the symmetry line (Figure 2.4). When the average velocity is subtracted

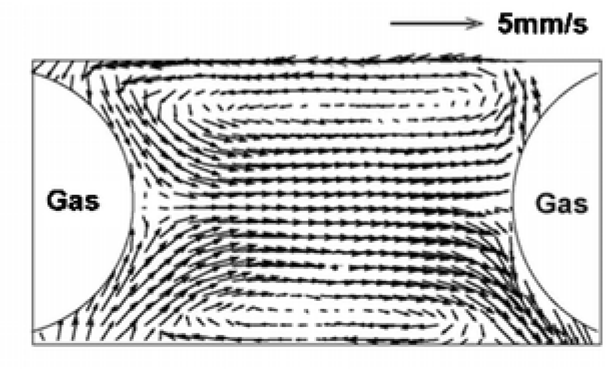

Figure 2.4. Micro particle image velocimetry (PIV) measurements of a 2D velocity field showing recirculation motion inside a liquid slug after the average velocity was subtracted from flow field. From Gunther et al.[49]

from the flow field, recirculation cells are visible around the line of symmetry. This recirculation aids mixing and multiphase mass transfer.

Mixing could be further improved if flow could be induced to cross over the symmetry line in the center of the channel. Gunther et al. demonstrated that undulating channels, as opposed to straight channels, break the symmetry and enhance mixing.[50] This enhancement can be readily seen from streamlines in both straight and curved channels (Figure 2.5). Curvature leads the inner meniscus to become thinner than the outer meniscus, leading to a break in symmetry.[108] Thus, undulating channels enhance mixing by varying which wall has the smaller

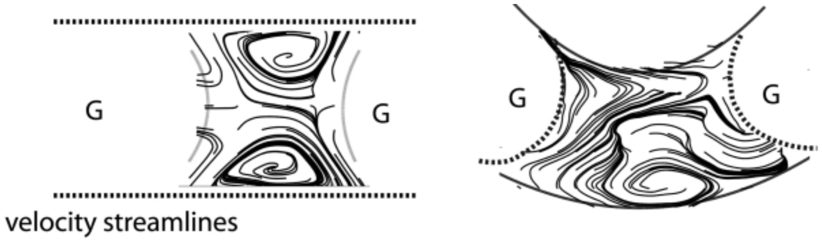

Figure 2.5. Comparison of streamlines for straight (left) and curved (right) channels showing that the center line of symmetry is disturbed in curved channels. From Gunther et al.[50]

radius of curvature and enabling flow across the midpoint of the channel. For optimal mixing, an undulating channel should be placed after streams are combined to quickly achieve homogeneity.

In segmented flow, adjacent slugs appear to be isolated by the dispersed phase. However, a meniscus exists around the dispersed, non-wetting phase that allows communication between adjacent slugs. In effect, segmentation only reduces axial dispersion in the continuous phase. In square channels, a substantial layer of the continuous phase exists in the corners of the channel (Figure 2.3). Residence time distribution (RTD) analysis can be used to study how much diffusion occurs between adjacent slugs. Kreutzer et al. injected a tracer into single phase and segmented flows to demonstrate the reduced dispersion in segmented flow (Figure 2.6).[109] The

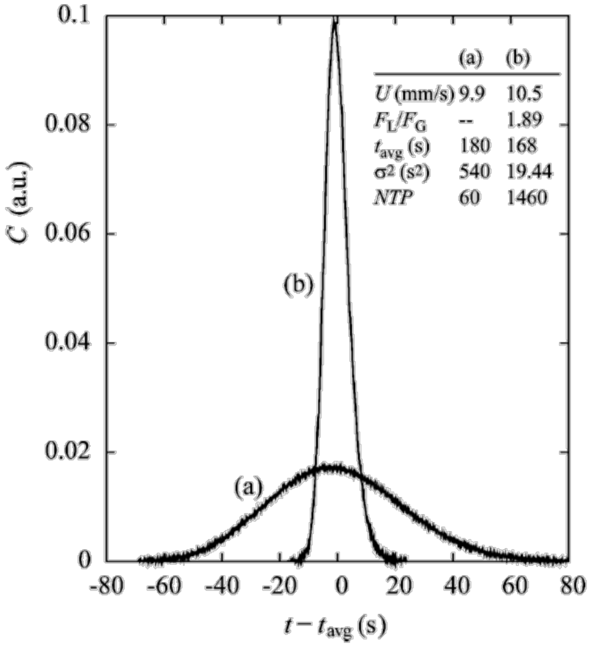

Figure 2.6. Residence time distribution for a tracer injected into (a) single phase flow and (b) segmented flow. The residence time in both cases was comparable. From Kreutzer et al.[109]

peak width in the segmented flow scenario reduced the peak width by a factor of 5. In addition, they found that dispersion decreases with increasing velocity, but at a less than linear rate. Decreasing the gas-to-liquid ratio was also shown to reduce dispersion for a constant linear velocity. Reduced transport between adjacent slugs is a key advantage of multiphase microfluidic systems.

The mass transport benefits associated with segmented flow diminish if the flow is unsteady and the lengths of the bubbles and slugs increase due to coalescence. Specifically, the axial diffusion length for mass transfer increases while the phase boundary surface area decreases. These changes will affect the rate of mass transport which can introduce erroneous results to kinetic experimentation.

2.1.3. Stability of Segmented Flow

Once formed, segmented flow has the potential to remain stable for long periods of time. Therefore, observed instabilities are manifestations of problems around the junction where the flow forms. Semi-stable bubbles can coalesce if given enough time. When designing a microreactor that will have residence times on the order of minutes, these instabilities might have enough time to manifest. Galbiati et al. demonstrated how disturbances in the inlet region can greatly change the flow regime.[110] In addition, they observed that, given a long enough channel length, small disturbances were magnified and led to coalescence.

Many disturbances in microreactor systems come from pressure fluctuations. External pressure fluctuations are very common primarily due to fluid distribution systems. Kraus et al. performed a statistical study of gas-liquid segmented flow and determined the probability density function of gas bubble dwell times.[93] They used three different methods to drive the liquid segmented flow: a Harvard PHD2000 syringe pump, an Inotech syringe pump, and a pressurized tank. While all three pumps were operating at the same average flow rate, differences in the probability density functions were observed. This suggests that the way that the pumps operate, likely due to pressure pulses, affects the characteristics of segmented flow. These pressure pulses likely extend to segmented flow stability.

The origin of fluctuations in pressure caused by syringe pumps is related to the two ways in which mechanically driven flow differs from pressure driven flow. First, the motor in mechanically driven flow introduces a characteristic step motion as the screw turns. Secondly, the elasticity of the fluid leads to a phenomenon known as the "bottleneck" effect.[111] As a fluid is compressed in a syringe, the diameter of the syringe is much larger than the exit microchannel. This results in a very long transient before steady pressurization is achieved. This phenomenon is not observed in the absence of a microchannel, which is small relative to the syringe diameter. Another source of pressure instability comes from the elastic behavior of some types of tubes, resulting in very long transients.[112]

The addition of hydrodynamic resistance upstream of the segmented flow junction has been shown to improve the stability of segmented flow. De Mas et al. found that to stably operate a slug flow reactor, a hydrodynamic resistance is required in the inlet channel that is larger than the pressure drop in the remainder of the reactor.[57] They found that this result was particularly true when multiple parallel channels were fed by the same feed line. Pressure fluctuations have also been shown to cause oscillatory bubbling.[113] Khan et al. developed an 'electricalhydraulic' model before testing it experimentally. Oscillatory bubbling was observed when flexible tubing was placed in series with a large diameter (500 µm ID) rigid polyetheretherketone (PEEK) tube. However, once the PEEK tube was replaced with a narrow diameter tube (65 µm), regular, monodisperse bubble sizes were observed. Thus, careful consideration must be given to fluid delivery lines to ensure stable flow; specifically, the pressure drop in the inlet tube/channel must be larger than the pressure drop in the channel.

Bubble coalescence is one of the most observable forms of segmented flow disturbance. Oztaskin et al. studied the stability of segmented flow in square microchannels using volume of fluid (VOF) simulations.[114] They considered two bubbles in a continuous liquid. A periodic boundary condition was used axially along the channel. The length scales used were larger than would be typical for microreactors, which also led to the inclusion of buoyancy in nearly all simulations. They considered bubbles and slugs of a variety of sizes. To perturb the system, the ratio of the lengths of two adjacent liquid slugs was varied.

Oztaskin et al. found that the two bubbles coalesced or recovered to the unperturbed system when both liquid slugs were of the same length. Essentially, a stable flow is one in which all liquid slugs are the same length. When the length of a slug was perturbed, some simulations returned to this stable flow while others became increasingly unstable and bubble coalescence was observed. When looking at the flow (Figure 2.7), it became clear that a minimum slug length must exist for recirculation to occur in the liquid slug. When a slug with recirculation was perturbed, it was able to recover. Specifically, when the dimensionless slug length (L_s/D_h) is less than 0.1, bypass flow was observed which led to the shrinking of the liquid slug and

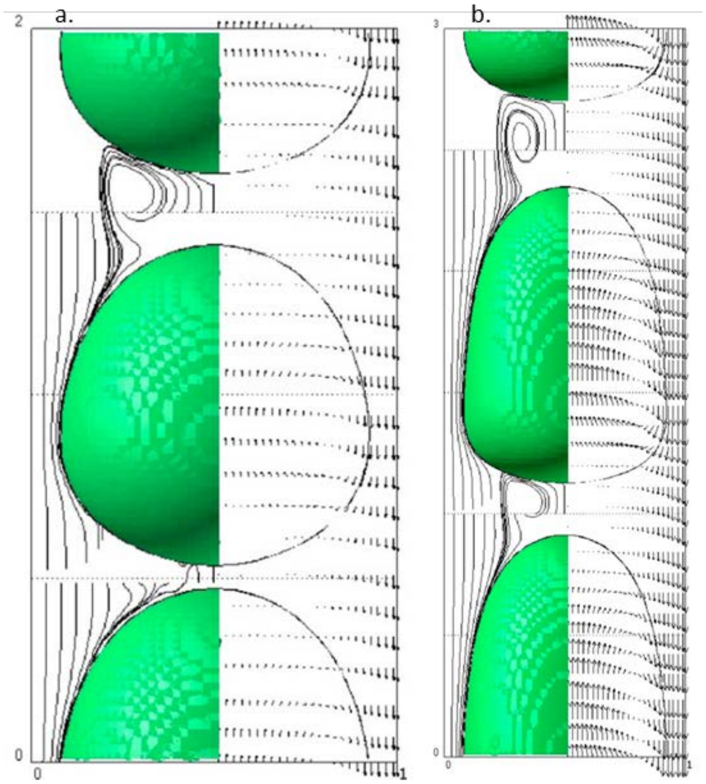

Figure 2.7. Visualization of particle trajectories (left half) and velocity vectors (right half) for (a) coalescing flow with bypass and (b) stable recirculating flow. From Thulasidas et al.[115]

coalescence. However, when L_s/D_h was greater than 0.2, recirculation was observed and the system recovered. In a similar work, Thulasidas et al. experimentally found that the liquid slug flow profile was fully developed when L_s/D_h was greater to or equal to 1.5.[115] This work suggests that there is a minimum slug length required to enable stable segmented flow. Otherwise, any small perturbation to the pressure envelope of the system, such as a disturbance from a syringe pump, would result in bubble coalescence.

2.1.4. Mass Transfer Model

When using a microreactor system to study a kinetic system, it is important to observe kinetics, not an artifact due to insufficient mass transfer. One check would be to estimate the mass transfer in the system and ensure that it is faster than the recorded reaction rates. In general, there are two separate contributions that can be considered: (1) mass transfer from the body of the bubble to the lubricating film and corner regions and (2) from the caps of the bubble directly to the liquid slug[116]

$$k_L a = k_{L,film} a_{film} + k_{L,cap} a_{cap} \tag{2-9}$$

The film transfer step also includes the diffusion from the film around the body of the bubble to the liquid slug. This model works best for the case where the liquid slugs are long, allowing complete mixing between the liquid film and the liquid slug.

Yue et al. developed a mass transfer correlation for gas-liquid segmented flow inside square microchannels.[117] The final expression for the mass transfer coefficient, $k_L a$, was

$$k_L a = \frac{2}{D_h}\left(\frac{DV}{L_B + L_S}\right)^{0.5}\left(\frac{L_B}{L_B + L_S}\right)^{0.3} \tag{2-10}$$

where D is the diffusivity of the gas species in the liquid phase. The length of the gas bubble strongly influences the mass transfer, which suggests that the film contribution is significant. If the bubble length did not have an impact, it would suggest that the mass transfer only occurred across the bubble cap. In addition, mass transfer is improved as the velocity of the flow increases or the length of the bubble decreases.

2.2. Gas-Liquid Flow over Packed Beds

When microreactors are used to study heterogeneous catalysis, a third solid phase is added to the system. While packed beds are the most versatile method of introducing a solid, it is also possible to deposit catalyst on to the walls of the channel using techniques such as wash coating[61, 118] or on impregnated structured packing.[89] Packed beds provide the greatest flexibility because it is possible to recover the packed catalyst for further tests or to reuse the reactor with another catalyst. In addition, the surface area of the packed bed is orders of magnitude larger than the wall surface area, for a given volume.

2.2.1. Micro Packed Beds

Micro packed beds are a simple way to add a third participating but immobilized phase to a microreactor. One of the largest practical challenges around packed bed microreactors is high pressure drops, particularly when compared to an unpacked channel. Pressure drop scales linearly with length and is strongly affected by the size and packing density of the bed. The Ergun equation describes the pressure drop for single phase flow through a packed bed of spherical particles,

$$\frac{\Delta P}{L} = \frac{150\mu(1-\varepsilon)^3 V}{\varepsilon^3 D_p^2} + \frac{(1-\varepsilon)\rho V^2}{\varepsilon^3 D_p} \tag{2-11}$$

where P is the pressure, L is the length of the bed, ε is the void fraction, and D_p is the diameter of the spherical particles. For relatively slow flows, the first term dominates. From the first term, we can see that pressure drop increases linearly with increasing bed length, viscosity, and velocity and decreases with the square of particle diameter.

To ensure uniform flow across a packed bed, the size of the particles must be much smaller (<1/10) than the width of the channel. Otherwise channeling will occur in the flow, particularly in the void adjacent to the wall. A typical microreactor channel has a width of 400-500 µm.

Therefore, typical particle diameters in micro packed beds are an order of magnitude smaller, approximately 50 µm. Even under slow flow, large pressure drops are observed. Large pressure drops are a particular problem for reactor systems run at low pressures. It may be difficult to overcome the pressure in these situations. In addition, as the pressure changes over the course of the bed, so does the concentration of gas species. The change in the concentration of gas is proportional to the ratio of pressure drop to total pressure. This concentration change further complicates kinetic measurements. At high pressures, overcoming moderate pressure drops are of smaller concern. In addition, the same nominal pressure drop will have a smaller effect on the measured kinetics because the total pressure is much higher, reducing the ratio of pressure drop to total pressure. Other fluid properties do not change significantly with pressure. Pressure drop is also a larger concern for flows that contain liquid rather than gas at comparable velocities, since the viscosity of liquid is much greater than the viscosity of gas.

There are a number of design strategies for reducing the pressure drop in packed beds. These strategies center on reducing the length of the bed for a given volume of catalyst. The simplest would be to increase the cross-sectional area by simply widening the bed and reducing the length. This strategy can work well for low pressure reactors. In high-pressure reactors, it is possible to run into failure due to material limitations. The stress exerted on the wall of a channel scales with the square of the channel width, where the width is smaller than the length. Thus a wide bed is much more likely to fail than a narrow bed.

A second approach to increasing the cross sectional area of the bed is to separate a single bed into parallel channels. Using parallel channels allows for narrow channels and high-pressure operation. However, parallel channels require a more complicated flow distribution system than is required for a single channel. Without uniform flow along each channel, it would be impossible to determine the amount of catalyst that participated in the reaction or the residence time. Losey et al. designed an early packed bed reactor that used parallel channels. Their design consisted of an array of 10 channels connected through a manifold.[89] The gas and liquid were mixed through a continuous split and mix strategy prior to the reaction channel. To allow catalyst loading, a wide channel was run perpendicular to the reaction channels. The catalyst particles were loaded in a slurry, which required a minimum velocity for the particles to remain in solution. The pressure required to satisfy this velocity became unattainable as the reaction channels filled with particles. By having the loading channel run parallel to the reaction channel, particles could be flowed at the required velocity both through and past the reaction channels. However, the loading channel also created a large dead volume during catalyst tests.

A third approach is to design a cross flow packed bed. This bed has a very short length in the direction of flow, and thus experiences a small pressure drop. It also overcomes the pressure limitations associated with wide packed beds because the stress exerted on the channel wall scales with the square of the bed length. However, a wide bed can also have flow distribution difficulties. Ajmera et al.[66, 119] designed a manifold system to ensure uniform distribution across the wide bed. The inlet channel bifurcates into 64 parallel channels followed by 256 shallow pressure drop channels. The pressure drop channels dominate the pressure drop in the rest of the reactor to ensure that variations in the catalyst loading do not affect the overall flow distribution. This design did not have any mixing zones to complicate the design because it was designed to operate in a single phase.

2.2.2. Mass Transfer Model

A simple mass transfer film model can be applied to three phase microreactor systems. There are three mass transfer steps required to get a reactant that is in the gas phase to react at an active site on a catalyst particle. The first step is for the gas to absorb into the liquid phase. The second step is for the dissolved gas to diffuse from the bulk liquid to the catalyst surface. The third and final step is for the dissolved molecule to diffuse into the catalyst particle. All three steps are required for reaction to occur, and they occur in series. Hence, applying the resister analogy, the overall reaction constant k_{ov} can be expressed as

$$k_{ov} = \frac{1}{\frac{1}{k_l a_i} + \frac{1}{k_c a_s} + \frac{1}{\eta k}} \tag{2-12}$$

where $k_l a_i$ is mass transfer resistance of the absorption into liquid across the interface, $k_c a_s$ is the diffusion of the dissolved gas from the bulk liquid to the catalyst surface, η is the catalyst effectiveness factor, and k is the intrinsic rate constant. It is difficult to determine the two mass transfer coefficients independently with any certainty and thus they can be lumped together in an overall mass transfer coefficient $k_L a$. Equation 2-12 can therefore be simplified to

$$k_{ov} = \frac{1}{\frac{1}{k_L a} + \frac{1}{\eta k}} \tag{2-13}$$

Calculating the value of the effectiveness factor requires knowledge of the intrinsic kinetics. Losey et al. determined the mass transfer in a single channel micro packed bed using this expression to be in the range $k_L a$ = 5-15 s^{-1}.[120] This represents a significant improvement over typical laboratory trickle-bed reactor system where $k_L a$ = 0.01-0.08 s^{-1}.[18]

2.3. Microreactor Designs

The ideal microreactor design differs depending on whether homogeneous or heterogeneous catalysis systems are studied. A homogeneous reactor would consist primarily of a long channel to enable studying slow reactions at long residence times. A heterogeneous reactor design would be dominated by having enough catalyst for reaction to occur while controlling the pressure drop.

2.3.1. Homogeneous Reactors

2.3.1.1. Initial Design

The initial homogeneous reactor design was provided by Samuel Marre.[52] This reactor had been designed for nanoparticle synthesis, which shares design objectives with homogeneous catalysis kinetics. Specifically, the reaction was to proceed through a known reactor volume under isothermal conditions. A two dimensional sketch of the reactor is shown in Figure 2.8.

The features shown in Figure 2.8 are etched anisotropically into a 650 μm thick silicon wafer, resulting in a channel with three silicon walls. The features were etched to a depth of 400 μm. A 1 mm Pyrex wafer was bonded to the silicon wafer, forming the fourth wall of the channel. The reactor design has a number of different sections that are designed to take advantage of unique aspects of segmented flow.

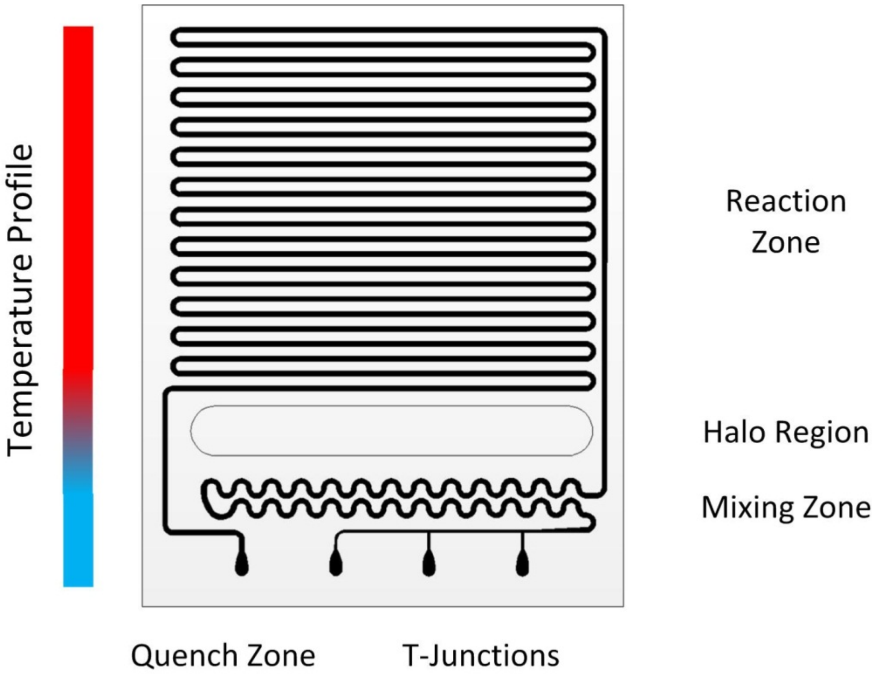

Figure 2.8. Initial homogeneous reactor design. The top of the reactor is heated, while the bottom of the reactor is cooled.

There are two zones in the reactor, heated and cooled, separated by a halo etched region. Silicon has a thermal conductivity two orders of magnitude greater than Pyrex (silicon: 153 W/m K; Pyrex 1.1 W/m K). Therefore, to sustain a temperature gradient, silicon must be removed between the two zones. A halo etch removes a large cross section of silicon and forms a boundary between the two zones. The bulk removal of silicon allows a temperature gradient to be sustained across the remaining silicon with a lower overall heat flux. The heated zone is maintained at a constant temperature to allow reaction to occur. The cooled zone consists of a pre-reaction mixing zone as well as fluidic ports. This zone is cooled to facilitate mixing prior to reaction, to quench the reaction before leaving the chip, and to enable polymeric sealing of the fluidic connections.

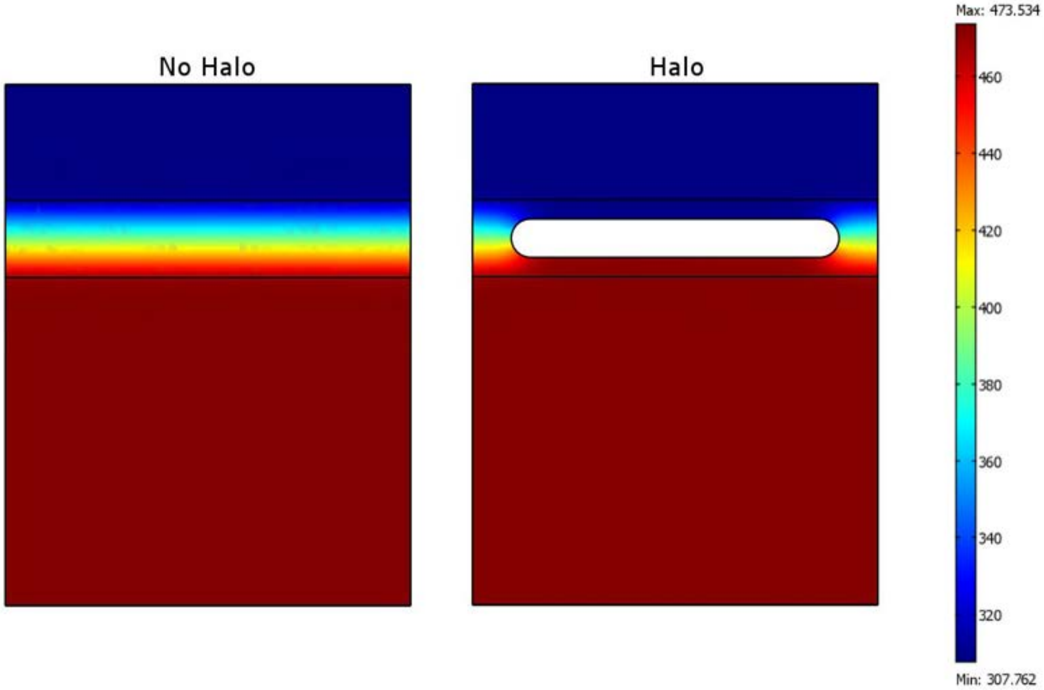

Figure 2.9. Temperature profiles in two 3-dimensional simulations showing the effect of the halo etched region on reducing the power required to sustain a temperature gradient. Power required: No halo = 40.5 W, Halo = 14.1 W.

The halo etched region allows a temperature gradient to be sustained at lower overall heat flux. Figure 2.9 shows two three dimensional COMSOL Multiphysics simulations. A silicon wafer is represented with and without a halo etched region. In both cases the reactor is capped with a silica glass layer. Constant temperatures are applied to the rectangles at the bottom (T_H = 200 °C) and top (T_C = 35 °C) of the reactor. All of the remaining boundaries are approximated adiabatically. The simulations show a similar temperature gradient existing between the two temperature zones. The advantage of the halo etched region is the reduction of heat that must be added or removed from the reactor to sustain that large gradient. The amount of heat added to the heated decreases by a factor of 2.9. In the reactor without the halo etch, 40.5 W of power is required. In the reactor with the halo etch, only 14.1 W of power is required.

The inlets at the lower right hand corner of the reactor enter at T-junctions. The widths of both the main and inlet channels were not fully optimized and have widths of 200 µm. There are three inlets allowing any combination of liquid and gas streams to be mixed in the inlet region. The width of the main channel then expands to 400 µm. The channel width in the inlet region was narrower so that smaller volume bubbles and slugs would form. After expansion, the bubbles and slugs would still span the channel and their length would be halved, since they have a fixed volume. This design attempted to have very small bubble and slug sizes to improve mass transfer within the liquid slug and across the gas-liquid interface. The widened channel then proceeded through an undulating zone that ensured that the fluid entering the heated zone was well mixed. Following the mixing zone, a 0.75 m long serpentine channel passes through the heated zone. A constant temperature is maintained in this region to allow reaction to occur. Finally, the channel passes back through the cooling zone before exiting the reactor. A 2500 Å layer of silicon nitride was deposited on the reactor. This improved the compatibility of silicon to strong bases, which could be required for certain catalyst systems.

The short length of the quenching zone is sufficient to cool the fluid stream. To provide an upper bound to the length required for cooling a simple two dimensional COMSOL Multiphysics simulation can be performed (Figure 2.10). A single liquid phase (toluene) was considered which provides a conservative estimate because recirculation in segmented flow improves heat as well as mass transfer. Fully developed flow passed from a constant temperature region (T_H = 200 °C) through a geometrically simplified halo region into the cooled region (T_C = 35 °C). A relatively fast flow of 50 µl/min (5.2 mm/s) was chosen to ensure the estimate is an upper bound. The simulation shows that the maximum variation between the channel and the center

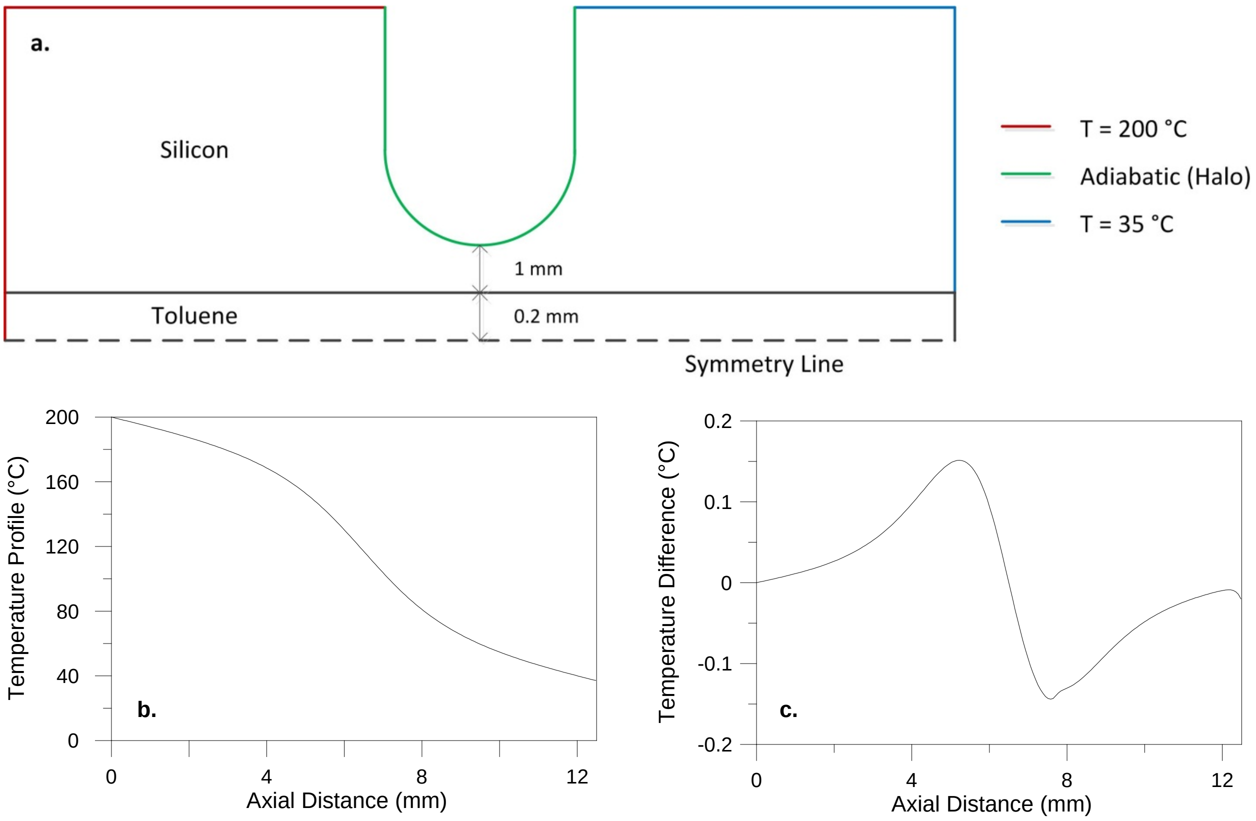

Figure 2.10. Simulation to verify the length of the quenching zone. (a) Simplified simulation diagram with boundary conditions. (b) Temperature of center of fluid channel, from heated zone to cooled zone. (c) The temperature difference between the wall and center of the channel.

of the channel, the point furthest from the wall, is 0.2 °C. This result suggests that the reaction will be quenched as long as the cooling zone is sufficiently cooled.

In total, the volume of the reactor is 160 µl, of which 120 µl is found in the heated zone. The total channel length was 1 m. The exterior dimensions of the reactor allowed four reactors to be manufactured on each 6 inch silicon wafer. A finished microreactor is shown in Figure 2.11.

Figure 2.11. Completed homogeneous microreactor.

2.3.1.2. *Initial Reactor Performance*

This first generation reactor was used to perform initial kinetic studies. Initial flow studies were conducted to ensure stable segmented flow. In nitrogen-water segmented flow, the reactor design performed well with stable segment flow present over the entire reactor (Figure 2.12a). However, when water was replaced by toluene, significant coalescence was observed towards the end of the reactor (Figure 2.12b).

The instability in the liquid phase extended over a wide range of gas-to-liquid ratios as well as flow rates. At the same flow rates and gas-to-liquid ratios, the size of each liquid and gas slug also varied. Differences in fluid properties clearly affected the stability of the segmented flow. Parameters that are likely relevant to bubble formation and segmented flow stability have been described in Section 2.1.3 above. Table 2.1 compares parameter values for water and toluene. Toluene has a lower density, viscosity, and surface tension when compared to water.

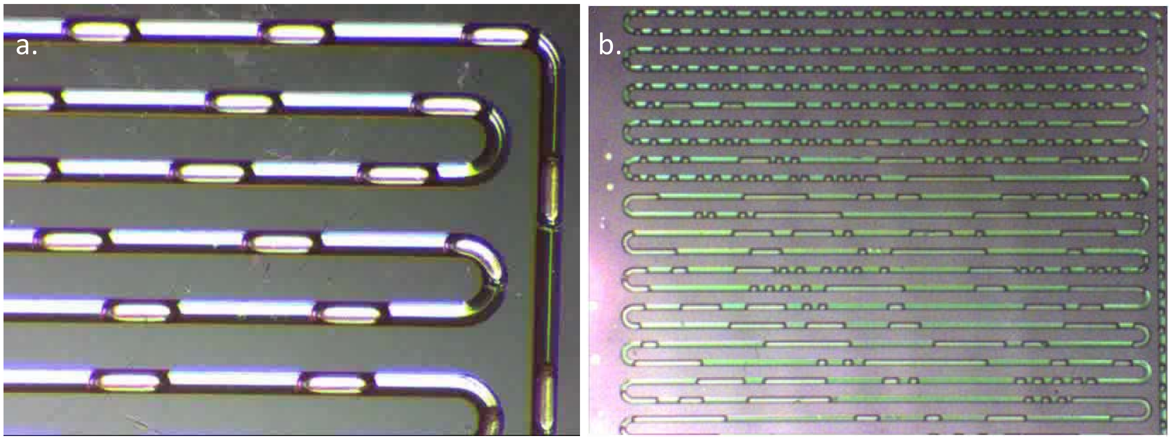

Figure 2.12. (a) Segmented flow comprised of nitrogen bubbles and water slugs. The segmented flow was very regular and did not coalesce over the length of the reactor. (b) When toluene was used as the liquid phase, significant coalescence was observed in the reactor.

Increasing the temperature of the heated zone further reduced the stability of segmented flow. At temperatures of greater than approximately 150 °C, the water-nitrogen segmented flow also began coalescing. Both viscosity and surface tension decrease as temperature increases. If water slugs coalesce above a certain temperature, the fluid properties likely crossed a critical value that toluene already crossed at room temperature.

Squalane, a viscous hydrocarbon, was added to the toluene (50%) to increase the mixture viscosity in hopes of improving segmented flow stability. This marginally improved the stability of the segmented flow. However, since the surface tension of both toluene and squalane are

	Water	Toluene	Squalane
Density (g/ml)	0.9982	0.8669	0.803
Viscosity (cP)	1.000	0.590	27.5
Surface Tension (dynes/cm)	72.8	28.5	28.0

Table 2.1. Property comparison of water, toluene, and squalane at 20 °C.[121]

essential the same and different from water, surface tension is likely the fluid property that most affects segmented flow stability.

Other attempts to improve the stability of segmented flow in the toluene case were to vary the pressure drop in both the gas and liquid lines upstream of the reactor. Specifically, PEEK tubing of 25 and 127 µm inner diameters and lengths varying from 10 cm to 1.25 m were added to increase pressure drop. Increased pressure drop improved the stability, but did not completely prevent coalescence. Ultimately long lengths of the 127 µm tube were used to provide pressure drop upstream of the reactor. This was mainly due to practical considerations around clogging of the very small inner diameter tubing. In particular, a disturbance that caused backflow could wick liquid into the PEEK tubing. In the case of 25 µm tubing, significant pressure was required to force the liquid out of the tube, which proved to be a challenge. The gas in the syringe pump (described in detail in Section 3.4) was compressible and had to be further pressurized to overcome this resistance.

Another possible cause of the instabilities was an unstable pressure environment downstream of the reactor. This thesis describes the first attempt to use an active pressure controller to control microreactor system pressure (described in detail in Section 3.3). While the controller provided excellent pressure control, ±0.02 bar of the set point, the needle valve was constantly actuating to control the overall pressure. These fluctuations might be enough to perturb the segmented flow leading to the observed coalescence. Alternately the constant fluctuations may have prevented steady state from ever being achieved.

It was also observed that the liquid slugs and gas bubbles were significantly shorter in the toluene case than the water case. Shorter slugs may prevent flow from fully developing, as described above. A gas-to-liquid ratio of approximately unity consistently led to the most stable flow. For example, the gas-to-liquid flow ratio was varied at constant liquid flow rate to determine the effect of bubble length on stability (Figure 2.13). In the case where $V_g/V_l = 3$, the length of the slug appeared to be smaller than the channel width. This would imply that the recirculation flow in the slug would not be fully developed. Increasing the gas-to-liquid ratio appeared to reduce the liquid slug length more than the ratio would imply. The rectangular cross section (Figure 2.3) captures significant liquid along the length of the bubble, reducing the apparent length of the liquid slug. The unit cell must contain a gas-to-liquid (volume) ratio set by the inlet flow rates for the continuity of mass condition to be satisfied.

The design of the T-junction and the expansion immediately following it might also contribute to variation in the lengths of the liquid slugs and gas bubbles that were magnified at long channel lengths. Specifically, the channel expansion occurs only a few channel widths from the final T-junction (Figure 2.14). It was hypothesized that allowing segmented flow to fully

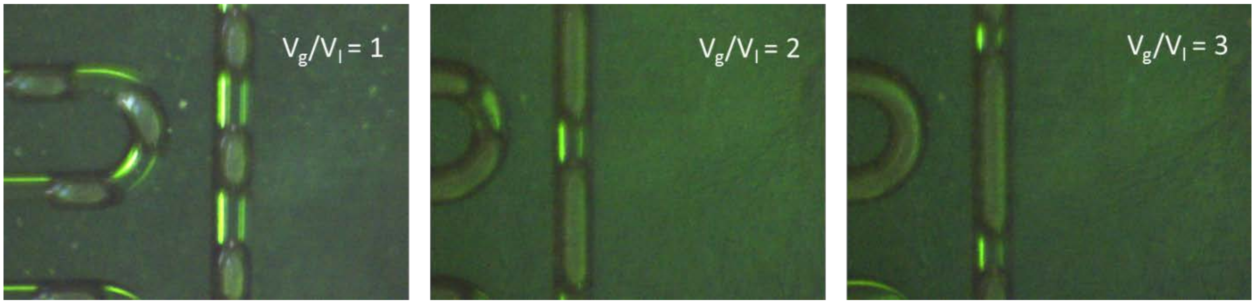

Figure 2.13. As the gas-to-liquid ratio is increased, the apparent liquid slug length decreases even as the overall liquid flow rate is held constant. Stability decreased with increasing gas-to-liquid ratios.

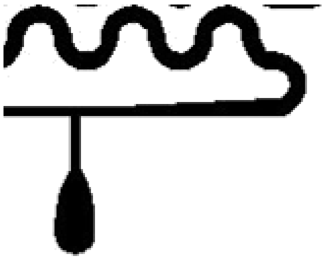

Figure 2.14. Third T-junction in the original design where the segmented flow typically formed. The bubbles extended to the start of the expansion zone prior to being pinched off.

develop prior to the expansion might improve the stability of the flow.

While it is difficult to pinpoint the exact cause of the instability in the segmented flow, a redesign might be able to address some of the observations. While fluid properties appear to have the largest effect on stability, it is not practical to vary the fluid for specific chemical systems. Instead, it appears that changes in the fluid properties have a direct effect on bubble and slug length, which may allow disturbances to magnify to the point that coalescence was observed. Varying the gas-to-liquid flow rate ratios or absolute flow rate has a very weak effect on bubble and slug length. The remaining lever is to vary the geometry of the T-junction which requires a reactor design.

2.3.1.3. Redesigned Reactor

A number of areas of the design were iterated in the second generation of reactors. Three different reactor designs were completed to address the instabilities in the previous section. In addition, higher flow rates at the same residence time were desired. By increasing the volume of the reactor, it would be possible to reduce the time between experiments. The new designs address one or more changes in the following list:

1. Increase the spacing between the T-junction and fluid expansion section. In addition, the fluid expansion section now expands symmetrically.
2. Remove the expansion section by having a constant width main channel.
3. Increase the volume of the reactor.

Both the first and second changes attempt to improve the stability of the segmented flow. Increasing the spacing between the T-junction and fluid expansion section will ensure that the recirculation flow in the liquid slug is fully developed. The second change should increase the size of the liquid slugs and gas bubbles. In addition, by removing the expansion section, the bubble and slug sizes are not reduced below their initial size. The final change enables higher flow rates at the same residence time. These higher flow rates enable increased experimental throughput by allowing the fixed minimum sample size to be collected more quickly.

The first microreactor design (Figure 2.15a) simply allowed the flow to further develop before

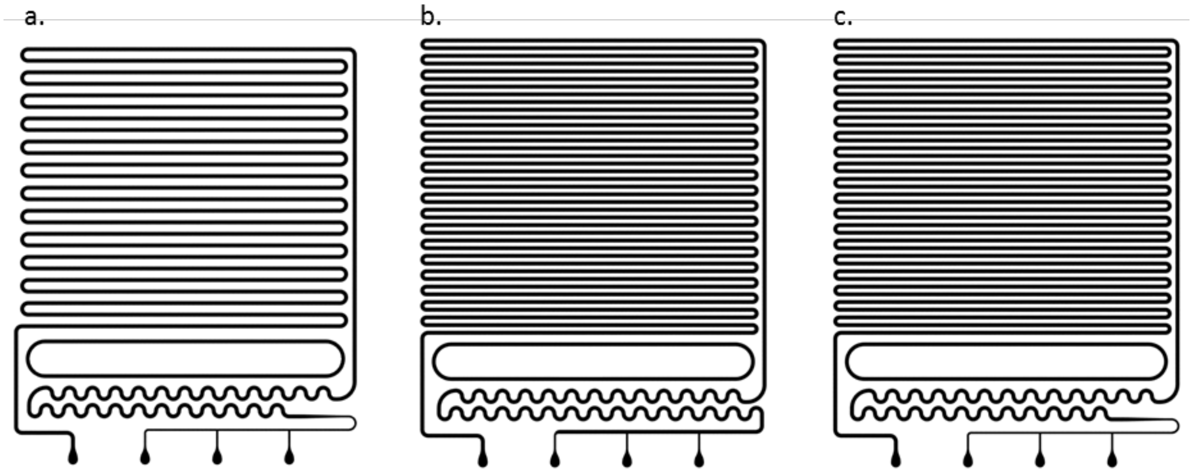

Figure 2.15. The three second generation reactor designs introduced new inlet and mixing zones as well as an increased reactor volume.

being expanded. The total length of the heated zone remained constant at 0.75 m. The inner radius of the turns in the heated zone of the reactor remained equal to the channel width, 400 µm. The second and third designs (Figure 2.15b,c) reduced the inner radius of the turns in the heated zone of the reactor to half the channel width or 200 µm. This enabled a total channel length of 1.6 m which leads to reactor volume of 260 µl, of which 220 µl are in the heated zone. This represents an 83% increase in the reaction zone when compared to the original reactors 120 µl reaction zone. The second design also removed the expansion section entirely and the main channel was widened to 400 µm. The third design is a combination of the inlet and mixing zone of the first reactor and the increased reactor volume found in the second reactor.

2.3.1.4. Second Generation Reactor Performance

The overall performance of the second generation reactors was similar to the first generation. Moving the expansion zone further from the T-junction did not have an observable impact on the overall stability of toluene segmented flow. Removing the expansion section and increasing the main channel width at the T-junction led to larger bubbles and slugs which appeared to improve the stability of the segmented flow. However, this improvement was offset by the increased channel length. Longer channels allow instabilities to grow and provide more time for coalescence to manifest itself. The reactor shown in Figure 2.15b was chosen to perform the final analysis for the homogeneous catalyst study due to its larger volume and adequate segmented flow stability.

2.3.2. Heterogeneous Reactors

2.3.2.1. Initial Design

The heterogeneous reactor was designed in conjunction with Bariş Ünal and based on his reactor design for studying high-pressure gas phase heterogeneous catalysis. The reactor, shown in Figure 2.16, was designed with eight parallel channels. A single inlet was shared by two adjacent channels. There were multiple inlets to ease loading of catalyst. Any curvature in a channel through which catalyst is loaded would result in clogging during loading. At the end of the main reactor channel, a weir with 40 µm posts and 20 µm channels was constructed as a catalyst retainer. Each pair of reactor channels proceeded to a single outlet. A large region of silicon was removed to improve the temperature gradient across the reactor. The exterior dimensions of the reactor are 5.7 cm wide by 7.6 cm long.

Figure 2.16. Eight channel, four inlet reactor for studying high-pressure gas phase heterogeneous catalysis. (Photo courtesy of Bariş Ünal)

To extend this design to multiphase flow, a few modifications were made to the single phase reactor design. The new reactor design is shown in Figure 2.17. Primarily, another inlet was required to introduce the second phase in a controlled manner. A single gas inlet was designed and joined to each of the eight main reaction channels. This gas inlet channel measures 200 µm in width. As the channel bifurcates, each half is identically symmetric to ensure that the pressure drops, and therefore the flows, are identical. A single outlet is used in this reactor design. The gas inlet lines preclude any extra outlets because channels would invariably cross. In addition, a single outlet simplifies the fluidic connections. The four inlets were maintained to enable easier loading of the catalyst. They will additionally be used as the liquid inlets since it is impossible to have both a single gas and liquid inlet without having channels cross if the reactor design is limited to two dimensions.

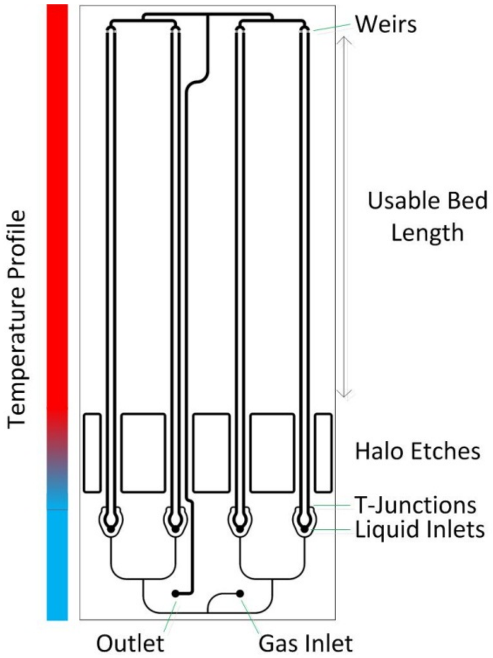

Figure 2.17. Initial heterogeneous reactor design. Eight parallel 45 mm long reaction channels allow up to 58 µl of catalyst bed volume to be loaded.

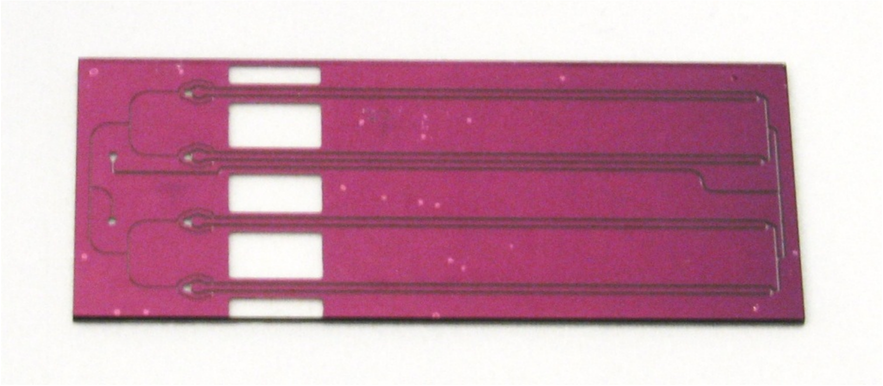

Figure 2.18. Completed multiphase heterogeneous microreactor.

A longer catalyst bed was included in this design by shrinking the length of the halo etched regions. The length of the heated region of a catalyst channel is now 47 mm. All features in this design are etched to a depth of 400 µm and width of all channels, other than the gas inlet channel, is also 400 µm. With 8 parallel channels, the maximum volume of catalyst that can be loaded in this reactor is 58 µl. In addition, the spacing between the ports on the reactor shrank to the minimum spacing that allows a wrench access to the fittings on the reactor chuck. This spacing is now 8 mm which also enables the reactor width to be narrowed to 3.2 cm from 5.7 cm. This reduction allows four (two additional) reactors to be fit on a single 6 inch silicon wafer, reducing fabrication costs. A completed microreactor is shown in Figure 2.18.

2.3.2.2. *Initial Reactor Performance*

It proved impossible to achieve stable flow using the initial design. Pressure drops prior to the reactor were varied in an attempt to tune the flow, but failed to have any impact. Flow was never observed simultaneously in two adjacent liquid channels. In addition, flow redistributed through the gas inlet lines. This behavior had been previously reported for a reactor without balanced pressure drops.[122]

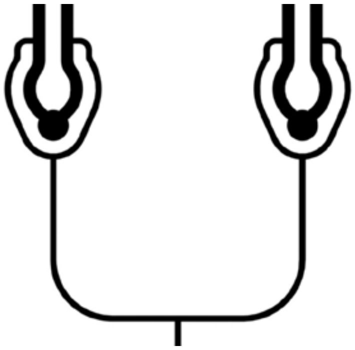

Figure 2.19. Detailed view of the inlet section of the first generation multiphase heterogeneous reactor. Pairs of channels share a common liquid inlet and the gas inlet allows communication between adjacent pairs of channels.

Small differences in pressure drop between channels led to the poor flow distribution. Multiphase flow led to further differences in pressure drop. Gas, due to its lower density and viscosity, has a much lower pressure drop in the packed bed than does liquid. The design of the inlet region of the channel (Figure 2.19) had a very low pressure drop between adjacent channels and low pressure drop between pairs of channels through the gas lines. Both of these pressure drops were dwarfed by the pressure drop across the bed. A new reactor design was required to refine the flow.

2.3.2.3. Second Generation Heterogeneous Reactor

A second generation reactor had an improved pressure drop design. Given the flow distributions observed in the first generation design, two new reactors were designed, differing only in the length of the gas inlet pressure drop channel. The new design improved the design by satisfying two pressure criteria:

1. Pressure drop in the inlet channels must be greater than in the packed bed to ensure that flow does not redistribute through the inlet channels.

2. For stable bubble formation, pressure drop in the gas inlet channel must be greater than the pressure fluctuations associated with bubble formation.

The first criterion, while conservative, should ensure that all channels have identical flow. For a packed bed of any practical length, the second criterion should be met if the first is.

The first criterion affects both the gas inlet channels as well as the liquid inlet channels. The liquid inlet channel serves two purposes: liquid inlet and catalyst loading. Catalyst is loaded into the channel manually, which requires a wide channel. Thus it is not possible to have a single liquid inlet serving two channels; there is no way to have a pressure drop between the channels to ensure that the liquid flow is distributed between the two. Thus the second reactor design has the number of parallel channels reduced from 8 to 4. The first criterion is satisfied by introducing the pressure drop *outside* the reactor. In the new design, each channel is fed by its own liquid port. A single line from the liquid pump is split into four lines which are then connected to the reactor. By using 8 inch long, 127 µm ID PEEK tubing, the flow can be distributed between the four channels with a high pressure drop.

A similar redesign of the gas inlet is required to preclude flow distribution through those inlets. It is possible to fabricate reactors with features of two different depths, specifically one very shallow depth followed by a second arbitrary depth. Features of up to 10 µm in depth can be achieved using this technique. A square channel with sides of 10 µm in length was chosen. Pressure drop in a channel with a single liquid phase can be described using the Hagen–Poiseuille equation,[123]

$$\Delta P = \frac{128\mu LQ}{\pi D_h^4} \tag{2-14}$$

where ΔP is the pressure drop, μ is the kinematic viscosity, L is the length of the channel, Q is the volumetric flow rate, and D_h is the hydraulic diameter. The viscosity is a fluid property, the flow rate will be varied, and the hydraulic diameter was fixed by fabrication limitations. The remaining degree of freedom is the length of the pressure drop channel.

The Ergun equation (Equation 2-11) can be used to estimate the pressure drop through the packed bed. The Ergun equation was developed for flow of a single phase and is hard to extend to multiphase flow. It is impossible to estimate liquid holdup in a multiphase packed bed, which would be required to extend the Ergun equation to multiphase flow. A number of correlations for pressure drop through a trickle bed have been proposed, but are difficult to apply outside of the experimental conditions used to fit them.[124, 125] These correlations have not been applied to microsystems in the literature. A very conservative estimate of the pressure drop across a packed bed in gas liquid multiphase flow would be to calculate the pressure drop as though the total flow rate was liquid. Thus both the pressure drop in the gas inlet and in the bed is a function of the gas flow rate; the pressure drop in the liquid region is a function of the liquid flow rate. To satisfy the first criterion, the pressure drop in the inlet channel must be greater than the pressure drop in the bed. To determine the required length of the pressure drop channel, the ratio of the inlet to bed pressure drop were compared against possible gas-to-liquid flow rate ratios at different pressure drop channel lengths (Figure 2.20). For a pressure drop inlet length of 300 mm, the pressure drop in the inlet channel was 4-10 times greater than the pressure drop in the longest packed bed that could be loaded into the

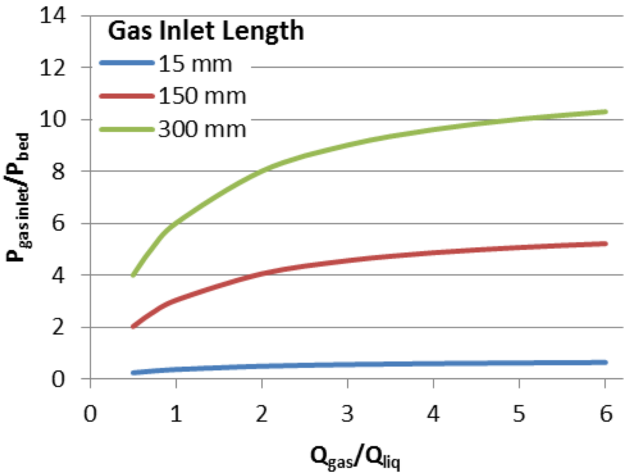

Figure 2.20. To determine the length of the pressure drop channel, the ratio of the pressure drop in the gas inlet to the pressure drop across the bed was calculated for various gas-to-liquid ratios.

reactor. Wada et al.[122] demonstrated a multiphase silicon packed-bed reactor whose pressure drop channels were designed to have 40 times higher pressure drop than the main channel.

Ultimately, two reactor designs were fabricated. In the first, the very conservative channel length of 300 mm was used. In the second, a 12 mm pressure drop channel was chosen. The tradeoff between certain stability at 300 mm is very slow dynamics associated with changes in pressure or when starting up the system. It was therefore worth trying a shorter channel to see if stable flow could be achieved more quickly. A comparison of the two inlet designs is shown in Figure 2.21a-b. The final 4 channel design is shown in Figure 2.21c. To reduce the chance of clogging, a weir similar to the one that retains the catalyst in the main channel was added to the inlet and the outlet of the gas pressure drop channels. The remaining dimensions remained identical to the first generation design. The total catalyst bed volume was halved allowing for 29 µl of catalyst to be loaded.

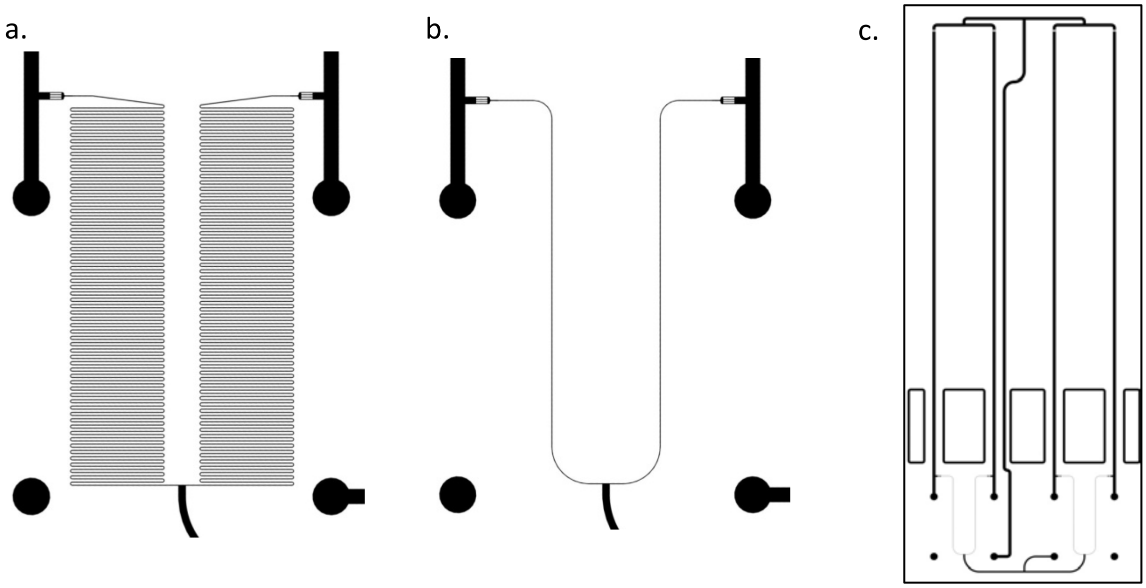

Figure 2.21. Detailed view of the 300 mm (a.) and 12 mm (b.) pressure reduction channels. The entire second generation reactor design is also shown (c.).

2.3.2.4. *Second Generation Reactor Performance*

The newly designed second generation reactor immediately achieved stable segmented flow in all four channels, using both the short and long pressure drop designs. A photograph of the segmented flow can be found in Figure 2.22. In this example, 20 µl/min of cyclohexene and 80 µl/min of hydrogen are flowing through the reactor at 30 bar. While not visible in the photograph, a standing bubble exists at the bed inlet. Liquid slugs collapse and bypass the bubble through the corners. Segmented flow reforms at the catalyst retaining weir. Bubbles and slugs coalesce at each junction where the streams recombine.

It is interesting that both the short and long pressure drop channels resulted in essentially identical flow distributions. The short pressure drop was able to achieve stable flow five times more quickly and thus was the preferred reactor design. The bed was also never filled greater than 60%, which would also reduce the amount of pressure drop required in the gas inlet. In

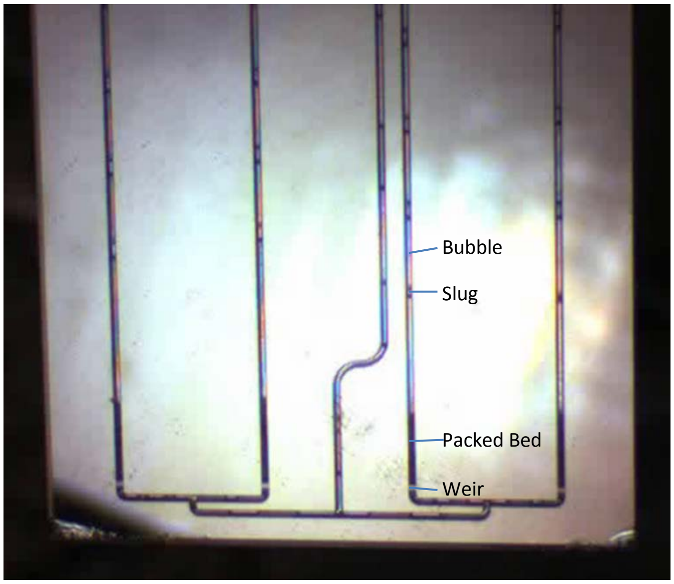

Figure 2.22. Photograph showing stable gas-liquid flow, at 30 bar, in a multichannel heterogeneous reactor.

addition, the pressure drop calculated for the bed was certainly high; the pressure drop for gas-liquid flow is always less than the pressure drop for a single liquid phase at the same flow rate. The fact that the shorter reactor design worked suggests that the criterion that the pressure drop in the gas inlet channel be greater than the pressure drop across the bed was too conservative. The pressure drop preventing flow between adjacent channels may only need to be greater than the *difference* in the pressure drop in those channels. The initial criteria would ensure stable flow, which was unintentionally observed, in the case where one channel had catalyst and the second had none.

2.4. Reactor Fabrication

All microreactors were fabricated using the same process in the fabrication (cleanroom) facilities in the Material Technology Laboratories at MIT. A general discussion of the fabrication procedure is included in this section. A detailed procedure can be found in Appendix A, along with all photolithography masks, which define the two dimensional layout of the reactors.

Bare 650 µm thick double side polished wafers were deposited with 5000 Å of low pressure continuous vapor deposition (LPCVD) silicon nitride to provide a sacrificial layer which will protect the bonding surface of the silicon wafer during processing (Figure 2.23a). A 10 µm layer of positive photoresist is spun onto the topside of the silicon. The photoresist serves as a mask for subsequent etch steps. Using a transparency mask, it is possible to expose the photoresist to high intensity light which modifies the structure of the polymer (Figure 2.23b). The exposed region is soluble in the corresponding developer exposing the silicon surface underneath. Using photolithography techniques, any two dimensional pattern can be exposed on the surface of the silicon wafer. The front side mask is used to expose the photoresist and developed.

Deep reactive-ion etch (DRIE) is used to etch the pattern 400 µm into the wafer (Figure 2.23c). Two steps are repeated sequentially to enable anisotropic etching with very high aspect ratios. In the first step, a standard silicon isotropic etch is combined with ions that vertically bombard the surface of the wafer. The second step deposits a chemically inert passivation layer on all exposed surfaces. This layer protects the side walls from the isotropic etchant and is removed from the bottom of the feature by ion bombardment during the first step. The silicon nitride coating is not a good mask for DRIE, and is readily removed. The remaining photoresist is removed, and the entire process is repeated on the back of the wafer (Figure 2.23d). The only features typically found on the back of the wafer are features that are present on both sides of the wafer, such as the halo etched regions and fluidic ports. The backside of the wafer is spun with photoresist, exposed, developed, and etched to a depth of 250 µm. In the second generation design for the multiphase heterogeneous reactor, two masks were used to pattern the front side of the wafer. Prior to patterning the 400 µm deep features, the pressure drop channels were pattered to a depth of 10 µm. This depth was chosen specifically because it is shallow enough that a second application of photoresist, required for the second front-side mask, will completely fill these features.

The sacrificial layer of nitride is removed in hydrofluoric (HF) acid. Silicon nitride is etched at a rate of 200 Å/min by HF while the silicon wafer is impervious. Following removal of the silicon nitride layer, found only on the top surface of the wafer, a fresh LPCVD silicon nitride layer is deposited which covers the entire wafer, including the walls of the etched channel. A Pyrex wafer is then anodically bonded to the wafer to form the fourth wall of the channel (Figure 2.23e). During anodic bonding a potential is applied across the heated silicon and Pyrex wafers. Sodium ions in the Pyrex wafer migrate under the electric field away from the Pyrex-silicon interface. The depletion of sodium ions increases the reactivity of the glass with the silicon, enabling strong bonds to form. Once bonded, the wafer is diced into individual reactors using a diamond saw (Figure 2.23f).

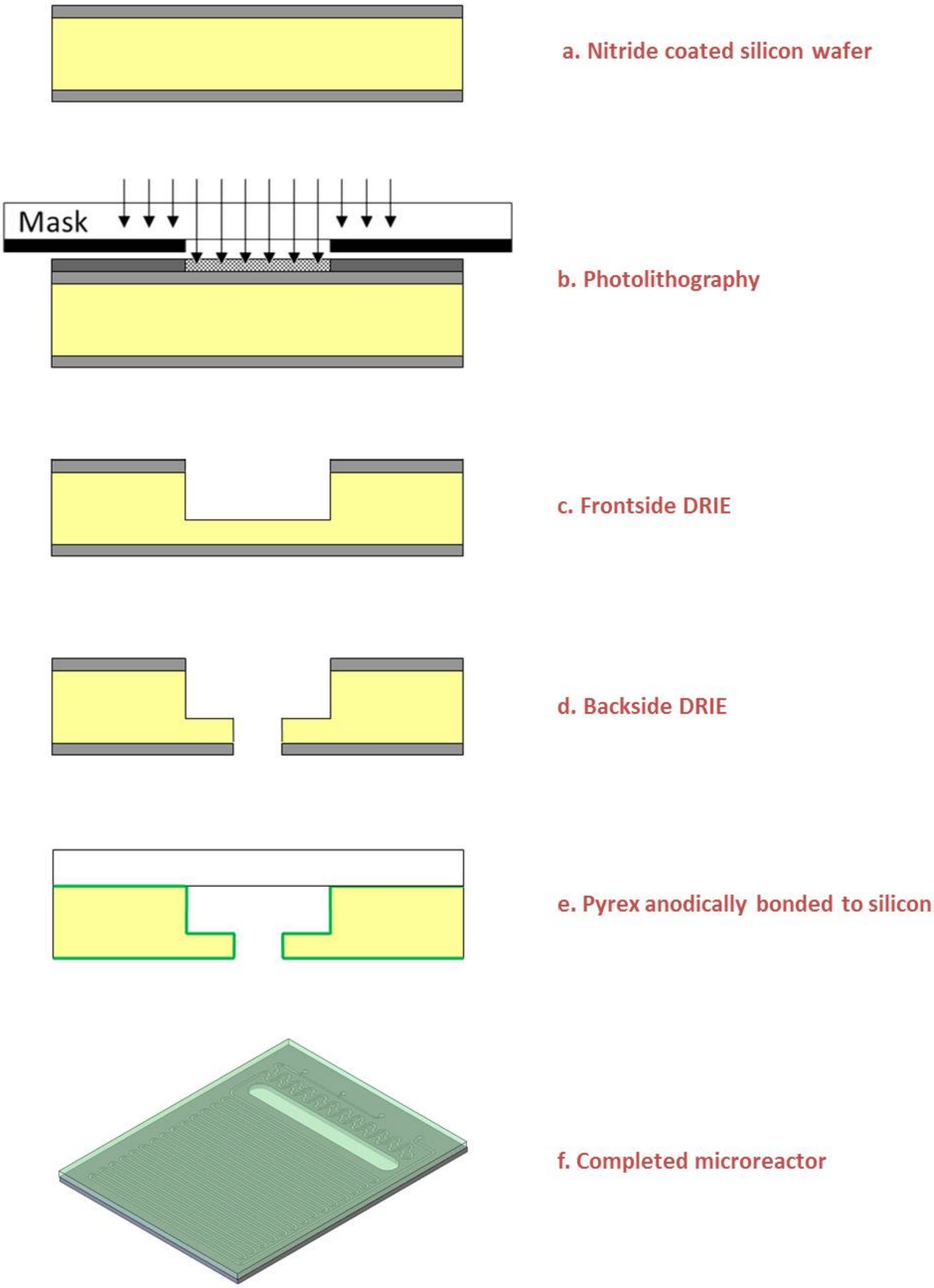

Figure 2.23. Key steps in the microfabrication of homogeneous silicon microreactors.

Chapter 3. System Components and Construction

3.1. Requirements

The design of a high-pressure microreactor support system is necessarily challenging. Many pieces of traditional equipment are simply too large to integrate seamlessly with microscale flow. Invariably, the supporting system has dimensions that dwarf the microreactor. A set of requirements (Table 3.1) was drafted that guided the design of the final system. The system is modular, allowing it to be modified to suit the changing requirements of the homogeneous or heterogeneous reactors. The primary challenge was combining stable high-pressure operation at low flow rates with analysis of the reactor effluent.

	Condition
Pressure	~100 bar
Temperature	Room temperature → 350 °C
Residence Time	Seconds to minutes
Analysis Methods	Online (preferred) and offline
Safety	Considered at all stages

Table 3.1. Summary of conditions that must be attainable in system.

The desired upper pressure limit for the system was on the order of 100 bar. Pyrex/silicon microreactors have been demonstrated to achieve pressures of 300 bar,[52] which could be considered an upper bound for the system as designed. A lower pressure was chosen because the goal was to study high-pressure reactions, which for industrial processes are run at pressures around 50 bar. Ultimately, the system pressure was limited by the back pressure controller, which had an upper pressure limit of 100 bar. The maximum temperature of the system is localized to the heated zone of the reactor and the heating elements. Therefore the temperature would be limited by the Pyrex-silicon bond, which has been previously operated under pressure at temperatures of 400-500 °C.[52] The residence time of the system was limited by the size of the microreactors. Online analysis is greatly preferred to offline analysis due to the quicker and more frequent analysis that this method allows. Quantitative reproducibility is also greatly valued and a number of offline techniques such as gas chromatography (GC) or high-pressure liquid chromatography (HPLC) have been shown to be reliable analysis techniques. Lastly, safety was considered throughout the design and construction of the system. The two most significant identified hazards were chemical toxicity and high-pressure operation.

3.2. Overall System Design

The completed system is constructed from a number of systems that work in concert to enable kinetic measurements at high temperature and pressure. The completed system for the homogeneous reactor case (Figure 3.1) consists of components organized together into major systems such as the pressure-control system, gas-handling system, temperature-control system, and analysis system. The pressure control system allows for the precise control of pressure independent of flow rate. The gas-handling system allows for the preparation of reproducible gas mixtures from up to three gas components, as well as delivering the mixture to the microreactor. The temperature control system controls both the heated and cooled zone of the microreactor. Finally, the analytic system consists of both online Fourier Transform Infrared (FTIR) spectroscopy and offline sampling infrastructure.

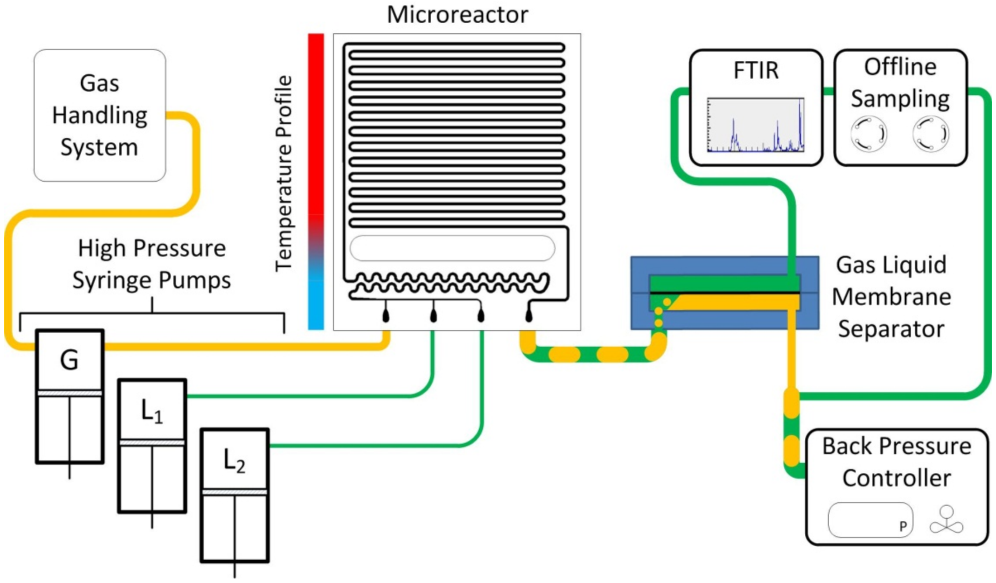

Figure 3.1. Schematic of the high-pressure system interfaced with a homogeneous microreactor.

The entire system was constructed in a modular manner. This allowed for the addition and removal of components as necessary. For example, it was determined that the multiphase flow must be phase-separated prior to the analysis system for accurate analysis. Therefore, a gas-liquid membrane separator was built and introduced into the system. The modular nature also allowed for the system to be rearranged while searching for stubborn leaks or clogged tubing. Each system was designed independently and is described in detail below.

3.3. Pressure Control System

The pressure control system consists of two major classes of components: a back pressure controller to regulate the system pressure and syringe pumps to deliver fluid. Identifying a back pressure control scheme that worked with microliter per minute flow rates at pressures of up to 100 bar proved to be a significant challenge. Prior microreactor systems have used two basic approaches for controlling pressure: large pressure drop at the outlet of the system or a reservoir system with a purge/bleed arrangement. The simpler arrangement is to provide a pressure drop at the outlet of the system using a small-diameter tube or a needle valve. Under this arrangement, pressure drop remains a function of fluid properties and the overall system flow rate. Pressure drop cannot be determined independently of flow rate. A needle valve allows for some tuning of pressure drop if flow conditions are varied, but either system is slow to achieve steady state in the presence of compressible fluids such as gas.

An improvement to this arrangement is to add a reservoir just before the outlet of the system. Three connections are required for the reservoir: an inlet from the microreactor, a constant-pressure gas inlet, and an outlet. The pressure in the system is supplied from a gas cylinder with a regulator set to the desired pressure. The leak from the system at the operating pressure must be greater than the overall flow rate through the microreactor. The difference between the outlet and inlet flow rates is supplied by the gas cylinder to maintain the set pressure. The reservoir must be large enough to collect the total volume of liquid that will flow through the system in a given experimental run. While rarely limiting, the reservoir must be large enough to allow gravity-based phase separation to occur. Using this configuration, the system flow rate and the system pressure are largely decoupled. This arrangement has two disadvantages: the relatively large reservoir volume can pose a safety risk and the increased risk of backflow.

A third approach would be to use an active back pressure controller and active-control valve. A suitable controller, EL-PRESS was purchased from Bronkhorst (Figure 3.2a). This system has the advantage of actively controlling back pressure in the system and was capable of controlling

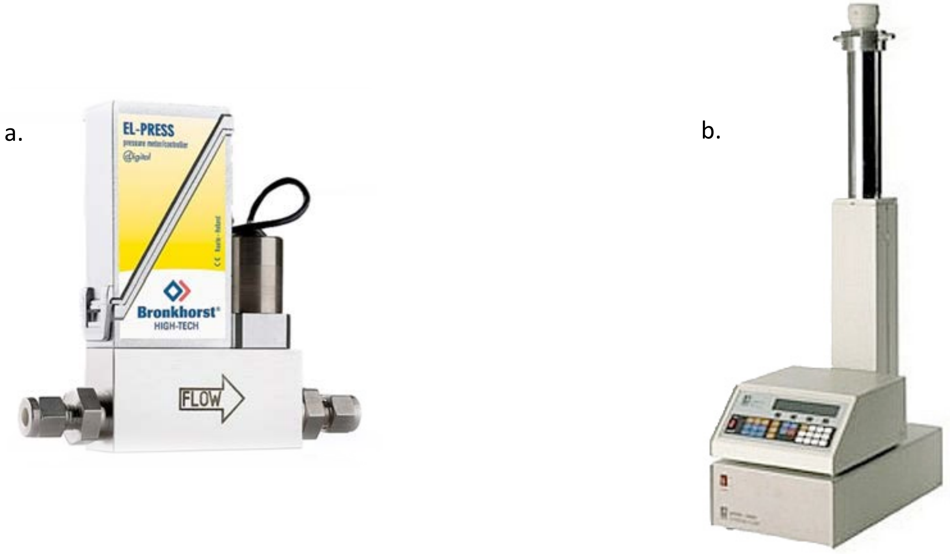

Figure 3.2. Two primary components of pressure control system: a) EL-PRESS back pressure regulator, consisting of a controller (left) and valve (right). b) Teledyne Isco 100DM high-pressure pump capable of pulse-less flow at flow rates of 1 µl/min and pressures of over 600 bar.

very low flow rates at pressures of up to 100 bar within ±0.02 bar of the set point. A Kalrez polymeric seal around the valve was chosen for its high chemical compatibility. This system is capable of controlling pressure as the fluid flow rates are varied. The internal volume of the back pressure controller is approximately 2 ml which is much lower than the volume of a reservoir.

The high-pressure syringe pumps that deliver gas and liquid to the microreactor make up the second half of the pressure control system. Syringe pumps have traditionally been used to deliver liquid to a microreactor at low pressure. The Teledyne Isco 100DM syringe pump was identified as being capable of driving high-pressure flows at very low flow rates. The pump is capable of pulse-less flow at flow rates of under 1 µl/min and pressures of over 600 bar with a syringe volume of 100 ml. Each pump has two connections: the first is connected to the microreactor system and the second is used for loading. These pumps are unique in that they can be operated in constant pressure mode as well as constant displacement mode. Traditional syringe pumps, such as the Harvard Apparatus PHD2000 series, are capable of slower flow rates using smaller syringes, but have difficulty driving high pressures. Gas has traditionally been controlled using mass flow controllers with the gas cylinder pressure driving the flow. However, no mass flow controllers were found to be capable of matching the low flow rates of the high-pressure syringe pumps at elevated pressures. Instead, a second syringe pump was used to deliver gas to the system. The syringe pump consists of a vertical, cylindrical chamber with two seals: a stationary, deformable seal at the top of the syringe and a moving piston seal at the bottom of the cylinder. When the syringe pump was pressurized with gas, small leaks were observed and were suspected to come from the moving seal. A 3 ml sample of very low vapor pressure Fomblin oil was added to the gas syringe pump to wet the moving seal at the bottom of the syringe. This oil pooled at the bottom of the syringe and provided a liquid interface between the moving seal and the syringe and greatly improved the ability of the syringe to pump gas. This solution was only possible because of the vertical orientation of the syringe. A second liquid syringe pump was eventually added to the system to enable liquid reactants to be isolated prior to reaction. A single Teledyne Isco Controller was able to control up to four pumps and could also interface with a computer.

3.4. Gas Handling System

The high-pressure syringe pump described in the previous section was capable of delivering a single stream of gas to the reactor system. This necessitated loading the syringe pump with a gas mixture. The pump would be loaded in much the same manner as a traditional bomb reactor – successive pressurization with each gas. A computer-controlled gas handling system was designed for this purpose (Figure 3.3). Automation of the filling increased reproducibility of the resulting mixture.

The gas handling system was initially designed by outlining the required fluidic and electric connections (Figure 3.3). The system was intended to allow mixtures of three gases to be mixed. The gas handling system thus required three pneumatic valves to control the flow of the three gases, nominally carbon monoxide, hydrogen, and nitrogen. In addition, a valve was required to vent the contents of the system to the hood. A valve was also included to control access to a vacuum pump that would allow the system be evacuated to reduce cross contamination. A final valve controlled flow to the gas syringe pump. The original design called

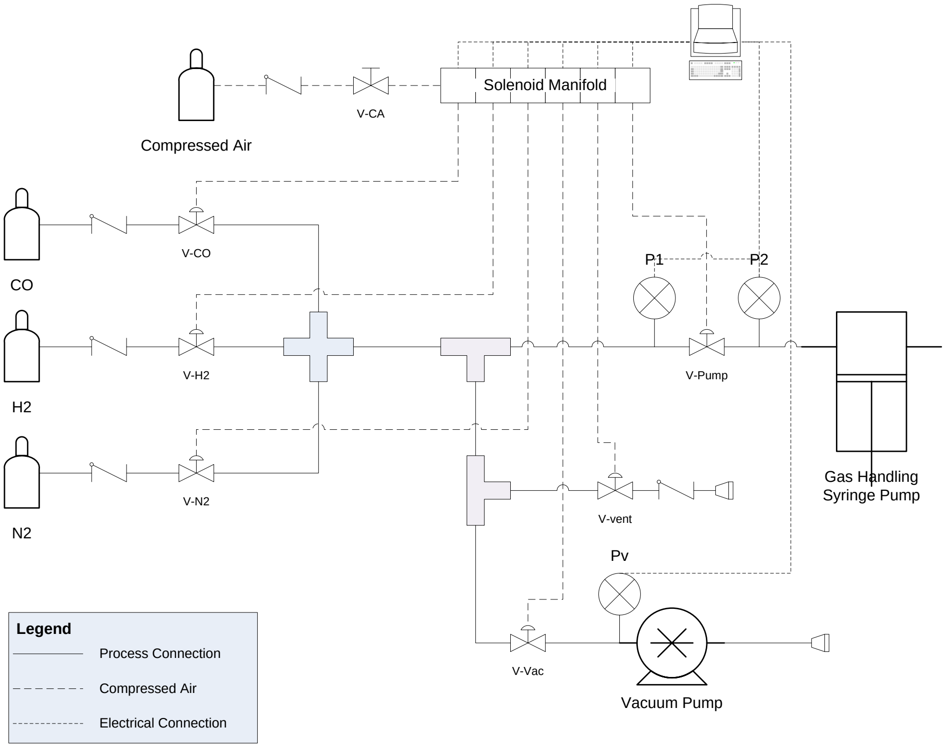

Figure 3.3. Schematic of gas handling system illustrates the required valves, transducers, and control system.

for three pressure transducers: to measure the pressure inside the system, to measure the pressure in the line between the system and the syringe pump, and to measure the vacuum level. Ultimately, the pressure transducer between the system and the syringe pump was removed and the pressure transducer in the gas syringe pump was monitored instead.

The normally closed pneumatic valves are actuated using high-pressure air. The required pressure to operate the valve is 80 psig, which was typically provided by the house high-pressure compressed air feed. The air was switched using computer-controlled solenoid valves. A solenoid valve was required for each pneumatic valve; the six solenoids were arranged in a manifold with a single high-pressure air inlet. Both the control of the solenoid valve and the monitoring of the signal voltage from the pressure transducers were performed using a data acquisition/switch unit, an Agilent Unit 34970A with two different plug-in modules: Multiplexer 34901A and Actuator 34903A. This switch was computer-controlled.

To ensure the most reliable and leak-free system possible, it was decided to construct the system using VCR fittings. VCR fittings form a seal using a deformable, single-use metal gasket. The smallest tubing size compatible with VCR fittings is 1/4 inch. This size of tubing requires a tool to make precise bends, which must be made before attaching to the system. In addition, VCR fittings must be welded onto the stainless steel tubing. As a result, the schematic shown in Figure 3.3 was adapted into a SolidWorks model (Figure 3.4), ensuring that the welded tubes are the proper length and corners occur at the proper location. The finished gas handling system (Figure 3.5) was mounted onto sheet metal that was hung vertically in the hood to conserve space. Precise placement of screw holes was required to mount the system onto the

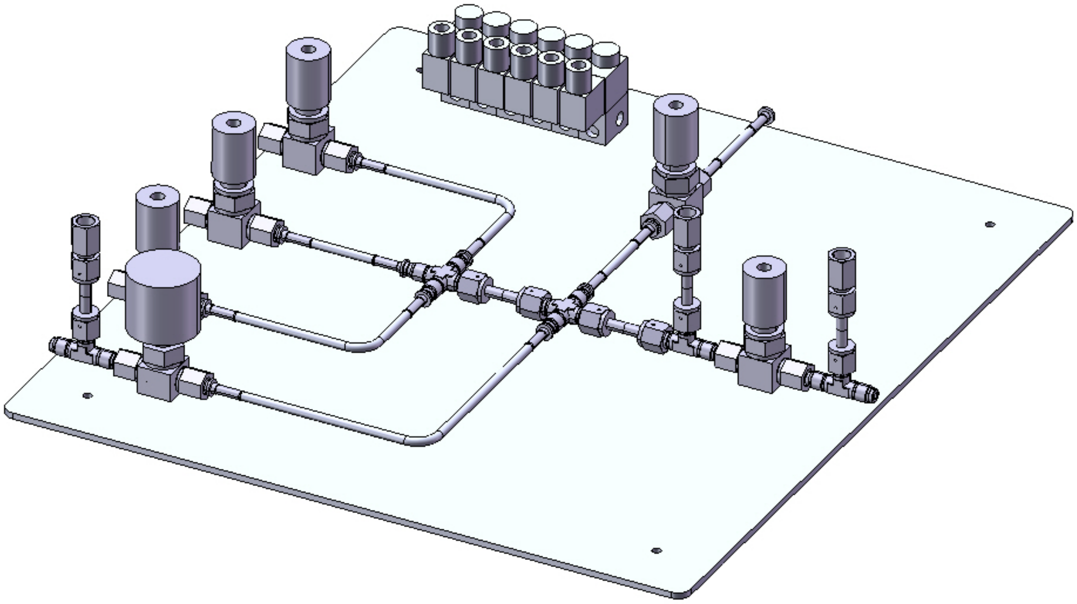

Figure 3.4. SolidWorks representation of gas handling system which provides a spatial model.

sheet of metal. The final SolidWorks model was used to control an abrasive water jet cutter, which cut the sheet metal.

Initially, the pressure in the pump was controlled by closing the pneumatic valve when the desired pressure was reached. In practice, the pump filled so quickly that the system had no ability to control the pressure. Thus a manual three-way valve was added downstream of the gas handling system (see Figure 3.6). In the first position, a large inner-diameter tube (0.03 in) allowed for quick filling and evacuation of the gas syringe pump. In the second position, a 5 foot length of 0.005 in inner diameter tubing was used to increase the pressure drop and restrict the flow. The pump filled much more slowly and the final pump pressure was decoupled from the pressure of the gas leaving the gas cylinder. Unfortunately, the volume of gas between the pneumatic valve and the pressure reducing tube prevented reproducible filling of the syringe pump because the pump continued to pressurize even after the valve was closed.

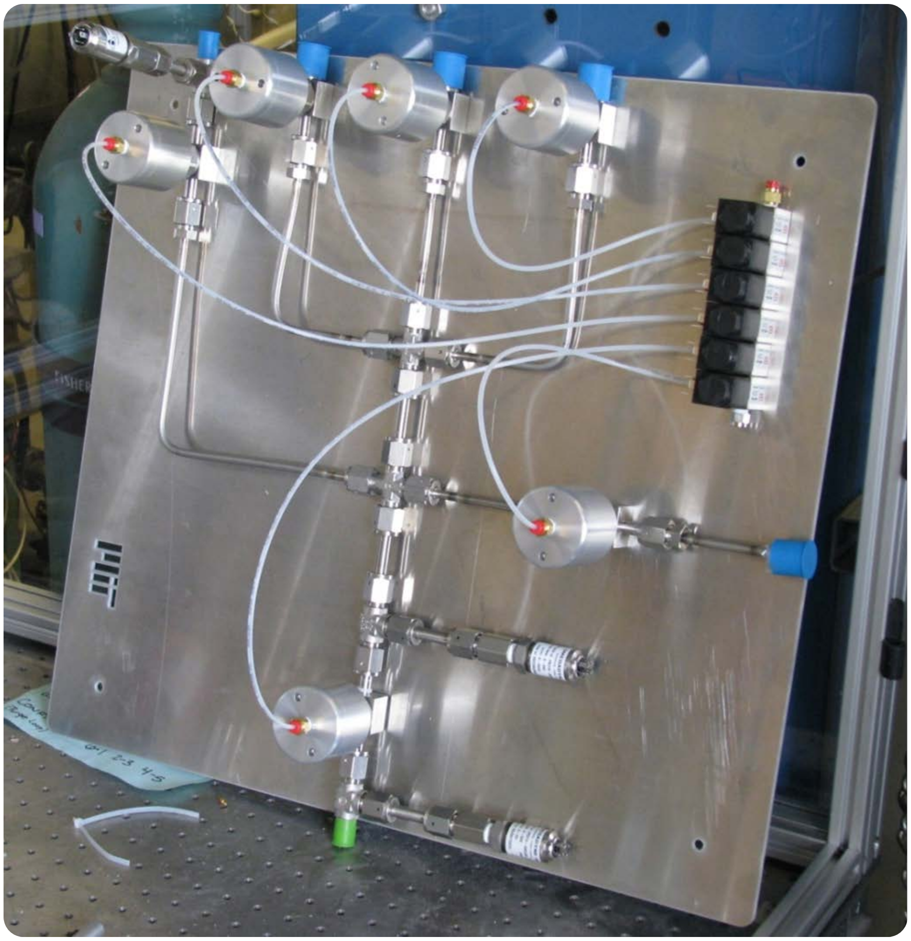

Figure 3.5. Assembled gas handling system.

A line was added connecting this region to the back pressure controller, which was used to bleed off this excess gas after the pump reached its desired pressure. Reproducible gas mixtures were then achieved.

3.5. Liquid Handling System

The liquid handling system consists of the liquid syringe pumps described above and a series of lines connected to one of the two pumps (Figure 3.7). These modifications enable loading of liquid samples while excluding gas, and in particular air, from the liquid pump. The inlet side of the pump was connected to a tube terminated with a syringe-compatible Leur Lock fitting. The

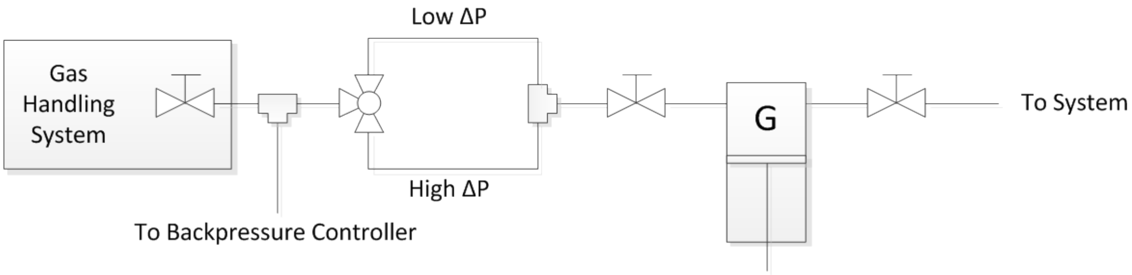

Figure 3.6. Schematic of the interface between the gas handling system and the gas syringe pump.

outlet of the pump is attached to a three-way valve. The pump attaches to the common port of the three-way valve and the first switched port is attached to the microreactor system. The second switched port is attached to a second three-way valve that is attached to low-pressure nitrogen and vacuum lines. The high-pressure syringe pump, even when "empty" holds a few milliliters of fluid. Opening the inlet valve and flowing nitrogen backwards through the pump can force the remaining fluid from the system through the inlet. The pump inlet can then be sealed and evacuated, evaporating any remaining solvent. Evacuating the pump additionally ensures that no gas remains in the pump prior to liquid loading.

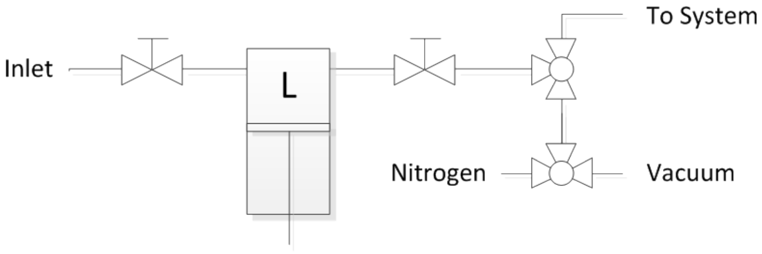

Figure 3.7. Schematic of the liquid handling system, highlighting the nitrogen and vacuum connections. This system enables the exclusion of oxygen during liquid loading.

3.6. Microreactor Fluidic Connections

The microreactor was interfaced with the rest of the system using a compression chuck that was previously developed in the Jensen group and could be operated under high-pressure conditions.[52] A chuck must be designed for each port design. For this work, two chucks were required: one for the four-port homogeneous reactor and one for the eight-port heterogeneous reactor. The compression scheme consists of a stainless-steel chuck that interfaces with standard 1/16” compression fittings on one side and the microreactor on the other. The holes on the chuck are aligned with through-holes etched through the silicon of the microreactor. Fluorosilicone O-rings (O-Rings Inc, M25988/1-005) fit into grooves on the chuck and form a compression seal against the silicon microreactor. Compression force is applied by a stainless steel plate screwed to the chuck. A Pyrex window distributes the force on the Pyrex side of the reactor. Parallel channels for active water cooling are machined through the chuck, perpendicular to the fluidic connections.

The four-port reactor chuck was designed for reactors with a port spacing of 7.5 mm and has two water cooling channels machined through the chuck. The eight-port chuck standardizes on port spacing of 8 mm and has three water cooling channels. Both chucks are compressed in the same manner. The four-port reactor uses coned stainless steel compression fittings (Vici Valco, ZP1), whose ports are more difficult to machine. The eight-port chucks uses flat-bottom polymer fittings (Upchurch M-250). CAD drawings of both reactors are shown in Figure 3.8 for comparison.

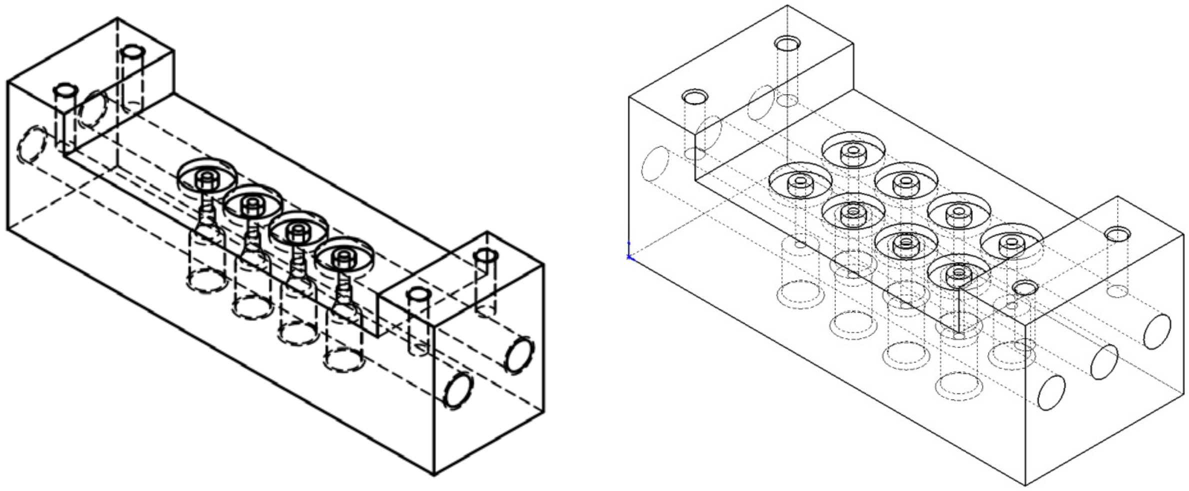

Figure 3.8. Left: Four-port compression chuck with coned ports. Right: Eight-port compression chuck with flat-bottomed ports.

When redesigning the chuck for the eight-port application, materials other than stainless steel were considered in an effort to reduce cost. For example, PEEK and aluminum are much easier to machine than stainless steel. In particular, PEEK is an attractive material because it exhibits very high chemical compatibility and is regularly used for high-pressure tubing and fittings. When designing a high-pressure chuck, the likely failure mechanism is deformation that leads to cracking of the silicon reactor, rather than total failure. The maximum deformation can be calculated as follows:[52]

$$d = d_1 + d_2 \tag{3-1}$$

$$d_1 = \frac{F\varepsilon l^2}{8EJ} \tag{3-2}$$

$$d_2 = \frac{qc}{384EJ}\left(c^3 - 4lc^2 + 8l^3\right) \tag{3-3}$$

$$F = Pbc/2 \tag{3-4}$$

$$J = h^3 b / 12 \qquad \textbf{(3-5)}$$

where d, d_1, d_2 are total deformation, force deformation, and bolt deformation, respectively, E is the elastic modulus of the chuck material, F is the force applied by the bolt, J is moment of inertia of the compression plate, and P is the system pressure. The remaining variables are geometric parameters and are defined in Figure 3.9.

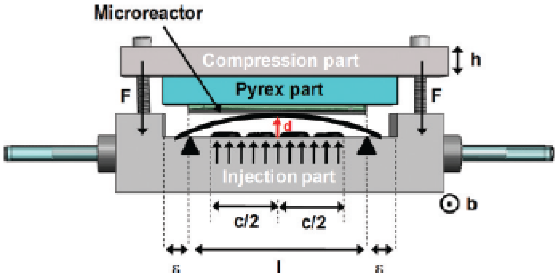

Figure 3.9. Geometric parameters required for calculating reactor deformation in a high-pressure reactor chuck.[52]

Under operating conditions, the maximum deformation of a Pyrex/silicon microreactor is on the order of a few microns. Summarized in Table 3.2, the results show that PEEK exhibits too large a deformation. Aluminum might work but lacks the chemical compatibility of stainless steel. Ultimately, the chuck was also constructed out of stainless steel.

Material	Young's Modulus (GPa)[126, 127]	d (μm)
Stainless Steel	200	90
PEEK	3.6	5020
Aluminum	69	260

Table 3.2. Total displacement deformation for the eight-port chuck constructed from a variety of machinable materials.

All remaining fluidic connections in the system were made using commercially available tube fittings. In general, three competing types of fittings were used: stainless steel Swagelok tube fittings, stainless steel Vici Valco coned tube fittings, and Upchurch polymeric flat bottom fittings. The Vici Valco and Upchurch unions have much reduced volume compared to the Swagelok unions and were thus favored for most of the system. Swagelok manufactures high-pressure three-way valves that were not available from the other two suppliers. Tubing in the system was either PEEK or stainless steel. PEEK tubing was easy to cut using a razor and resulted in consistently good ends. Additionally PEEK tubing was very flexible and was resistant to kinking. PEEK tubing was used wherever possible.

3.7. Temperature Control

The temperature of the reaction zone in the microreactor is controlled during kinetic experiments. In addition, the compression chuck is cooled to quench the reaction and to enable polymeric sealing with the reactor. The polymeric O-rings fail at high temperature. Cooling water flows through the high-pressure chuck, cooling it and the reactor to near ambient temperature. A heating chuck was designed to heat the reactor.

The purpose of the heating chuck is to transfer heat from resistive cartridge heaters to the silicon microreactor while maintaining a uniform temperature profile. The basic design for the heating chuck (Figure 3.10) is to places cartridge heaters in 1/4 inch holes drilled through the aluminum block and suspend the heater from the microreactor. The heating chuck is suspended using light compression in much the same way as the high-pressure chuck is compressed. The reactor is sandwiched between base plate containing the heating element

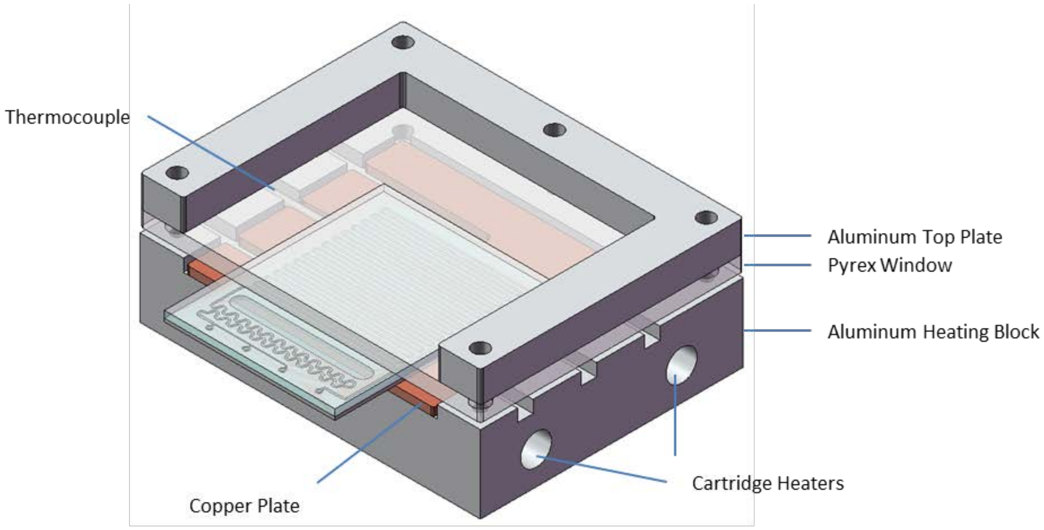

Figure 3.10. Schematic of the heating chuck attached to a reactor.

and a Pyrex window and aluminum top plate. Aluminum was chosen for the heater and top plate because it is inexpensive and easy to machine. The thermal uniformity achieved with aluminum (237 W/m K) alone is likely sufficient, but adding a compliant layer of copper (401 W/m K) should improve the uniformity. Graphite (2.2 W/m K) is an alternative compliant layer because it conforms to the reactor when compressed. Copper was ultimately chosen because of its higher conductivity, its ability to be patterned using a water jet cutter, and the fact that it is sufficiently compliant when a compressive force is applied to it. Precision patterning with an abrasive water jet cutter removed copper from the plate to enable a K-type thermocouple (Omega, KMQSS-062G) to be inserted and contact both the reactor and the aluminum chuck. The thermocouple is cylindrical with a diameter of 1/16 in. A 1/16 in thick copper plate allows the thermocouple to contact the silicon device while preventing the thermocouple from concentrating stress.

To verify the uniformity of the temperature using the chuck design, a two-dimensional COMSOL Multiphysics simulation was run (Figure 3.11). A constant heat flux was applied to the cartridge

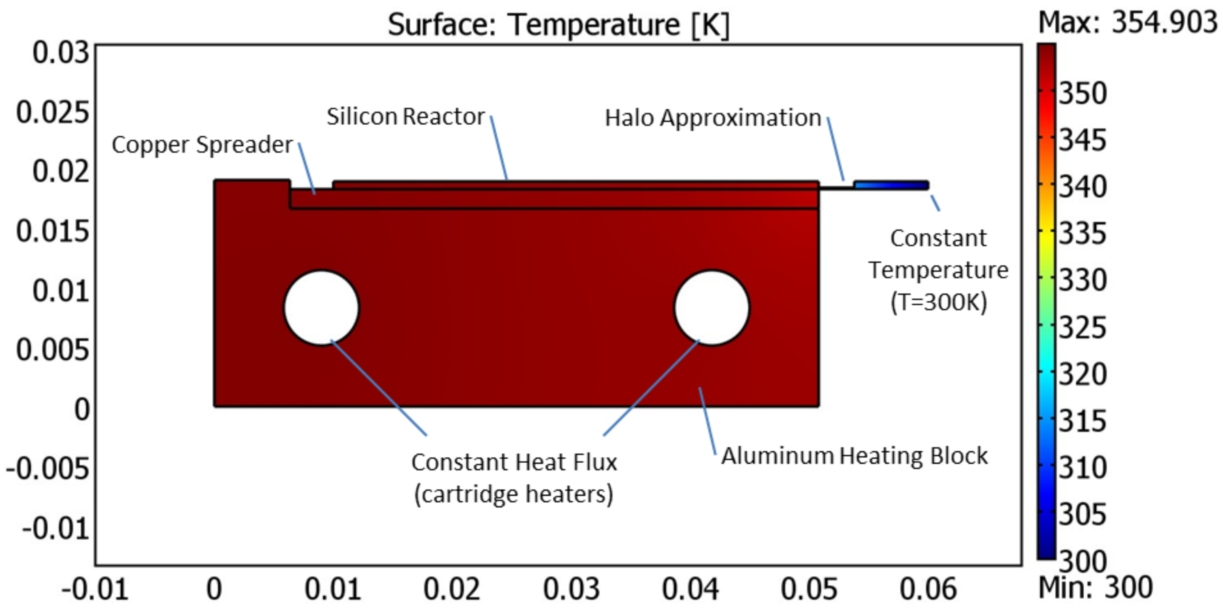

Figure 3.11. Finite elements simulation demonstrates the temperature uniformity across the silicon microreactor in contact with the heating chuck.

heater sections. The heater chuck was drawn as a stack consisting of an aluminum plate, copper heat spreader, and a silicon chip. The right most boundary of the chip was held at a constant temperature of 300 K. A two-dimensional halo approximation was included. The halo etched zone reduces the cross-sectional area available for heat transfer. It was assumed that the halo region removes 80% of the silicon between the heated and cooled region of the chip. Therefore, when approximating the problem in two dimensions, the thickness of the wafer at the halo position is reduced by 80%. The temperature profile along the base of the chip is plotted in Figure 3.12. The temperature profile is largely flat across the heated zone with an average temperature of 353.7 K and a standard deviation of 0.7 K. The maximum temperature deviation is 2.7 K. The design is deemed sufficient due to the low temperature deviations.

The resistive cartridge heaters (Omega, CIR-1021/120V) are capable of providing 125 watts and are 1/4 inch in diameter. These are controlled using a J-Kem Gemini-K temperature controller.

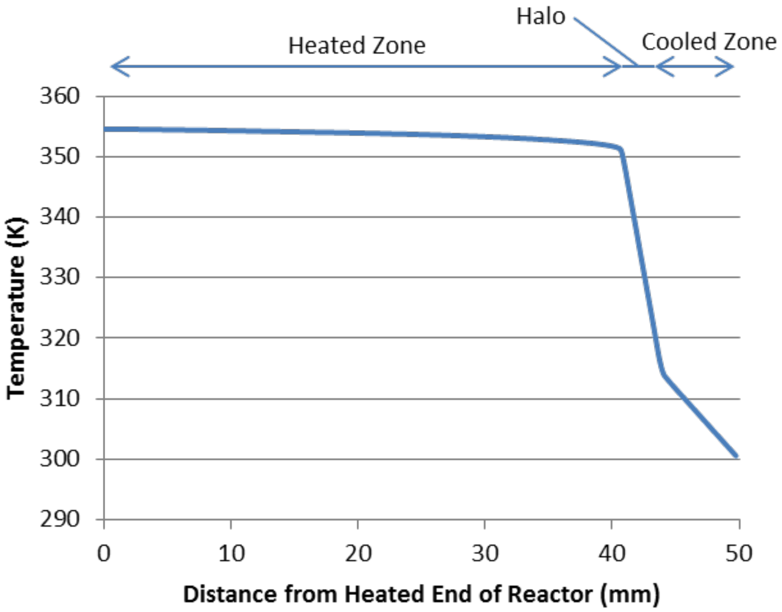

Figure 3.12. Temperature profile along the base of the reactor in Figure 3.11. The temperature in the heated zone averages 353.7 ± 0.7 K with a maximum temperature difference of 2.7 K.

This temperature controller is capable of auto-tuning the PID parameters, which significantly improves the performance of the heating chuck. The reactor temperature is generally controlled within ±0.2 °C of the set-point. Cooling is provided by pumping water through channels in the high-pressure compressor chucks. An inexpensive aquarium pump (ViaAqua 2600 Pump) recirculates room-temperature water from a 14 L reservoir.

3.8. Gas-Liquid Separation

Gas-liquid separation at the micro-scale requires new approaches. Gravitational effects, the basis of traditional separations, are dominated by surface tension effects precluding density-based separations. Microscale separators must therefore harness surface tension effects to separate phases. Phase separation was added to the system to improve sampling reliability in the analytic sections. Two different gas liquid separators were constructed for this system, employing different separation methods.

The degassing separator was built around a Teflon AF membrane. Teflon AF is a gas-permeable membrane with a molecular framework open enough to allow passage of gas. It has been used for degassing solvents under vacuum.[128] This separator was designed to degas the multiphase flow as it passed over the membrane, leaving pressurized liquid on the feed side of the membrane. The separated gas could be depressurized prior to being vented or sent to a mass spectrometer for analysis. The membrane separator was machined out of two blocks of aluminum (Figure 3.13). On one of the blocks, a 1 mm wide spiral design was machined 0.2 mm into the surface and then polished. The other block has a 0.5 inch diameter cylindrical hole where a stainless steel frit was placed. Teflon is capable of operation at high pressure and under high compressive loads, but would rupture if a large force is placed across it. The porous frit supported the membrane preventing rupture. A sheet of Teflon AF was placed covering all

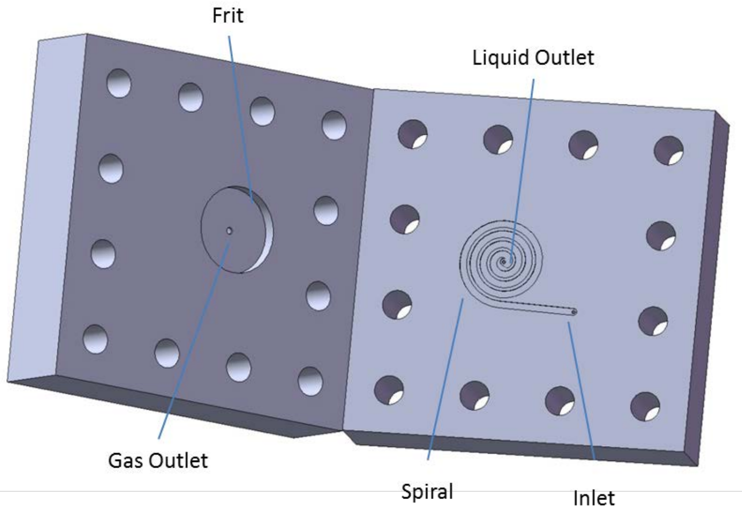

Figure 3.13. CAD model for the degassing gas-liquid separator.

features in the design. Screws were then used to compress the two blocks. The Teflon AF sandwiched between the two blocks was compressed, forming a seal around the channels.

This degassing separator was successfully used at pressures of up to 30 bar. Gas permeated the membrane while liquid did not pass through the membrane. In fact, the gas passed through the membrane so readily that pressure fluctuations were observed in the reactor leading to undesirable bubble coalescence. The main advantage of this technique is that the gas stream is always liquid free. Mass spectrometers, for example, cannot tolerate any liquid contamination.

The second gas liquid separator was adapted from prior work in the Jensen group.[84] For the published application, a Teflon PTFE membrane (average pore size: 0.45 µm) was used to separate two immiscible liquids. Selective wetting and capillary pressure prevented the non-wetting phase from passing through the membrane. Similarly, in a gas-liquid system, the liquid phase would always wet the membrane. Thus liquid can be induced to pass through the membrane while the gas remains on the inlet side (Figure 3.14). This arrangement is the opposite of the degassing separator above. This membrane design requires that the pressures on both sides of the membrane be similar and related in a very specific way. Thus, while the streams are separated, they are later combined and exit the high-pressure system together. Two distinct pressure conditions must be met to ensure separation:

1. The pressure difference between the gas and liquid side of the membrane must be less than the capillary pressure difference, and
2. The pressure drop between the separator and the point where the streams rejoin must be much lower for the liquid side than the gas side.

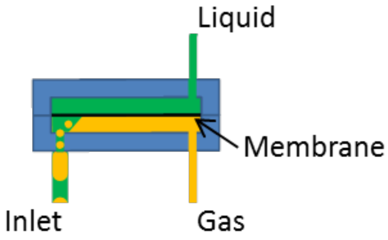

Figure 3.14. Capillary gas-liquid separator. Liquid wets and passes through the membrane while the gas is retained on the inlet side.

The capillary pressure is the minimum pressure required to overcome capillary forces and drive gas through the membrane. The first condition ensures that the membrane is selective for liquid. The second condition ensures that both phases do not just bypass the membrane separator. Given the large viscosity differences between gas and liquid, the second condition requires that the gas side be heavily constricted. Transparent Teflon tubing was attached to both the gas and liquid outlets. The transparent tubing allowed for visually monitoring the separation efficiency. A micro-metering valve was added to each Teflon line to allow tuning of the pressure drops to ensure that the two pressure conditions were satisfied.

The Teflon membrane was again sandwiched between two aluminum blocks of a simpler design (Figure 3.15). A single straight channel (1 mm wide, 0. 5 mm deep, 30 mm long) was machined on the top and bottom blocks. The PTFE membrane was compressed between the two blocks. This design did not require membrane support since both sides of the membrane were pressurized and only differed slightly in pressure. The top block had a single outlet port for the liquid phase, while the bottom block had two ports: an inlet and a gas outlet. The gas-liquid separator performed well under all conditions studied requiring only slight tuning of the micro-metering valves to ensure that the two pressure conditions were met.

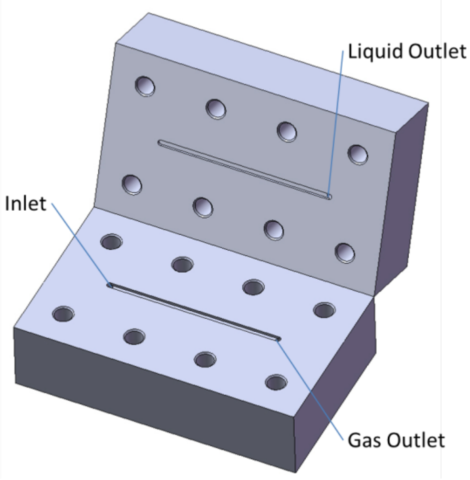

Figure 3.15. CAD model for the capillary gas-liquid membrane separator.

3.9. Offline Sampling

The collection of liquid samples allows for many types of analysis to be performed in the laboratory. Initially, samples were collected from the stream exiting the back pressure regulator, but this quickly proved impractical. The back pressure controller has an internal volume of approximately 2 ml. The system is operated at flow rates on the order of 10 µl/min. Considering only the volume of back pressure controller, it would take over three hours for a sample to reach the outlet. In addition, large chambers, such as in the back pressure controller, must be flushed with a few volumes of sample to reduce sample cross contamination. A new method was required to collect liquid samples prior to the back pressure controller. This method also had to prevent pressure disruptions to the main channel flow to ensure that stable segmented flow was achieved.

The offline sampling unit is constructed out of two high-pressure valves (Figure 3.16). When integrated, the 2-postion, 6-port valves have four states (binary: AA, BA, AB, and BB) which are fully described in Table 3.3. A 100 µl sampling loop is attached to the first valve (Figure 3.17),

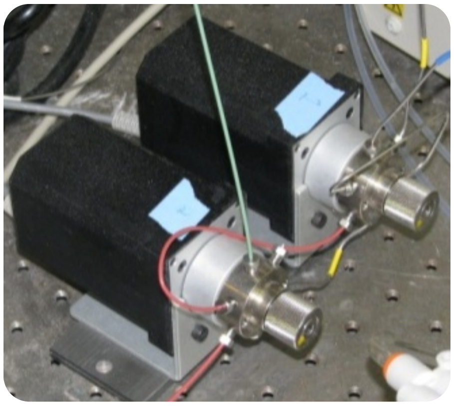

Figure 3.16. Photograph of the two integrated two-position six-port valves.

which allows a sample to be removed from the pressurized system. The second valve is connected to a high-pressure gas line that delivers gas at the system pressure. A nitrogen tank with a regulator manually set to the system pressure is used to supply the high-pressure gas line. After the sample is expelled into a 200 µl insert containing a 2 ml sample, the sampling loop is pressurized using nitrogen. As a result, no pressure disturbances are introduced when the loop is returned to the high-pressure system. The entire filling procedure is automated using a custom LabVIEW program.

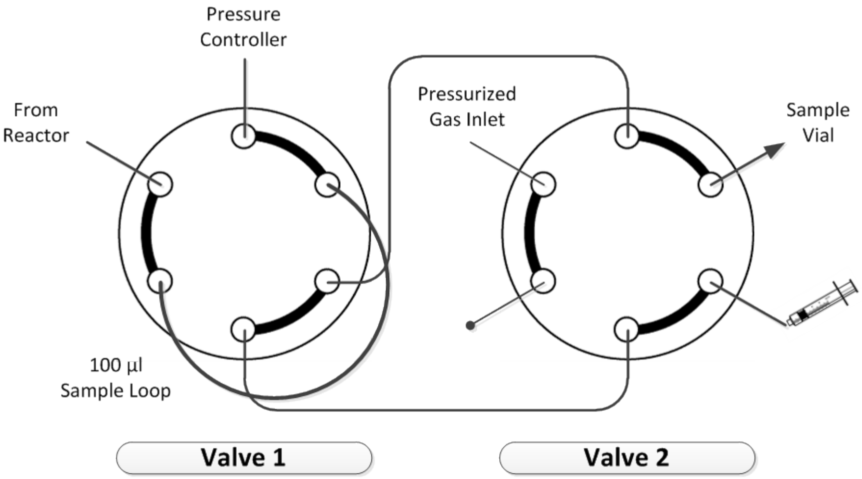

Figure 3.17. Schematic of the two-position six-port valves showing the connections between the two valves.

Step	V_1	V_2	Purpose
1	A	A	Normal operation, flow filling sample loop
2a	B	A	Pressurized sample removed from system
2b	B	A	Sample manually expelled into vial
3	B	B	Pressurize sample loop with gas to system pressure
4	A	B	Reintroduce sample loop into system
5	A	A	Clean sampling line

Table 3.3. Procedure for collecting samples for offline analysis without disturbing system flow using high-pressure valves.

Initially, a 10 µl sample loop was used to collect samples because it was believed that removing and reintroducing a smaller volume to the system would reduce the impact of pressure fluctuations on the flow. When operated with this smaller loop, multiple loop volumes were required to collect the required 70+ µl sample. This system was sampling a combined gas-liquid stream and pressurized gas was used to automatically eject the sample. Ultimately the yield per cycle was very low and large volumes of gas were consumed. This gas led to evaporation and distortion of the collected liquid sample. In addition, aerosolization of the sample was observed.

The addition of a gas-liquid separator overcame these challenges. With the gas-liquid separator in place, depressurization no longer led to the sample being ejected from the system. The sample was thus ejected from the sample loop manually using a disposable syringe which forced air through the sampling lines. The smaller sample loop was replaced with a 100 µl loop so that only a single manual operation would be required to collect an entire sample. Increasing the size of the sample loop did not change the level of disturbance observed in the microreactor during sampling.

The sampling procedure (Table 3.3) was largely automated and controlled through the LabVIEW interface. The loop was filled for a set time, calculated from the liquid flow rate and a user-defined delay. The sample loop was then removed from the system and a disposable syringe was used to eject the sample for collection. The automation was then resumed causing the sample loop to be pressurized and reintroduced into the system. Finally, the sampling line was pulsed three times with nitrogen in an effort to reduce sample cross-contamination.

3.10. Computer Control

The majority of the system was integrated into a single, custom LabVIEW program that enabled remote operation of the high-pressure system. LabVIEW drivers were available for the Teledyne Isco high-pressure syringe pumps and the Agilent data acquisition unit. Customized drivers were developed for the high-pressure valves used in the offline sampling unit, the JKEM temperature controller, and the Bronkhorst back-pressure controller. The LabVIEW interface (Figure 3.18) was designed to include access to all of the major systems including the syringe pumps, pressure controller, sampling valves, temperature controller, and the gas handling system.

The interface enabled all relevant pump parameters to be displayed and modified. Pressure, volume remaining, and flow rate were all displayed in real time. The pressure measured by the back pressure controller was shown in real time, as was the valve output level. The set point could be changed from this interface as well. The operation of the offline sampling unit could be operated automatically or manually. During automation, the progress of the procedure was displayed. The set point and current reading for either channel of the temperature controller

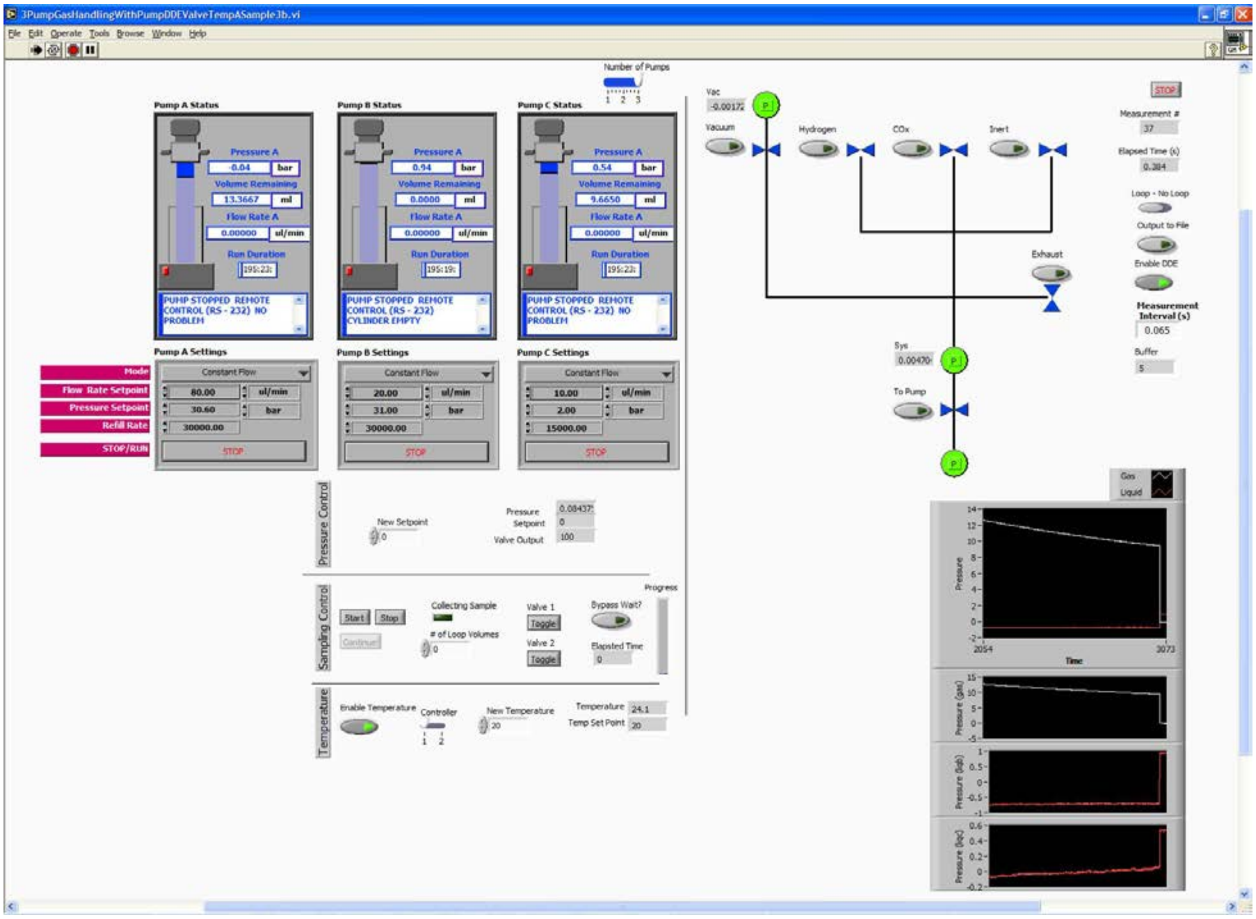

Pump A Status: Pressure A -0.04 bar; Volume Remaining 13.3667 ml; Flow Rate A 0.00000 ul/min; Run Duration 195:23:
PUMP STOPPED REMOTE CONTROL (RS - 232) NO PROBLEM

Pump B Status: Pressure A 0.94 bar; Volume Remaining 0.0000 ml; Flow Rate A 0.00000 ul/min; Run Duration 195:19:
PUMP STOPPED REMOTE CONTROL (RS - 232) CYLINDER EMPTY

Pump C Status: Pressure A 0.54 bar; Volume Remaining 9.6650 ml; Flow Rate A 0.00000 ul/min; Run Duration 195:23:
PUMP STOPPED REMOTE CONTROL (RS - 232) NO PROBLEM

	Pump A Settings	Pump B Settings	Pump C Settings
Mode	Constant Flow	Constant Flow	Constant Flow
Flow Rate Setpoint	80.00 ul/min	20.00 ul/min	10.00 ul/min
Pressure Setpoint	30.60 bar	31.00 bar	2.00 bar
Refill Rate	30000.00	30000.00	15000.00
STOP/RUN	STOP	STOP	STOP

New Setpoint 0
Pressure 0.08437
Setpoint 0
Valve Output 100

Collecting Sample
\# of Loop Volumes 0
Valve 1
Valve 2
Bypass Wait?
Elapsed Time 0

Enable Temperature
Controller 1 2
New Temperature 20
Temperature 24.1
Temp Set Point 20

Vac -0.00172
Sys 0.00470
Measurement # 37
Elapsed Time (s) 0.384
Measurement Interval (s) 0.065
Buffer 5

Figure 3.18. LabVIEW interface for the high-pressure system. This program controlled all pump, gas handling, pressure, sampling, and temperature systems and could be accessed remotely.

were also accessible. Finally, a simplified schematic for the gas handling system allowed each valve to be manipulated. The schematic also displayed the pressure at different locations in the system.

3.11. System Enclosure

Early during the design process, it was determined that the Teledyne Isco high-pressure syringe pumps were the only viable alternative for delivering fluid to the system. These pumps stand 40 inches tall, while the previous enclosure was only 24 inches tall. To be able to place the entire system in an enclosure, a new design was required. The enclosure was built on a 4 ft by 8 ft optical isolation table. This table is shared by two researchers who constructed experimental setups on opposite sides of the table.

Through discussions with MIT's Environment, Health, and Safety (EHS) department, the only criterion for an experimental enclosure is that the average linear face velocity across any open areas is greater than 80 ft/min, with 100 ft/min being preferred. The available ventilation near the enclosure was limited to 1000 ft^3/min. Any remaining ventilation capacity was connected to a gas cylinder cabinet that would hold toxic gases. From these constraints, the maximum exposed area during operation was limited to 100 ft^2. The design must be tall enough to allow the high-pressure syringe pumps to fit inside. In addition, it must enable two people to work simultaneously. The enclosure was designed to be 48 inches tall. Three rows of two doors each were designed for each of the two sides of the enclosure. A one inch gap was left below the bottom doors to allow make-up air to enter the enclosure when all the doors were closed. Two doors open at the same time would expose an area below 100 ft^2. The enclosure was vented through two exhaust ports at the top of the enclosure. Two ports were chosen to reduce the effect of the rectangular enclosure shape.

To verify that operating with different pairs of doors open does not affect local face velocity, a series of simulations were run using ESI CFD-ACE+, a computational fluid dynamics (CFD) and multiphysics solver. This software allows large CFD problems to be solved on relatively modest computer platforms using iterative methods. The geometry of the proposed enclosure was built in the software. The boundary conditions were as follows: exhaust outlet: fixed mass flow rate, open doors: pressure = 0 psig, remaining surfaces: no-slip.

A number of door combinations were tested, including two adjacent and two opposite doors being open. The solution was calculated using the kappa-epsilon turbulence model. A sample solution can be found in Figure 3.19. The simulation shows some variation in the face velocity across the enclosure. The calculated face velocities are above 0.4 m/s which correspond to the 80 ft/min criterion. From this and similar simulations, it was concluded that any two doors could be opened without affecting the safety of the system.

The enclosure was constructed out of aluminum framing with Lexan windows. Lexan is shatter resistant to ensure researcher safety in the event of an explosion within the enclosure. The

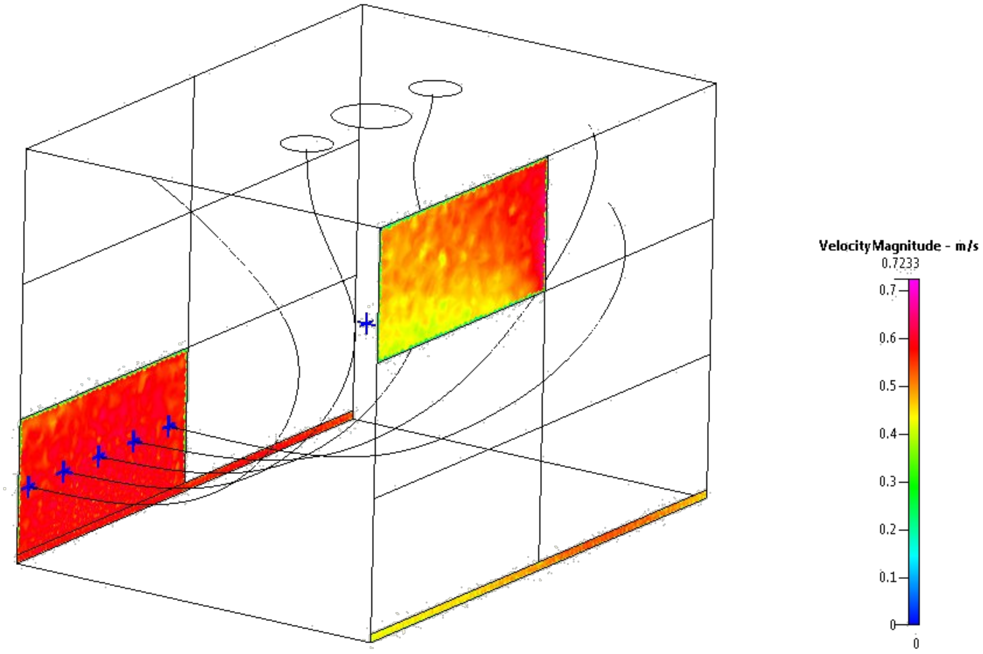

Figure 3.19. Turbulent simulation showing face velocities and particle traces for the case when two doors are open. All velocities are above the required 80 ft/min (0.4 m/s).

aluminum framing was a custom cut product known as T-Slots (Futura Industries). T-shaped nuts and fasteners are inserted in the slots enabling quick assembly. Similarly, door hinges can be attached to fasteners in the slots. The gas handling system, first mounted on an aluminum plate, was suspended from the T-slot material as well.

By designing the enclosure from scratch, it was possible to integrate cable/tube feedthroughs into the design. The feedthroughs are basically custom-designed rings that are fastened to the Lexan panels. Four sheets of neoprene are sandwiched between the ring and the panel. The neoprene has an X pattern cut through it and each sheet is rotated 45° relative to the sheet below it. The neoprene forms a seal around the cables and tubing that is passed into the enclosure. Four feedthroughs were incorporated into the enclosure design requiring that the two large Lexan walls as well as the roof be custom fabricated. The completed enclosure is shown in Figure 3.20.

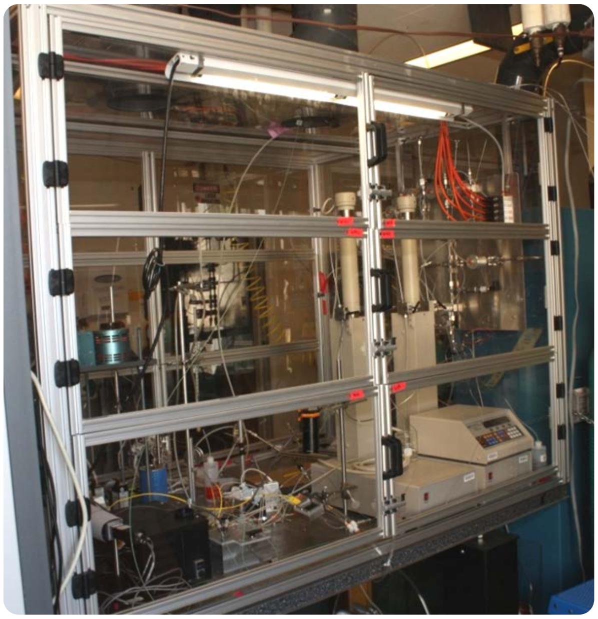

Figure 3.20. Completed system enclosure with six doors per side.

Chapter 4. System Operation and Analytics

Standard operating procedures were developed for the high-pressure microreactor system for both homogeneous and heterogeneous operation. Specifically, a procedure was developed for preparing gas and liquid mixtures, as well as for conducting sequential experiments. For heterogeneous operation, procedures were also required for catalyst loading. Both the inline Fourier Transform Infrared (FTIR) and offline sampling have unique considerations that must be addressed to enable reliable data collection.

4.1. Experimental Preparation

For both homogeneous and heterogeneous reactions, a generalizable procedure was developed. A liquid mixture, required for the day's experiments, was loaded into a high-pressure syringe pump. If a second pump was to be used, a second liquid mixture was loaded into it at this time. A gas mixture was then prepared and loaded into the gas syringe pump. The reactor was loaded with catalyst, if applicable, and connected to the high-pressure system. The back-pressure controller was then set to the pressure for the set of experiments. The gas syringe pump was opened, which pressurized the system. Once the system was pressurized, gas and liquid flow was started. During pressurization, the pump was run at constant pressure to compensate for the gas consumed while pressurizing the system. When the pressures stabilized in each of the syringe pumps, the flow was at steady state and reaction sampling could begin. At the conclusion of the experiments, the system was depressurized through the back-pressure controller; the pumps were depressurized separately. The following sections describe each of these steps in greater detail.

4.1.1. Gas Mixtures

Catalyst systems often require more than one gaseous species for reaction. As described in Section 3.4, a single high-pressure syringe pump is used to deliver the gas to the system. A gas handling system was developed to create a gas mixture in this pump. This gas handling system is automated using a custom LabVIEW program. The LabVIEW program allows the desired composition to be input, as well as the target pressure and volume. The first step in the filling procedure is to evacuate the gas pump and all of the common lines. This is done through the larger diameter line connecting the gas-handling system with the syringe pump. Once the pump has been evacuated for 40 seconds, the manual valve is switched to the smaller diameter line. This line has a larger pressure drop which slows the filling rate.

The first gas is introduced to the system. The program follows the pressure in the gas syringe pump until it approaches the desired pressure. The valve connecting the gas handling system to the pump is then automatically closed. A small reservoir of high-pressure gas is held in the tubing between the closed valve and the low diameter tubing. This gas eventually equalizes in pressure with the pump, increasing the syringe pressure above the desired level. To bleed this excess gas, the back-pressure controller is connected to this zone. A three-way valve is used to connect the back pressure controller to either the high-pressure microreactor system or to the gas handling system. Initially, the back-pressure controller's valve remains closed. Once the valve to the gas handling system is closed, the set point is varied until the pressure stabilizes. At that time, the first gas is considered loaded. The gas handling system is then vented, followed by evacuation. The second and third gas are added sequentially in much the same manner, at increasing pressures so that the partial pressure of each gas corresponds with the desired composition of the final mixture.

When an experiment does not require a mixture, manual controls are used to fill the pump. For example, the only hydrogen gas is required for hydrogenation. In this case, fine pressure control is unimportant because excess gas would just bleed through the system during pressurization. In this scenario, the pressure from the gas cylinder can be used directly to pressurize the system without needing to run the pump. The valve to the gas handling system is then closed before starting the pump.

Upon completion of the experiment, any residual gas in the gas syringe pump is vented through the gas handling system, which is much faster than venting it through the microreactor system. Venting is completed through the larger tube connected to the manual valve.

4.1.2. Liquid Mixtures

The handling of liquid mixtures is largely determined by the sensitivity of each mixture to water and oxygen. Most of the chemistries studied contained compounds that were sensitive to air. Initial manipulations were therefore done under an inert atmosphere in the glove box.

Organometallic homogeneous catalysts are typically solid under standard conditions and are dissolved in solvent. These catalysts are oxygen sensitive and are purchased under an inert atmosphere, which is maintained through manipulation in a glove box. The samples are weighed and transferred to empty septum vials (40 ml, iChem). Stir bars are also loaded into the vial in the glove box. The vial is then sealed and removed from the glove box. To further manipulate the contents of the vial, modified Schlenk line techniques are employed. A nitrogen line connected to a syringe needle is used flush the vial with inert gas, while a second syringe is used as a vent. This vial is thus kept under positive purified nitrogen pressure during manipulations. Anhydrous toluene (used as purchased) is loaded into a syringe and transferred to the vial containing the solid catalyst. The vent is removed, followed by the nitrogen line, leaving the vial under positive pressure. The vial is placed on a stirrer until the catalyst is fully dissolved.

If a liquid reagent is air sensitive and unavailable in an anhydrous form, a different procedure is used. In this case, the reagent is transferred to the glove box for preparation. Molecular sieves, baked at 115 °C for at least 12 hours, are transferred to the solvent bottle. Molecular sieves remove water in the reagent to very low levels. To remove any oxygen-containing species in the reagent, activated alumina is added to the vial. The alumina is activated using the same procedure as described above for molecular sieves. Finally, the reactant is transferred to the vial and sealed. The vial is then removed from the glove box.

The liquid syringe pumps require a special procedure for cleaning. The pumps cannot be disassembled easily, so they are cleaned using repeated fillings. The pumps are first flushed three times with pure solvent, compatible with their previous contents. The syringe pumps, even when “empty,” contain a few milliliters of liquid in the tubing between the syringe and the high-pressure valves. While it is possible to fully exclude air from the first liquid syringe, the second liquid syringe pump does not have this capability and was used for reagents that were not air sensitive. The first syringe pump is first flushed with nitrogen delivered through the gas handling system. This purge expels the remaining liquid in the pump. The purge is run for a few minutes to encourage evaporation of the remaining solvent in the pump. Finally, the pump is evacuated until the vacuum pressure reading stabilizes. This removes all remaining volatile species.

The liquid mixtures in the septum vial are then loaded into the syringe pumps. A nitrogen line with attached needle is reinserted into the septum vial, this time without a vent. A glass, gas-tight syringe is then used to remove the mixture from the vial. The syringe is also fit with an on/off valve. A 0.45 μm filter disk is inserted between the syringe and the needle to filter particles from the liquid. Microfluidic systems are very susceptible to clogging if foreign solids are introduced to the system. The syringe is inserted into the liquid and the valve is opened. Nitrogen pressure drives the fluid into the syringe. When the syringe is full, the valve is closed and the syringe is removed from the vial. The gas-tight syringe is then connected to the syringe pump, which is then filled. In the case of the first high-pressure syringe pump, the line to the attached gas-tight syringe is evacuated before loading. There is no gas headspace in this scenario. For the second high-pressure syringe pump, the lines are initially filled with gas, resulting in gas and liquid being loaded into the pump. The pump is subsequently run until only liquid is observed exiting the inlet, which ensures that all gas is removed.

4.1.3. Solid Catalyst Loading

Catalyst particles must be loaded into the heterogeneous reactors prior to attachment to the system. There are two traditional methods for loading reactors: fluidization and manual manipulation. Fluidization, for example in ethanol, is preferred because loading is faster and requires less researcher manipulation. The typical size of the catalyst particles employed (40-

70 µm) are large enough that they require high velocities to remain suspended. The beds in this study were 1-4 cm long, which would require increasingly large driving forces to maintain the velocity required for particle suspension. Alternately, the particles can be manually manipulated using a spatula to load the dry catalyst particles. A 1 mm micro spatula is used to load each reactor channel individually. The inlet port is filled with catalyst particles. The reactor is then tilted and tapped gently to allow the catalyst particles to flow from the inlet to the bottom of the channel under the force of gravity. The process is repeated many times until the desired bed length has been reached. The length of the bed in each channel is evened by small additions of catalyst. The loaded reactor weight is compared to the empty reactor to determine the catalyst loading.

This procedure leads to uniformly packed beds. High packing efficiency has been observed by simply tapping the reactor to settle the catalyst. When pressurized rapidly, the four bed lengths remain uniform suggesting that there were no voids in the initial packing.

4.1.4. Reactor Packaging

Reactors are loaded into the chuck using a standard procedure. Care must be employed during packaging to prevent cracking the reactor. The homogeneous reactor is inserted into the reactor chuck and aligned by ensuring that the through-etched ports are concentric with the ports on the chuck. The heterogeneous reactor requires an additional step. Given the sensitivity of the microreactor system to clogging, extra effort is made to limit the spread of catalyst particles from the microreactor to the rest of the system. Stainless steel screens (Vici, 1SR1) with 1 µm spacing are placed over the ports on the stainless steel chuck. Care is taken to ensure that the 1/16 inch-wide frits are centered over the ports. The reactor is then slid into the chuck. The chuck is tightened in the same manner for both reactor designs. The four screws on the chuck are tightened a fraction of a turn each following a cross pattern to ensure that the load is evenly distributed. Improper balancing resulted in cracked reactors. During tightening, the spacing between the reactor and the chuck is observed from multiple angles to ensure that equal force is being applied to all four corners. The fluorosilicone O-rings (O-Rings Inc, M25988/1-005) lose their elasticity after a few uses, increasing the likelihood of cracking a reactor during tightening.

4.2. Experimental Operation

After the system has been pressurized, the flow rates of the gas and liquids streams are set. The pressures in the syringe pumps, particularly the gas pump, are monitored until they stabilize. The transient in this step can be large, depending on the pressure drop between the gas pump and the main reactor channel. During operation, the gas pump is pressurizing rather than pumping the gas. The gas is driven across a pressure drop to the reactor. The pressure will vary until equilibrium is reached with the volumetric flow rate. Liquid equilibration happens much more rapidly since it is largely incompressible and therefore can be pumped directly.

If the liquid phase fluid properties, such as viscosity and surface tension, have changed significantly since the previous experiment, the gas-liquid separator would need to be tuned. Under standard operating conditions, both separator outlets are observed through the transparent Teflon tubing connecting the separator to two micrometering valves. The micrometering valves are used to balance the pressure drops such that the only the liquid passes through the porous membrane.

The design of the system makes changing certain variables quicker than others. A change in reactor temperature would only take a few residence times before a new sample could be taken. Similarly, a pressure change would simply require a new steady state to be achieved. Changing the gas composition or liquid composition would require reloading the respective syringe, as described above, and restarting the entire process. If there is only a single liquid reactant, the system is capable of varying the concentration of that species in real time through dilution. A typical experiment would therefore map out a series of temperatures before attempting to change any other parameters. It is essentially very cheap to conduct temperature experiments.

The procedure for each successive temperature is as follows. The temperature is input into the LabVIEW program and the reaction progress is monitored using the inline IR system. The conversion varies with temperature and eventually reaches a steady state. Inline analysis increases experimental throughput. Rather than waiting for a stable temperature followed by a predetermined number of residence times, steady state is observed directly. At this time, samples are collected using the sampling valve system. Two samples are typically collected, of which only the second is retained. The samples are collected in 2 ml screw top glass vials with 200 µl inserts to enable collection of small volume samples. Upon completion of the offline sampling, the next temperature is set and the procedure is repeated.

Following a series of temperature experiments, the next variable is changed. By varying the flow rate, it is possible to determine temporal effects on the reaction. Reducing the system pressure is most useful in experiments with a single species in the gas phase. When the system pressure is changed, it is most efficient to begin the first experiment at the highest pressure. In either scenario, the pressure in the gas syringe pump is monitored until a new steady state is reached. A new series of temperature data is then collected.

4.3. Analytics

The system was designed to have two complementary methods of analysis. The first system incorporates an inline Fourier Transform Infrared (FTIR) spectroscopy system that provides real-time analysis. The second method involves offline analysis. While high-pressure liquid chromatography (HPLC) could also be employed to analyze the offline samples, gas chromatography (GC) with and without mass spectrometry (MS) were used exclusively.

4.3.1. Inline – Fourier Transform Infrared Spectroscopy

A Mettler Toledo ReactIR iC10 FTIR system was incorporated into the high-pressure system. This system is a capable of real-time monitoring of reaction progress. It uses a mercury cadmium telluride (MCT) detector, which is cooled to 80 K to enable a good signal to noise ratio. This system was chosen for the availability of a flow cell. The flow cell (Figure 4.1) allows for continuous monitoring of small volumes of fluid under flow. The flow cell contains an attenuated total reflectance (ATR) sampling element. The infrared beam enters the crystal at an angle such that it is reflected a number of times. At each internal reflection, an evanescent wave is generated that penetrates 0.5-2 µm into the fluid being sampled, depending on the

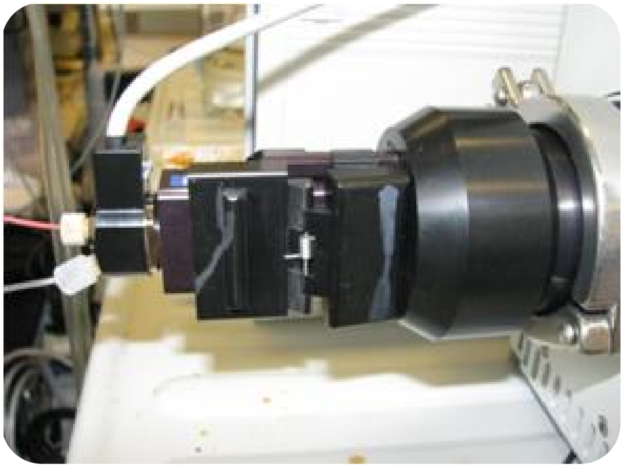

Figure 4.1. Flow cell module connected to the iC10 FTIR. Fluidic connections are made to a removable head, which is heated.

light wavelength. The attenuation from the interaction of the evanescent wave with the sample is passed back the IR beam and analyzed.

The DiComp ATR window is a composite material of diamond deposited over zinc selenide. The diamond coating increases the strength and chemical compatibility of the window, but significantly reduces sampling of the region from 2250 to 1950 cm^{-1}. The combined crystal has a spectral range of 4000 to 650 cm^{-1}, excluding the diamond "blind spot." Alternatively, silicon could be used as the crystal material. It does not suffer from the diamond blind spot, but is not as chemically or mechanically robust as diamond. A silicon window is more likely to scratch during cleaning. Moreover, it is etched by alkaline solutions.

The second half of the flow cell consists of a removable head (shown in Figure 4.2), which is fastened using screws. A Kalrez O-ring provides a fluidic seal between the head and the rest of the cell. The head contains the fluidic connections which are 1/4-28 threaded flat-bottom ports. A variety of fittings are available from suppliers such as Upchurch Scientific that can

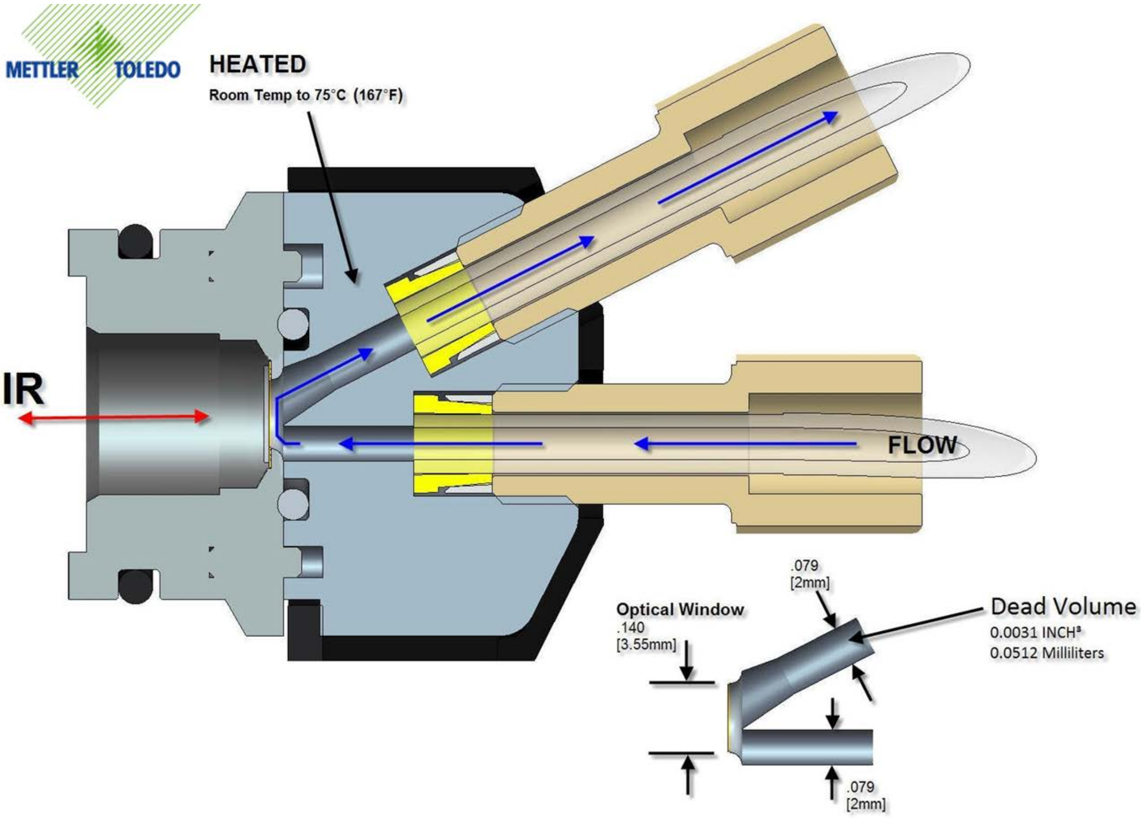

Figure 4.2. Schematic of the flow path in the head of the flow cell. The flow enters on through the lower port, impinges on the window, and exits through the upper port. [Courtesy of Mettler Toledo]

interface with these ports. The flow within the cell impinges on the crystal window before exiting the cell. The internal volume of the flow cell is 51 µl. The removable head also incorporates a resistive heater and an RTD temperature sensor. The flow cell can be maintained at temperatures from room temperature to 75 °C. The flow cell is capable of operation at pressures up to 30 bar. The flow cell restricts the upper operating pressure when the flow cell is used as part of the high-pressure system.

Sampling occurs at predetermined intervals using the accompanying Mettler Toledo reactIR reaction analysis software. Each data point consists of the average of the scans that occur during that interval. For example, with the resolution set to 4 cm^{-1} and the interval set to 30 sec, 127 scans are averaged for each point recorded. The reaction software also performs real-time analysis such as chemometrics, peak integrations, and solvent background subtraction.

4.3.1.1. Operation

When the FTIR was attached to the high-pressure system, additional steps were required at the start of experimentation. Liquid nitrogen is required to cool the MCT detector to 80 K. While the reservoir should be capable of holding enough liquid nitrogen for experiments of up to 24 hr, the liquid nitrogen was topped up before overnight runs. In addition, a dry air purge was required to prevent changes in humidity from affecting the data. The laser beam travels through both fiber and air within the IR instrument. An air background was collected prior to each experiment. During background collection, the spectrum is influenced by whatever is in contact with the ATR crystal. The window must therefore be very clean when the background is collected.

Prior to collecting the background and beginning experimentation, one of two cleaning procedures was employed. The type of experiment most recently run in the system determined which cleaning procedure was used. If the most recent chemistry was the same as the current set of experiments, the goal of the cleaning was simply to remove material from the window itself to ensure collection of a clean background. If a new chemistry was to be run, every effort was made to completely clean the entire flow cell. For a complete cleaning, tubing was attached to the flow cell and a disposable syringe was used to flush it with a series of solvents. Solvents such as water, toluene, acetonitrile, and acetone were used to flush the flow cell. Acetone was always the last solvent. To clean the window, the head of the flow cell was removed. A cotton-tipped applicator, wet with acetone, was rubbed vigorously on the ATR window. The window was then allowed to air dry. The ReactIR software stores a known clean "gold-standard" background spectrum. The software allows a real-time comparison between the measured spectrum and the stored spectrum to verify that the window has been cleaned. Depending on the result of this comparison, the window was further cleaned using a cotton-tipped applicator soaked in the solvents enumerated above. Acetone was always the final rinse because it evaporates rapidly. Once the window was sufficiently clean, a background for the day's experiments was recorded. The head was then reattached to the flow cell. The temperature in the flow cell was set to 35 °C. Temperature control minimizes the effect of room temperature fluctuations on the collected spectrum. IR data collection could then commence.

4.3.1.2. Analytic Approaches

The iC10 spectrometer, together with the micro flow cell, allow for both qualitative and quantitative monitoring of reaction progress. Quantitatively, IR can be unreliable at low concentrations. Small peaks can be overcome by noise in the system, particularly in mixtures of any complexity. Mettler Toledo promises reliable results at concentrations greater than 1% of the total solution. Of course, this depends on the intensity of the IR response to individual species. For example, molecules containing carbonyl groups have strong IR fingerprints and can be tracked quantitatively at lower concentrations than a weaker IR active functional group such as an alkene. Characteristic peak overlap or duplication of functional groups in a mixture increases the difficulty of using IR quantitatively.

Beer's law forms the basis of quantitative analysis based on IR spectra,[129]

$$A(\nu) = a(\nu)bc \tag{4-1}$$

The law relates absorbance at any wavenumber v to the species absorptivity (a) at that wavenumber, the path length (b), and concentration (c). This expression can be extended for mixtures such that Beer's law for a mixture can be written:

$$A(\nu) = \sum_{i=1}^{N} a_i(\nu)bc_i \tag{4-2}$$

where i refers to the ith component of the mixture. The simplest way to apply this relationship is to find a wavenumber where a_i is 0 for all but the desired species. In other words, that peak location is unique to a single species. For example, in a nonanal/1-octene/toluene mixture, there is a peak associated with a carbonyl stretch at 1740 cm^{-1}. Thus by calibrating concentration against this peak, it is possible to calculate the concentration of nonanal. Calibration occurs by taking measurements of known concentrations and fitting a slope to a plot of absorbance against concentration. Essentially the fitted slope is the product of $a(v)b$. Beer's law is expected to be linear over a wide range of absorbance. Deviations can occur when analyzing highly concentrated solutions or when there is insufficient spectral resolution.

For qualitative analysis, it is often desirable to subtract the solvent from the spectrum to ease identification of the desired species. Solvent subtraction can also ease quantitative analysis by isolating spectral bands. Background solvent subtraction works best when the sample mixture is dominated by the solvent, such that the scaling factor k is near unity in the following expression,

$$A = A_r - kA_b \tag{4-3}$$

where A_r is the raw spectra and A_b is the solvent background spectra. As the solvent becomes less dominant, determining the proper scaling factor becomes challenging.

In practice, the height or area of a representative peak can be correlated to concentration. The ratio of the width of the peak versus the instrument's spectral resolution affects the measured stability and accuracy. Very sharp peaks provide fewer possible wave numbers at which the maximum peak height can be observed. Peak area, on the other hand, is less sensitive to spectral resolution since the area lost due to a truncated peak is small relative to the rest of the peak. In practice, both techniques work equally well for the systems studied in this thesis. Absorbance data, after solvent subtraction, is shown for a typical run in Figure 4.3. The data show that there is a strong, highly-linear relationship between peak height and area, as would be expected. Peak height data is easier to collect and was thus the basis for all IR data presented in this thesis.

The analysis presented above is the simplest way of approaching the IR data and only works when a non-overlapping characteristic peak can be identified for each species. The ReactIR software has two additional approaches for performing online data analysis. The first is iC Quant, which uses a training data set to identify spectral characteristics associated with each species. This method enables quantitative results in mixtures with many overlapping peaks. The second method, ConcIRT applies chemometrics to identify patterns in the IR data over time

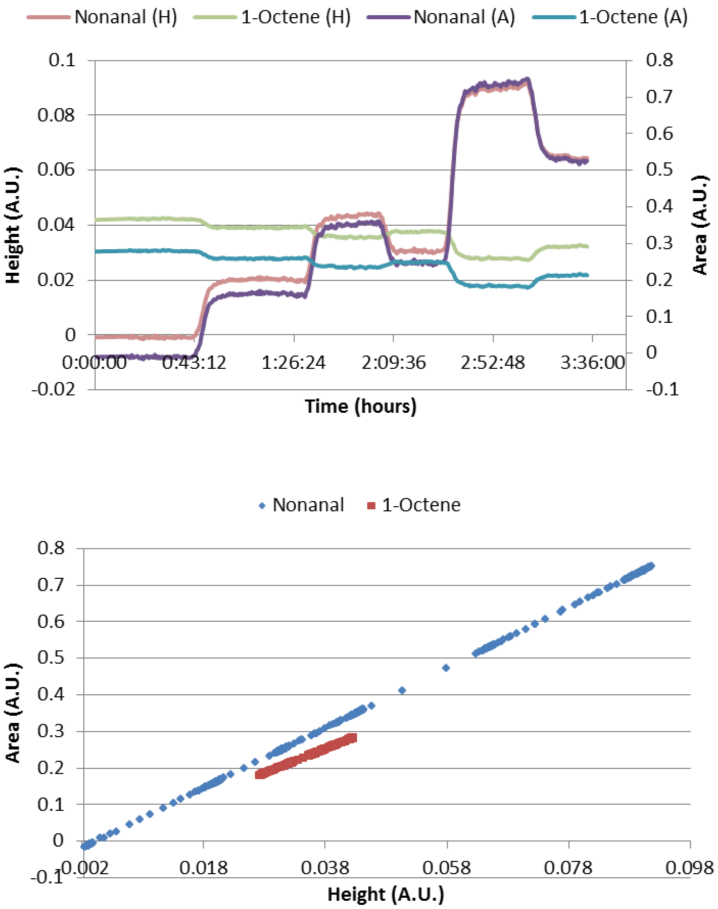

Figure 4.3. Top: Raw reaction data as temperature is varied showing both height and area data associated with nonanal and 1-octene. Bottom: The same data is plotted showing that a linear relationship exists between height and area. (A.U. abbreviates arbitrary unit)

and is able to identify different species in the sample and provide a rough spectrum for each species.

Before running an experiment using the iC Quant system, a model must be developed within the software. A known series of samples are prepared and sampled using the IR system. The resulting spectra and concentration data, collectively known as a training set, are then fed into the model software. The model is based on the spectra within a defined range that would preferably exclude strong solvent peaks. A partial least squares method is used to reduce a sample spectrum into a handful of variables that are indicative of the larger spectrum. A model is then defined by further reduction of these variables down to a set of principle components. Ultimately, fewer principle components must be selected than there are data points in the training set to ensure a reasonable model.

An iC Quant model was prepared for the hydroformylation reaction of 1-octene to nonanal. Two component mixtures were prepared of 1-octene and nonanal in toluene (solvent) at concentrations ranging from 0.01 to 0.50 M, with a combined analyte concentration of 0.50 M. A model was developed that fit the data and could then be applied in real time as IR data was collected. The predicted concentrations for a sample run are shown in Figure 4.4. While the predicted concentrations follow the expected trends as the temperature is varied, they fail to make physical sense. The model forces mass balance closure, while allowing the concentration

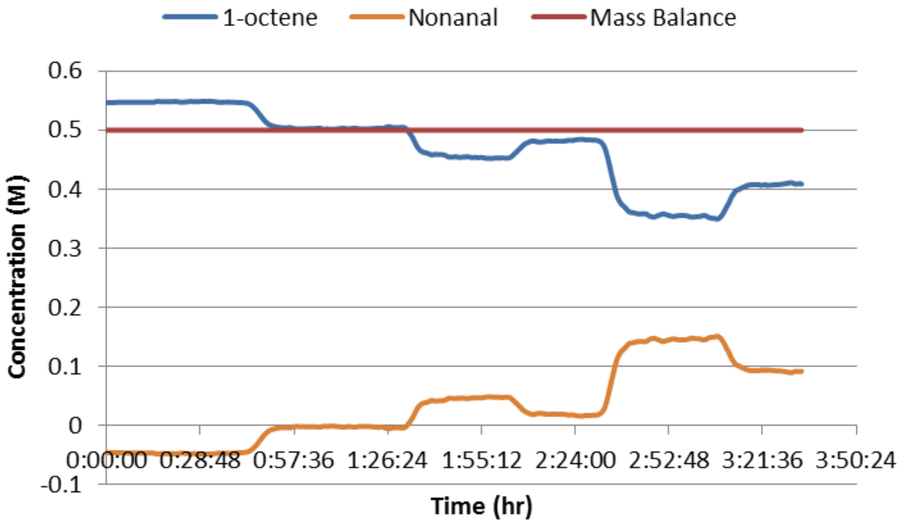

Figure 4.4. The iC Quant concentration results from an experimental run, as temperature is varied. While the mass balance closure is perfect, the model makes little physical sense due to the negative concentration of the nonanal product.

of nonanal to be negative. Training the model with single component mixtures led to poor mass balance closures. While it is conceivable that a training set could be devised that would lead to a better model, no further effort was expended because manual single peak analysis led to reasonable results.

ConcIRT analysis was also applied to the hydroformylation system. The benefit of ConcIRT is that the chemometric methods require neither a training set nor any a priori knowledge of the system. By tracking a portion of the spectra with time, it attempts to decompose the raw data into pure component spectra. From these spectra it generates concentration profiles with arbitrary units that can be used to study complex reactions. This analysis was attempted as a third possible method for analyzing the IR reaction data.

The concentration profiles calculated using the ConcIRT method (Figure 4.5) follow the same trends as simply monitoring the characteristic peaks for nonanal and 1-octene. Component

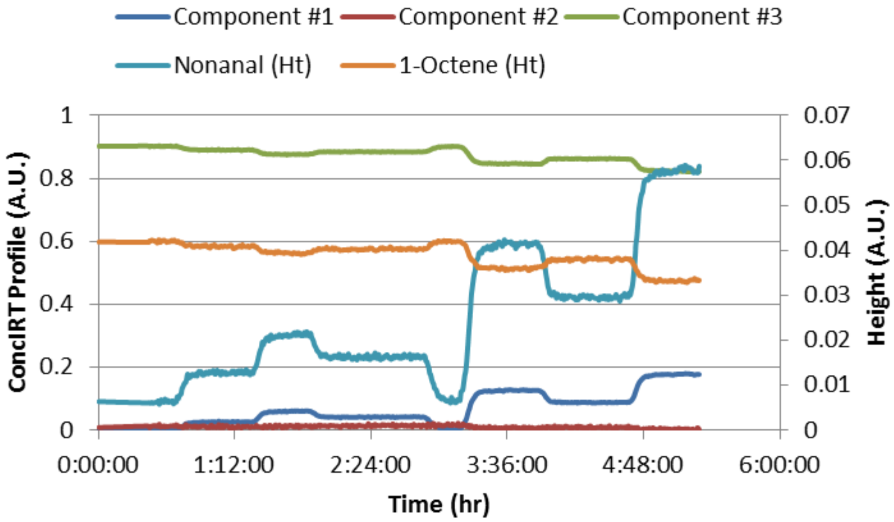

Figure 4.5. ConcIRT concentration profiles are compared to the peak-height based profile completed manually (Ht).

#3 is 1-octene and Component #1 is nonanal. The analysis also identified a third component (Component #2) that does not vary widely over the course of the experiments.

In addition to the concentration profiles, the method also determines estimates of the pure component spectra. These spectra are shown in Figure 4.6, along with analytically pure component spectra. The heights of the peaks in this comparison are arbitrary, but the location of the peak is important. The peak that ConcIRT identifies as Component #1 has the characteristic peak of nonanal at 1740 cm^{-1}. Similarly, Component #3 shares its characteristic peak with 1-octene at 1642 cm^{-1}, as well as most of the toluene spectrum. Component #2 appears to be positively correlated with 1-octene and negatively correlated with nonanal. This proposed spectrum makes little physical sense and is of little importance in the

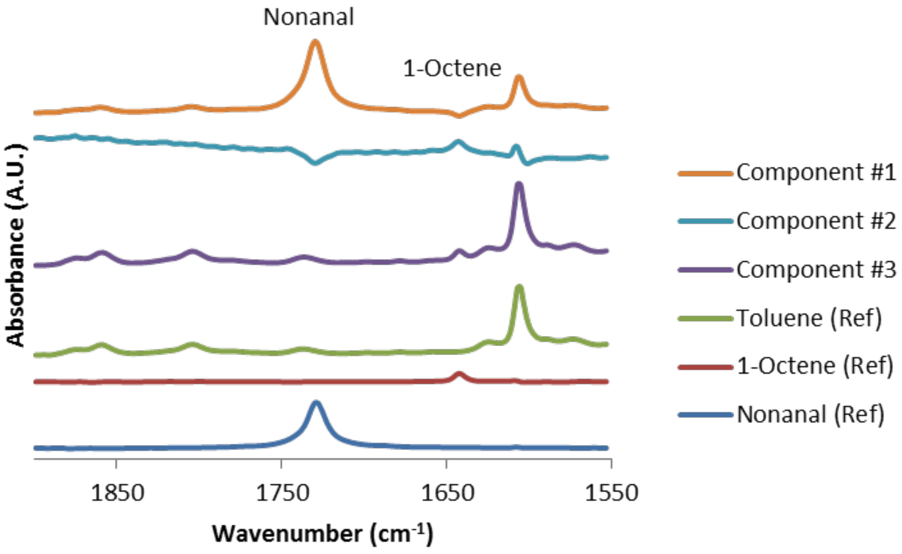

Figure 4.6. A comparison of the ConcIRT pure component spectra against the directly measured pure component spectra shows that Component #1 is correlated with nonanal and Component #3 is correlated with 1-Octene. Component #2 appears to be positively correlated with 1-octene and negatively correlated with nonanal.

concentration profiles in Figure 4.5. It is interesting to note that both Components #1 and #3 contain peaks associated with the toluene solvent. Introducing solvent peaks into the spectra for the reacting components is expected to reduce the accuracy of the overall model. In addition, a calibration would still be required to use this analysis quantitatively. For the systems studied in this thesis, it was simpler to perform a manual analysis based on the height of a single characteristic peak for each species.

4.3.1.3. Gas-Liquid Effects

When first introduced into the system, the flow cell was inserted directly downstream of the reactor. This arrangement analyzed the multiphase flow directly. During multiphase flow, the liquid phase is expected to wet all walls, including the ATR crystal. The evanescent wave is only expected to penetrate 0.5 to 2 µm into the flow, permitting sampling of the liquid phase. In general, a strong signal was observed when sampling multiphase flow. However, the data was noisy and would unexpectedly dip at times (Figure 4.7). Data for both 1-octene and nonanal vary in the same direction suggesting variation of the wetting layer thickness. If the variability was caused by fluctuating conversion, 1-octene and nonanal would have oscillations that were out of phase.

A gas-liquid membrane separator was inserted between the reactor and the flow cell. Thus only liquid was sent to the flow cell, removing multiphase complications. The resulting peak height data had less variability (Figure 4.8) suggesting that the presence of a second phase affected data collection.

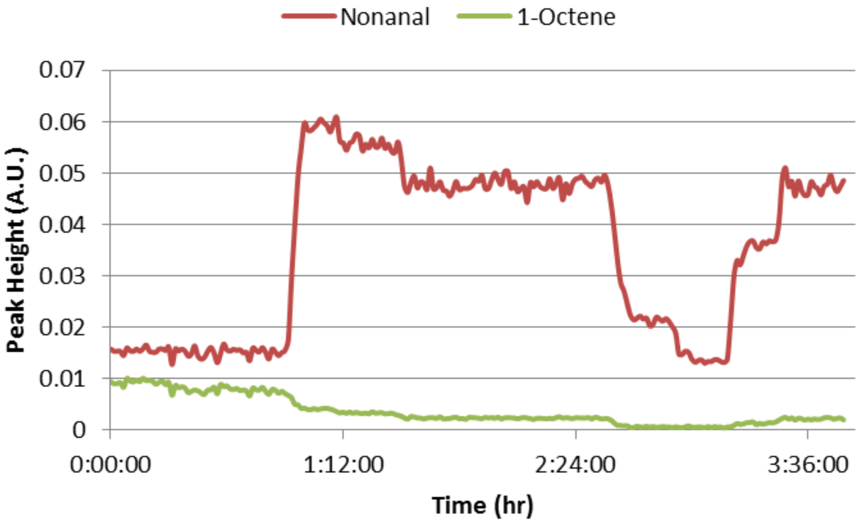

Figure 4.7. Raw IR data for a multiphase samples is noisy. The peaks and valleys are correlated between 1-octene and nonanal suggesting the magnitude of the entire spectra is varying.

A more direct way to analyze the effect of multiphase flow was to vary the flow rate, while maintaining a gas to liquid ratio of 3:2. The concentration of 1-octene in the liquid phase was

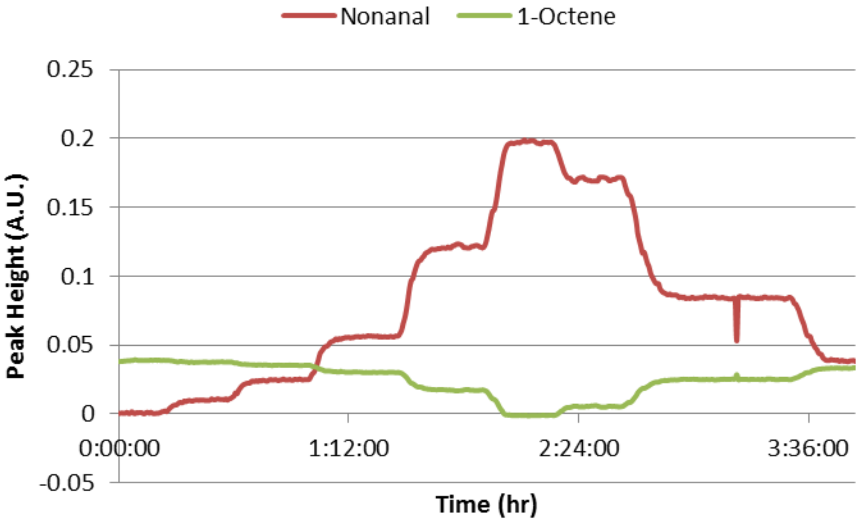

Figure 4.8. Raw IR data for a liquid stream only. The variability in peak height is greatly reduced when compared to the multiphase data in Figure 4.7.

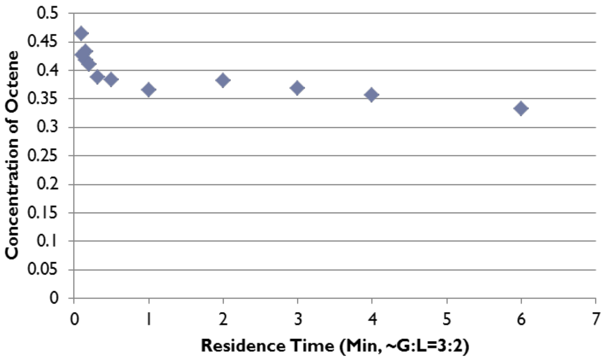

Figure 4.9. The measured concentration of 1-octene varied during multiphase flow. The concentration of all samples was 0.54 M, as measured in single phase flow.

constant for the entire experiment. However, the measured concentration of 1-octene decreased as the flow rate increased (Figure 4.9). This trend is consistent with the liquid film thickness on the surface of the ATR crystal decreasing at faster flow rates. As the liquid film thins at higher flow rates, the measured amount of attenuation decreases, reducing the peak height associated with 1-octene. When the same liquid stream is injected directly into the flow cell, in the absence of gas, a concentration of 0.54 M was measured. These results further highlight the susceptibility of the IR flow cell to multiphase flow. All remaining IR data in this thesis were completed after the addition of the gas-liquid membrane separator ensuring that only liquid is measured.

4.3.2. Offline – Gas Chromatography and Sample Collection

Gas chromatography (GC) provides an alternative analysis method to IR. GC is a common laboratory technique for analyzing compounds that can be vaporized without decomposition. Typically, the analytes must have boiling points above room temperature and below 300 °C. Large, high-boiling molecules can remain in the sampling zone or column, contaminating future results. Similarly, salts or other solid materials remain in the system, eventually leading to clogging. GC analysis can also differentiate isomers, which is impossible using IR. GC is able to quantitatively analyze more complex mixtures than IR is capable of. In addition, GC can analyze molecules without any IR active groups. Offline GC analysis has an inherent delay, preventing it from being the sole analysis technique. When used in concert, IR and GC provide analytical redundancy.

An Agilent HP 6890 series gas chromatograph, with a HP-5MS column, was used to analyze the offline samples. In conjunction with a heat ramp, the column separates different species based on their interaction with the column surfaces. Using a robotic autosampler, liquid samples are injected into a sample zone and vaporized. An inert gas, typically helium, is used as a carrier. Absorption on the surface inhibits analyte progress in the column. The inhibition varies by molecule, allowing separation to occur. A flame ionization detector is used to monitor the outlet of the column. The area under each peak is proportional to the analyte concentration. Under ideal conditions, each species in the mixture elutes at a different retention time, allowing for analysis of complex mixtures. The characteristic retention time is a function of analyte, column, and method employed. Calibration standards are run to determine a species retention time and relative response factor.

When the identity of a species is unknown, the GC column can be used in conjunction with a mass spectrometer (MS). GC-MS analysis is only required to characterize unknown peaks identified during simpler GC analysis. For most samples, GC analysis is sufficient to determine concentration. The mass spectrometry data consists of a spectrum that shows the relative abundance of molecules of different weights. The spectrum is composed of basic peaks and fragmented peaks. Basic peaks are those associated with the total mass of a molecule or after a single deprotonation. Fragmented peaks occur when bonds are cleaved during ionization. Different fragmentation patterns allow isomers to be distinguished. Mass spectra are typically compared to a spectral library to identify the molecule.

4.3.2.1. *Sample Crossover during Collection*

Early samples collected for GC analysis were unreliable. The hydroformylation of 1-octene to nonanal was run at different temperatures, which were varied in a random order. The reaction rate was expected to increase exponentially as temperature is increased. Early results showed great scatter in the results, as though the results were affected by previous samples. To test this hypothesis, two samples were successively collected at each temperature point (Figure 4.10). In the figure, the red crosses are the first sample, and the blue squares are the second sample and are numbered according to experimental order. When the previous experiment was at higher conversion than the current experiment (labeled “d”), the conversion was higher for the first sample. When the previous experiment was at lower conversion (labeled “u”), the conversion was lower for the first sample. For the first data point, both the first and second samples have the same conversion. When only the second samples are considered, the expected exponential relationship is present. This suggests that there is crosstalk between samples. The problem persisted even after reducing the number of connections in the sampling line. The ultimate solution was to take two samples at each condition and discard the first. All remaining GC data in this thesis employed this strategy.

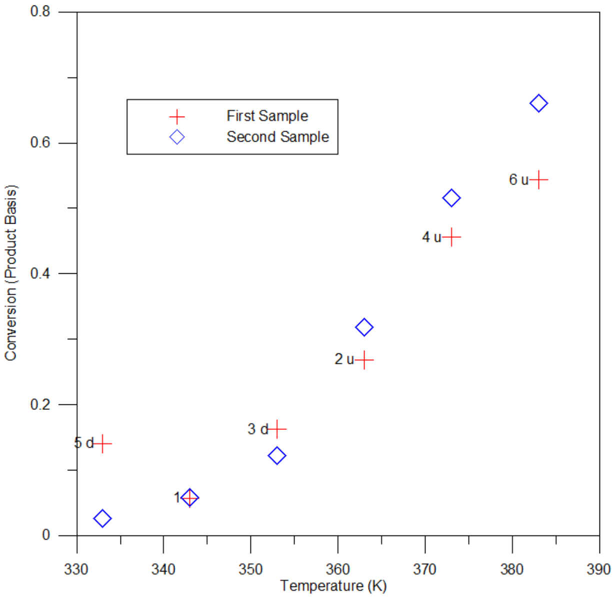

Figure 4.10. Crossover contamination was observed during offline sampling. When two successive samples were analyzed, the first sample was influenced by the previous reaction condition. This was not the case for the second sample. Numbers represent sample order, "d" represents a lower temperature than the previous sample, and "u" represents a higher temperature than the previous sample.

Chapter 5. Homogeneous Catalysis – Hydroformylation

5.1. Introduction and Reaction Literature

Homogeneously catalyzed gas-liquid reactions, such as the hydroformylation of alkenes to aldehydes and the carbonylation of methanol to acetic acid, are of high industrial importance. While catalyst recycling proves to be an expensive challenge, homogeneous catalysis displays a number of benefits when compared to heterogeneous catalysis. Homogeneous catalysts typically have higher activity and selectivity, require milder reaction conditions, and provide the ability for some mechanistic understanding.[130]

Rhodium catalyzed hydroformylation was discovered by Wilkinson and his colleagues in the late 1960s.[131] This new catalyst system could be operated at more moderate conditions relative to its predecessor, cobalt carbonyl.[132] Hydroformylation reactions are expressed as follows:

$$\mathrm{RCHCH_2 + H_2\,CO \rightarrow RCH(CHO)CH_3}\ \textit{or}\ \mathrm{R(CH_2)_2(CHO)} \qquad \textbf{(5-1)}$$

One of the most commonly studied catalysts is $HRhCO(PPh_3)_3$ which was first identified by Wilkinson.[131] The mechanism is currently thought to be well understood, and can be found in Figure 5.1. This mechanism consists of two branches which determine the selectivity of the reaction to the linear or branched aldehyde product. Selectivity towards one product is determined by whether the center metal forms a bond to the terminal or internal carbon (Steps 3 and 9). Selectivities, which can often exceed 90% for the linear product, are a function of the type of ligand that is attached to the rhodium center.[132] After alkene insertion (Step 2), carbon monoxide is added (Step 6), followed finally by hydrogenolysis (Step 4). A number of internal rearrangements occur during the reaction and are typically unobservable during kinetic studies.

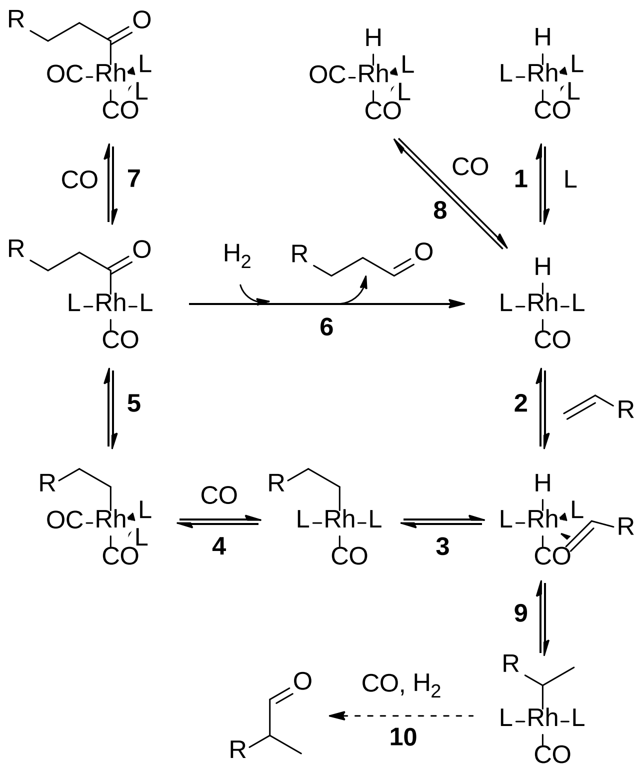

Figure 5.1. Widely accepted mechanism for alkene hydroformylation. Steps 2-6 are the dominant cycle and result in the linear aldehyde product. Steps 9-10 represent a similar cycle whose product is the branched aldehyde.

The rates of the equilibrium reactions are important because a number of reactions also remove rhodium from the catalyst cycle through the coordination of an additional carbon monoxide molecule with the metal center. These equilibria depend on the concentration of the available ligands. For example, triphenyl phosphine (L) and carbon monoxide can coordinate to the rhodium in different ratios,[132]

$$HRhL_4 \leftrightarrow HRh(CO)L_3 \leftrightarrow HRh(CO)_2L_2 \leftrightarrow HRh(CO)_3L \leftrightarrow HRh(CO)_4 \qquad \textbf{(5-2)}$$

Studies have shown that the disassociation of CO is 100 times faster than the hydroformylation reaction at 85 °C.[100] FTIR in situ studies have shown that at low phosphine concentrations, $HRh(CO)_2(PPh_3)_2$ is the predominant precursor species and readily reacts with the alkene.[133]

Despite the wide agreement on the mechanism of rhodium catalyzed hydroformylation, the identity of the rate determining step is a source of continued debate. Different groups identify either the coordination insertion of alkene or the hydrogenolysis to the product as the rate determining step and thus disagree whether hydrogen pressure should affect reaction rate. An early study into the kinetics of propene hydroformylation expressed a rate law that was zero-order in hydrogen.[134] Later studies of slightly different systems found either positive-[135-138] or zero-[139] order dependence on hydrogen. Van Leeuwen directly addresses this discrepancy and argues that differences in conditions, most notably hydrogen pressure, could lead to a positive observed order due to the requirement that hydrogen cleave di-rhodium species before they can renter the catalytic cycle.[132, 140, 141]

The choice of ligand also affects the rate determining step. DFT calculations[142] and FTIR in situ studies[143] have demonstrated that the electrophilicity of the ligand determines whether the insertion of alkene or hydrogenolysis is the rate determining step. Phosphite ligands also lead to higher reaction rates than phosphines.[144-146] For electron withdrawing ligands such as phosphites, the rate determining step is found to be alkene insertion. For electron donating ligands such as phosphine, the rate determining step is hydrogenolysis. Another DFT study finds that CO insertion is rate determining.[147]

A number of kinetic studies for $HRhCO(PPh_3)_3$ catalyzed hydroformylation are available in literature. These studies express the kinetics as either an overall power law[99, 134] or an empirical form chosen through regression analysis.[135-137] Both types of expressions provide a reasonable fit for the data and the many different forms reflect the complexity of the system.

As can be expected for empirically-derived kinetic expressions, they are only valid within the range of experimental conditions. The complexity of the mechanism prevents a comprehensive kinetic model. There are multiple catalyst complexes, such as rhodium-hydride or rhodium-acyl, which remove rhodium molecules from the catalyst cycle.[143] The choice of alkene, hydrogen and carbon monoxide partial pressures, ligand concentration,[140] and solvent[148] all affect the observed kinetics.

Murzin et al.[149] recently attempted a kinetic model to explain the regioselectivity of alkene hydroformylation. They claim that the relative selectivity of the products depends on the ratio of CO to PPh_3 ligand on the rhodium center during reaction. When the catalysts exists in the active form $HRhCO(PPh_3)_2$, shown before Step 2 of Figure 5.1, the selectivity to the linear aldehyde is higher than when the active form is $HRh(CO)_2(PPh_3)$. These observations are consistent with experimental data showing that an excess of PPh_3 ligand, which would favor the catalyst form with increased ligand, increases the selectivity towards the linear product.[140] Murzin developed a microkinetic model using elementary reactions from the four reaction cycles (two catalysts each forming two products). They formed an overall rate expression after applying a quasi-equilibrium assumption. These expressions were greatly simplified using results from an earlier study, such as the overall order of the kinetic expression in CO and alkene.[99] Much of the simplification, which made further analysis possible, was based on the first order dependence on CO in their data. Other groups found CO pressure have a negative overall order, which would prevent this simplification.[135-137]

5.2. Experimental

Catalyst and reactant solutions were prepared individually and loaded into the two liquid syringe pumps. The catalyst, tris(triphenylphosphine)rhodium(I) carbonyl hydride ($HRhCO(PPh_3)_3$) (Aldrich, 225665), and extra ligand, triphenyl phosphine (Sigma-Aldrich, T84409) were dissolved in anhydrous toluene (Sigma-Aldrich, 244511). A 2:1 mass ratio of ligand to catalyst was used for all experiments. The solution was prepared using a glove box, under a nitrogen atmosphere, and modified Schlenk techniques to exclude oxygen (Section 4.1.2). The reactant, 1-octene (Aldrich, O4806) was separately diluted in toluene. Hydrogen (Airgas, HY Z300), carbon monoxide (Airgas, CM UHP35), and nitrogen (Airgas, NI UHP300) gases were all used as purchased. The three gases were added sequentially to the gas syringe pump to achieve the desired composition and pressure (Section 4.1.1).

The standard conditions for the reactions were: hydrogen pressure = carbon monoxide pressure = 11.25 bar, nitrogen pressure = 2.5 bar, catalyst concentration = 5.0×10^{-4} M, and 1-octene concentration = 0.50 M. Nitrogen was included to ensure that bubbles would remain and reduce axial dispersion if all of the reacting gas was consumed. The reaction was carried out in flow, with a liquid flow rate of 26 μl/min and a gas flow rate of 29 μl/min. These flow rates correspond to a residence time of 4 min in the heated zone of the reactor. To explore the parameter space, only a single condition was varied from these standard conditions. The active form of the catalyst was created in the reactor during reaction. For each set of conditions, the temperature was varied randomly between 85-105°C, in 5°C increments. The reaction rate was estimated from the concentration of the aldehyde products. When experiments were repeated in during a single run, the reproducibility was very high. The results varied by less than 1%.

5.2.1. Analytic Considerations

Mass balance closure is an important analytic system benchmark. A closed mass balance signals a well calibrated analytic system that accounts for all participating species. A sample experimental run is presented in Figure 5.2. Two analytic techniques are shown, as well as the sum of all of the species analyzed by GC. The mass balance should remain constant at all temperatures. The calculated mass balance closure for the gas chromatography data has a standard deviation of 1%. The mass balance using the IR measurements show the mass balance varies as temperature increases.

The measurement of 1-octene and nonanal using the two techniques tends to follow the same trend, but are slightly offset. For example, the deviation increases at higher concentrations of

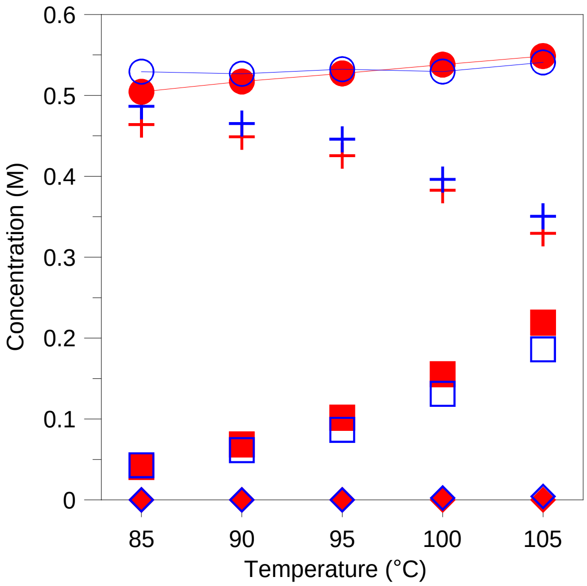

Figure 5.2. Raw data for 1-octene hydroformylation at standard conditions. The three measured species are 1-octene (+), aldehydes (■), and 2-octene (◆) measured by FTIR (red filled) and GC (blue open). The circles are the sum of the measurements of all of the GC data and demonstrate good mass balance.

nonanal. These deviations cause the observed trend in the mass balance calculations and endured through multiple calibrations. Calibration was completed in both single component and multicomponent solutions. The initial calibrations were prepared in volumetric flasks by diluting each species individually. A predetermined volume of each species was pipetted into the flask and then diluted in toluene (solvent). By avoiding serial dilution methods, an error in the preparation of the initial stock solutions would not propagate to the other standard mixtures. On the other hand, nonlinearities in the calibration of the micropipette would still propagate as the solutions were prepared.

Calibration curves were prepared for three species, 1-octene, nonanal, and 2-octene (a potential side product) and are shown in Figure 5.3. All calibrations exhibit high correlation coefficients and near zero intercepts. Given the IR mass balance closure described above, a second and independent nonanal calibration was prepared. Both nonanal calibrations have

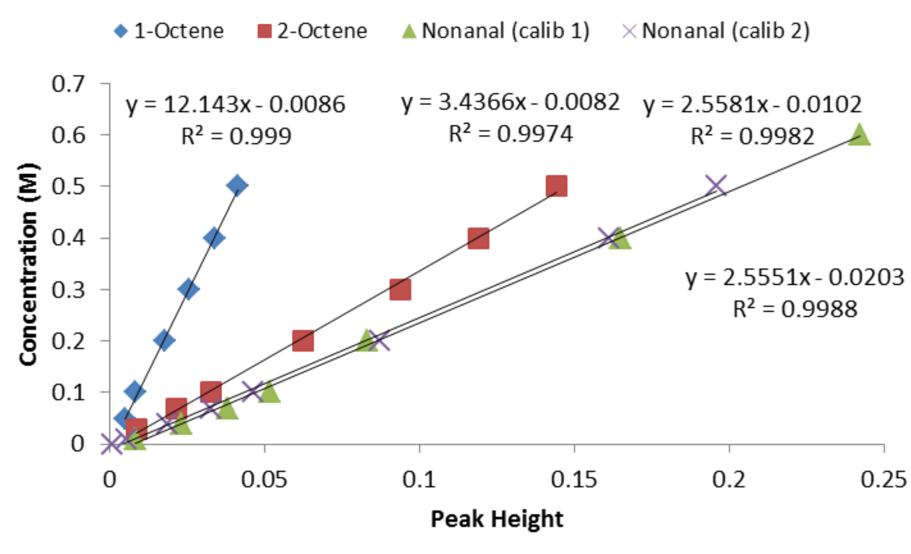

Figure 5.3. Prepared calibrations for 1-octene, 2-octene, and nonanal. All calibrations have near zero intercepts and high correlation coefficients.

nearly identical slopes suggesting that errors in preparing the standard solutions are unlikely to cause mass balance issues.

There is no overlap between the characteristic 1-octene and nonanal peaks. Figure 5.4 shows the variation in peaks of these spectra, after solvent subtraction, as 1-octene is converted into nonanal. At higher concentrations, the solvent subtraction algorithms of the iC IR software could potentially be less quantitatively reliable. To test this hypothesis, a second set of calibration standards were prepared. For these calibrations, the total concentration was held fixed at 0.5 M. Mixtures were prepared by combining different volumes of 0.5M solutions of 1-octene and nonanal. These mixtures were then analyzed to develop a calibration. The

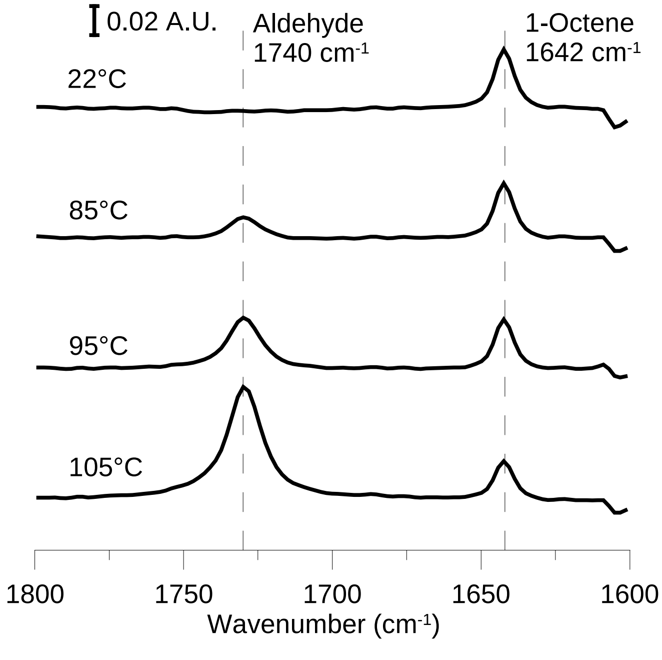

Figure 5.4. IR spectra of the hydroformylation reaction at standard conditions, after solvent subtraction. The 1-octene (0.5 M) is consumed more rapidly at higher temperature to evolve the aldehyde products. The peak at 1642 cm^{-1} corresponds to the C=C stretch of a vinyl group, while 1740 cm^{-1} corresponds to C-O stretch of an aldehyde.

calibration was not materially different from Figure 5.3. Catalyst was also added to the calibration solutions to test if the carbonyl ligand affected the aldehyde response. The catalyst containing solutions were indistinguishable from the original calibrations.

Another possible error source is that only one of the aldehyde products was commercially available. Specifically, calibrations were only constructed from nonanal solutions, when the product of the hydroformylation is a mixture of nonanal and 2-methyl-octanal. The IR response to the carbonyl is not expected to vary greatly. In addition, GC analysis of the product streams shows that the ratio of branched to linear product remains consistently 1:3. The spectra of 0.5 M hexanal and 2-methylpentanal in toluene were analyzed as a proxy aldehyde pair. From the analysis (Figure 5.5), the peak height of 2-methyl pentanal was 3.5% larger than hexanal. For a difference in height of the carbonyl peak in the branched and linear products to account for the deviations in the mass balance, the response of the branched peak height would have to

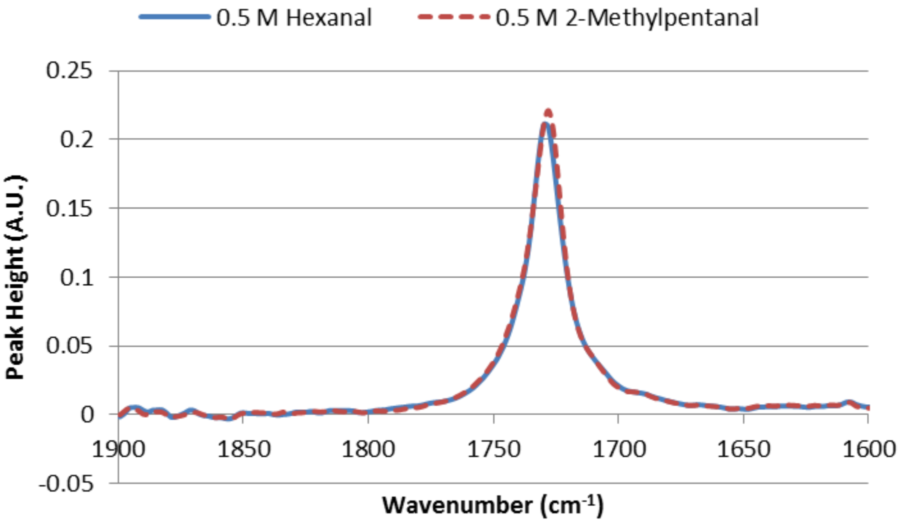

Figure 5.5. The spectra for 0.5 hexanal and 2-methylpentanal are nearly identical, with 2-methylpentanal having a 3.5% stronger response.

be 50% larger. This increase is not observed for the proxy aldehyde pair.

Gas chromatography analysis consistently provided good mass balance closure. It was able to separate all species, including the product isomers, while avoiding solvent complication. As a result, all remaining data presented in this chapter were based on the gas chromatography data. IR data was always collected in concert to monitor the stability of the reaction and identify problems during operation.

5.3. Kinetic Results of Hydroformylation

The high-pressure system was used to conduct a series of experiments where the partial pressures of carbon monoxide and hydrogen and the rhodium catalyst concentration were varied. At standard conditions, the time elapsed between subsequent experiments was less than 45 min. An empirical reactor model is first fit to the data to better understand relationship between the catalyst, hydrogen, and carbon monoxide. This understanding is then applied to a mechanistic model. An overall empirical expression of the following form is proposed,

$$\frac{dC_P}{dt} = k(T) C_{Rh}^{a} P_{H}^{b} P_{CO}^{c} C_{oct}^{d} \qquad \textbf{(5-3)}$$

where C_P is the concentration of the aldehyde products, $k(T)$ is the reaction constant and is a function of temperature, C_{Rh} is the catalyst concentration, P_H is the hydrogen partial pressure, P_{CO} is the carbon monoxide partial pressure, C_{oct} is the 1-octene concentration, and a, b, c and d are reaction order constants. The temperature dependence of $k(T)$ can be described using the Arrhenius equation,

$$k(T) = A_0 \exp\left({}^{-E_a}\!\!\diagup_{RT} \right) \tag{5-4}$$

with A_0 being the pre-exponential factor, E_a the activation energy, and R the gas constant.

5.3.1. Differential Reactor Analysis

Under differential conditions, an appropriate starting point for kinetic analysis would be to assume that all other parameters are held constant during the experiment. When the conversion only reaches a few percent, neither the partial pressures of the carbon monoxide and hydrogen in the bubble nor the concentration of the alkene in the slug would change significantly. When these assumptions are valid and catalyst concentration is varied, the rate expression in Equation 5-3 can be simplified to:

$$r = k_{Rh} C_{Rh}^{a} \tag{5-5}$$

where k_{Rh} lumps the alkene, hydrogen, and carbon monoxide contribution with k. A value for parameter a could then be determined by minimizing the standard deviation of k_{Rh} across all catalyst concentrations, at each reaction temperature. A similar analysis could be carried out for variations in the partial pressures of hydrogen and carbon monoxide.

The Arrhenius equation could be linearized as follows,

$$\ln(k) = \ln(A_0) - \frac{E_a}{R} \cdot \frac{1}{T} \tag{5-6}$$

allowing for simple determination of the kinetic parameters. Using linear least squares regression, the parameters for the pre-exponential factor and the activation energy are related to the slope and intercept of the above linearized equation.

However, applying a differential reactor model to the current data set would strain the required assumptions. The experimental data set contains a number of data points with conversions of greater than 10%. For example, the partial pressure of carbon monoxide varied by over 50% at high temperature and low partial pressures. Additionally, as gas is consumed, the bubble volume decreases. This reduction in the unit cell length - the sum of the bubble and slug lengths - is associated with an increase in the residence time in the reactor. Thus, the reactor analysis must fully account for changes in the gas phase partial pressures as well as differences in residence time.

5.3.2. Reactor Model

The reactor model keeps track of each of the species that is varying during reaction, including the alkene reactant, the aldehyde product, and the gas composition of the gaseous species. The effect of the vapor pressure of 1-octene and toluene were not included in the analysis. At 105 °C, 1-octene and toluene represent less than 3% of the gaseous species in the bubble. Similarly, this would have negligible impact on the liquid phase composition since <0.2% of 1-octene loaded into the system is expected to partition to the gas phase. It is reported that for electron donating ligands such as phosphine, the rate determining step is hydrogenolysis.[143] Consequently, alkene insertion is sufficiently fast to not affect the observed reaction kinetics and the rate dependence on alkene concentration is assumed zero order. Additionally, the alkene concentration far exceeds the concentration of the catalyst. The initial alkene concentration for all experiments was 0.5 M, while the catalyst concentration was on the sub-millimolar scale.

The reactor model then takes the form:

$$r = k(T)\left(C_{Rh} / 1\ \mathrm{M}\right)^{a}\left(P_{H} / 1\ \mathrm{bar}\right)^{b}\left(P_{CO} / 1\ \mathrm{bar}\right)^{c} \tag{5-7}$$

$$\frac{dC_{P}}{dt} = r \tag{5-8}$$

$$\frac{dC_{oct}}{dt} = -r \tag{5-9}$$

$$\frac{dN_{H2}}{dt} = -rQ_{l} \tag{5-10}$$

$$\frac{dN_{CO}}{dt} = -rQ_{l} \tag{5-11}$$

where N is the number of moles of each species in the gas phase and Q_l is the volume of liquid. The number of moles of gas rather than concentration was used to make it easier to account for changes in volume in the gas phase. The number of moles of each gaseous species is then related to the partial pressure,

$$P_{i} = \frac{N_{i}}{\sum N_{i}} P \tag{5-12}$$

where *P* is the system pressure. The gas bubble is made up of three components: hydrogen, carbon monoxide, and nitrogen. The nitrogen does not participate in the reaction, but impacts the partial pressure in the bubble.

Normally a differential equation is solved with known starting and ending times. However, when the residence time in the reactor depends on the level of conversion, the end time is not known a priori. Instead, a fifth differential equation is added that relates the axial position *L* to the current time,

$$\frac{dL}{dt} = V_g \frac{\sum N_i}{\sum N_i^*} \frac{T}{T^*} + V_L \tag{5-13}$$

where V_g and V_l are the initial velocities for the gas and liquid, as calculated from the volumetric pump flow rates and room temperature. The *N* ratio corrects for the volume of the bubble lost due to reaction and the *T* ratio corrects for the temperature change between the pump, at room temperature, and the reactor, at elevated temperatures. The integration is carried out until L = 1350 mm, the total length of the reaction channel.

A nonlinear least squares regression is used to determine the values for the five parameters in this model: A_0, E_a, *a*, *b*, and *c*. The differential equation is solved for each set of experimental conditions. A total of 42 experiments were used to fit the model. The best set of parameters is then chosen by summing the square of the residuals of the experimental measurement against the model.

The parameter set determined from this analysis is shown in Table 5.1. The values for a 95% confidence interval are also shown. The confidence interval suggests a strong fit for the activation energy. The observed activation energy, E_a = 19.0 kcal/mol, compares favorably with the literature. The reported hydroformylation activation energy for small alkenes was 19.1 kcal/mol for ethene,[150] 20.6[134] and 19[151] kcal/mol for propylene, and 22 kcal/mol for 1-butene.[152] For larger alkenes, a wide range (11.8-28 kcal/mol) of activation energies have been reported for 1-hexene,[136] 1-decene,[137] and 1-dodecene.[153] This wide range might be explained by the complex, empirical rate expressions that were used to fit the data in these studies. These results also show that the reaction is first order in catalyst and hydrogen, and negative order in carbon monoxide. The reaction orders are consistent with the kinetics reported for unmodified rhodium carbonyl[154] and some phosphite ligand systems.[145] A comparison of the model predicted conversion and the experimental data is shown in Figure 5.6a-c. This figure demonstrates that the model is in good agreement with the data.

	E_a kcal/mol	$\ln(A_0)$ ln(M/s)	*a*	*b*	*c*
Value	19.0	25.2	1.03	0.96	-0.64
Confidence Interval (95%)	±0.8	±0.2	±0.15	±0.16	±0.08

Table 5.1. Parameters for the differential equation based power law model, as determined by nonlinear least squares.

The positive, first order relationship between the reaction rate and the concentration of rhodium and hydrogen is consistent with hydrogenolysis being the rate determining step (Figure 5.1 Step 6). Increasing the amount of catalyst in the system would increase the observed reaction rate. Similarly, increased hydrogen partial pressure would increase the rate of the rate controlling reaction. The effect of carbon monoxide concentration on reaction rate is more complex. As shown in Figure 5.1, carbon monoxide participates in the reaction in three separate elementary reactions. Two reactions remove catalyst from the main cycle: the reversible deactivation of the catalyst (Step 8) and the reversible formation of an acyl complex (Step 7). The third reaction is carbonyl addition to form an aldehyde intermediate (Step 4), which is part of the main catalytic cycle. The negative reaction order of carbon monoxide suggests that carbon monoxide has an inhibitory effect over the partial pressure range studied.

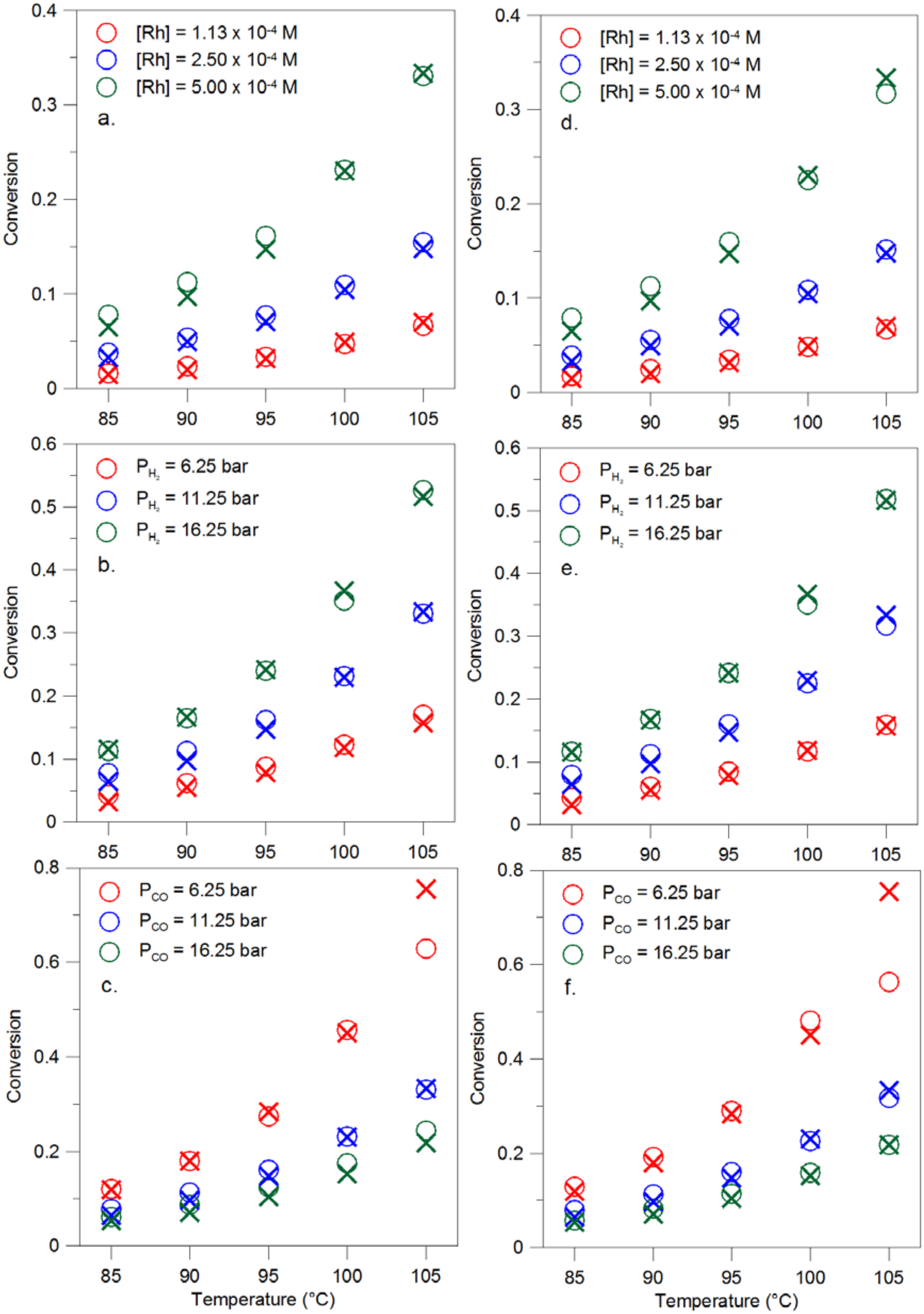

Figure 5.6. Comparison of model (○) to experimental (✕) data show good agreement for both the empirical (a-c) and mechanistic (d-f) models.

This observation suggests that Step 7 or Step 8 affects the overall reaction rate. Under different conditions, a different reaction rate would likely be determined. It has been reported in the literature that at low enough pressures of carbon monoxide, below 2 atm, the observed dependence on the pressure of carbon monoxide is positive.[136]

For completeness, the reactor analysis was repeated with the reaction rate including first order dependence on the alkene concentration (data not shown). This model did not fit the data as well, reinforcing the assumption that the overall model is zero order in alkene.

5.3.3. Mechanistic Model

The kinetic results above can be further reconciled with the reaction mechanism. As previously discussed, the data are consistent with hydrogenolysis (Figure 5.1, Step 6) being the rate determining step. The rate expression has no dependence on alkene addition (Figure 5.1, Step 2). The absence of a positive response to carbon monoxide pressure suggests that carbon monoxide addition (Figure 5.1, Step 6) in the catalytic cycle does not affect the overall rate. Together, these observations suggest that most of the rhodium is held in the rhodium-acyl complex. The negative observed order for carbon monoxide shows that carbon monoxide has the effect of inhibiting the overall reaction. In the mechanism (Figure 5.1), there are two reactions (Steps 7-8) involving carbon monoxide that remove rhodium from the cycle. Step 7 is expected to dominate, given that the most common rhodium species is the intermediate preceding hydrogenolysis. Carbon monoxide is generally found to inhibit the hydroformylation reaction, regardless of whether hydrogenolysis or alkene coordination is the rate-determining step. In the case of alkene coordination being rate determining, Step 8 would likely dominate over Step 7 and provide the same overall order. A simplified reaction mechanism is proposed in Figure 5.7.

The desired kinetic expression relates the rate of formation of the aldehyde product *P* to measurable species in the system. The hydrogenolysis reaction, r_1, has been found to be the rate determining step,

$$r_1 = \frac{dP}{dt} = k_1 P_{H_2}\left[Rh^*\right] \quad \textbf{(5-14)}$$

where k_1 is a reaction constant. The quasi-steady-state concentration of the rhodium-acyl intermediate Rh^* is difficult to measure directly and is a function of other reaction parameters. The other reactions in the original cycle have been simplified to a single reaction r_2,

$$r_2 = k_2\left[R\right]P_{CO}\left[Rh\right] \quad \textbf{(5-15)}$$

where *R* is the reactant alkene. In a catalytic cycle, the rates of all reactions are the same at steady state, i.e.,

$$r_1 = r_2 \quad \textbf{(5-16)}$$

Since step is rate controlling, we expect that [Rh^*] >> [*Rh*] implying that [*Rh*] is approximately 0. Rhodium species are catalytic and therefore not consumed during reaction. A mass balance

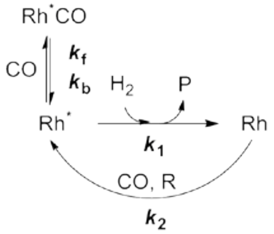

Figure 5.7. Simplified reaction mechanism used for kinetic analysis.

leads to the following expression:

$$\left[Rh_0\right]=\left[Rh\right]+\left[Rh^*\right]+\left[Rh^*CO\right]\approx\left[Rh^*\right]+\left[Rh^*CO\right] \qquad \textbf{(5-17)}$$

where [*Rh₀*] is the concentration of rhodium loaded into the system. A rate expression can be prepared for rhodium-acyl species Rh^*,

$$\frac{dRh^*}{dt}=-k_1P_{H_2}\left[Rh^*\right]+k_2\left[R\right]P_{CO}\left[Rh\right]+k_f\left[Rh^*CO\right]-k_bP_{CO}\left[Rh^*\right] \qquad \textbf{(5-18)}$$

The first two terms cancel according to Equation 5-16. At equilibrium, Equation 5-18 can be set to 0. Solving for [Rh^*] and substituting for [Rh^*CO],

$$\left[Rh^*\right]=\frac{k_f\left[Rh^*CO\right]}{k_bP_{CO}}=\frac{k_f\left(\left[Rh_0\right]-\left[Rh^*\right]\right)}{k_bP_{CO}} \qquad \textbf{(5-19)}$$

$$\left[Rh^*\right]=\frac{K_{eq}\left[Rh_0\right]P_{CO}^{-1}}{1+K_{eq}P_{CO}^{-1}} \qquad \textbf{(5-20)}$$

$$K_{eq}={}^{k_f}\!\big/_{k_b} \qquad \textbf{(5-21)}$$

Combining Equation 5-20 with Equation 5-14, yields the final kinetic expression,

$$\frac{dP}{dt}=\frac{k_1K_{eq}P_{H_2}\left[Rh_0\right]P_{CO}^{-1}}{1+K_{eq}P_{CO}^{-1}}=\frac{k_1P_{H_2}\left[Rh_0\right]}{1+P_{CO}/K_{eq}} \qquad \textbf{(5-22)}$$

In the limit where K_{eq} is small, Equation 5-22 collapses to Equation 5-3, where c = -1. A small value for K_{eq} implies that the rate of the backward reaction to remove the catalyst from the cycle is larger than the forward reaction. On the other hand, if K_{eq} was large, the overall dependence on carbon monoxide would be zero order. Thus this mechanism bounds the possible reaction order of carbon monoxide to be between -1 and 0. The fitted parameter, $c = -0.644$, lies within this expected range.

This three parameter model - A_0, E_a, and K_{eq} - was fit using a nonlinear least squares regression. The parameters can be found in the top row of Table 5.2. This activation energy is nearly identical to the one determined for the empirical reactor model. From the value of K_{eq}, it is possible to estimate the fraction of rhodium that is held in the catalytically active form. For the standard partial pressure of carbon monoxide, $P_{CO} = 11.25$ bar, 38.9% of the rhodium loaded into the system is in the main catalyst cycle. The remainder is held in the kinetically inactive form.

	E_a / (kcal/mol)	ln(A_0 / (M/s))	K_{eq} / bar	G / (kcal/mol)
$K_{eq} \neq f(T)$	19.0 ± 2.4	24.8 ± 3.3	3.15 ± 1.38	
$K_{eq} = f(T)$	18.9 ± 2.3	24.7 ± 3.2		-0.80 ± 0.33

Table 5.2. Parameters (with 95% confidence intervals) for the mechanistic model assuming equilibrium between the active and inactive rhodium complexes.

A comparison can also be made between the carbon monoxide dependence in the empirical and mechanistic models. In the empirical power law model,

$$r_p \propto P_{CO}^{-0.644} \tag{5-23}$$

and in the mechanistic model,

$$r_m \propto \frac{1}{1 + P_{CO}/K_{eq}} \tag{5-24}$$

The initial carbon monoxide pressure took one of three values during the experiments. Both r_p and r_m provide a very similar dependence on P_{CO}, as shown in Figure 5.8.

In the preceding analysis, K_{eq} has been considered independent of temperature. The model was expanded to include temperature dependence,

$$\ln\left(K_{eq}\right) = {-\Delta G}/{RT} \tag{5-25}$$

where ΔG is a constant Gibbs energy of reaction. There is insufficient temperature resolution in the data to resolve a temperature dependent expression for ΔG. These three parameters - A_0, E_a, and ΔG - were also fit using nonlinear least squares (Table 5.2, bottom row). The value for the Gibbs energy, ΔG = -0.80 kcal/mol, demonstrates that the equilibrium constant K_{eq} has a very low temperature dependence. Over the experimental temperature range (85-105 °C), the value of K_{eq} is calculated to vary between 2.91-3.09 bar. A comparison of the predicted conversion and the experimental data is shown in Figure 5.6d-f. This figure demonstrates that the model is in good agreement with the data and is nearly identical to a plot of the empirical

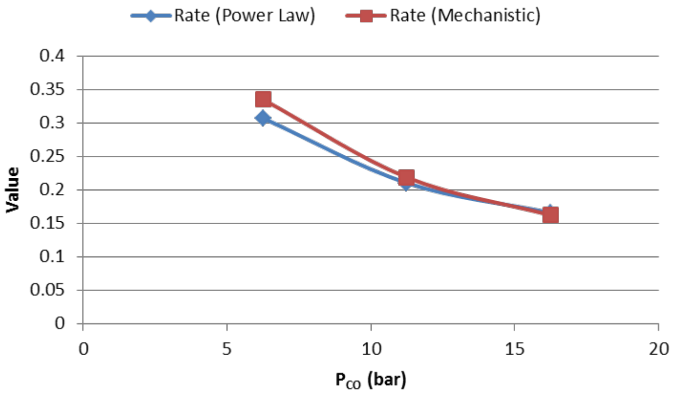

Figure 5.8. The mechanistic and power law models show a similar dependence on P_{CO} over the experimental P_{CO} range.

model against the experimental data (Figure 5.6a-c).

5.4. Absence of Mass Transfer Limitations

The utility of the designed system depends greatly on directly observing the kinetic reaction rate. If mass transfer rates slow and become competitive with reaction rates, the observed rates will no longer be dominated by kinetic effects. By comparing the rate of transfer of a gas species to the liquid phase, assumed to be the rate determining mass transfer step, with the rate of consumption of the gas due to reaction, the importance of mass transfer on the observed reaction rate could be estimated. To limit the effect of mass transfer on reaction rates, the gas and liquid flow rates were similar. Longer bubbles and slugs are undesirable because they reduce the mass transfer rate in the system. This reduction in the mass transfer rate is caused by the reduction of the interfacial area between the two phases as well as increased diffusion length scales within a single phase.

Of the two reacting gases that were consumed during hydroformylation, carbon monoxide would likely have the slower mass transfer because it has a lower solubility and slower diffusion rate in toluene. In addition, the highest reaction rate observed (1.5×10^{-3} M/s) coincided with the lowest carbon monoxide pressure of 6.25 bar. A mass balance was performed on the dissolved carbon monoxide to evaluate any potential effect of mass transfer,

$$-r_{CO} = \frac{dC_{CO}}{dt} = k_L a\left(C_{CO}^{*} - C_{CO}\right) \qquad \textbf{(5-26)}$$

where r_{CO} is the rate of disappearance of carbon monoxide due to reaction, C_{CO} is the concentration of carbon monoxide in the bulk liquid, k_La is the mass transfer coefficient, and

C_{CO}^{*} is the equilibrium liquid-phase carbon monoxide concentration in the absence of reaction. The equilibrium carbon monoxide concentration can be estimated using Henry's law,

$$C_{CO}^{*} = p_{CO} / k_{H,CO} \tag{5-27}$$

Here p_{CO} is the partial pressure of carbon monoxide in the gas phase and $k_{H,CO}$ is the Henry's law constant for carbon monoxide. Jauregui-Haza et al.[155] reported a Henry's law constant of 119.4 bar L/mol for carbon monoxide in toluene.

Yue et al.[117] prepared an experimental study of gas-liquid mass transfer in square micro channels and obtained an empirical correlation for the estimation of the mass transfer coefficient, $k_L a$

$$k_L a = \frac{2}{d_h}\left(\frac{DU_B}{L_B + L_S}\right)^{0.5}\left(\frac{L_B}{L_B + L_S}\right)^{0.3} \tag{5-28}$$

where d_h is the hydraulic diameter of the channel, D is the diffusivity of the gas in the liquid, U_B is the gas bubble velocity, and L_B and L_S are the lengths of the gas bubble and liquid slug, respectively. The hydraulic diameter of a square channel is equal to the length of its side, which was 400 µm for the microreactor. The diffusivity of carbon monoxide in toluene has been reported to be 9.85×10^{-9} m^2/s.[156] For a gas bubble velocity of 5.7 mm/s and gas bubble/liquid slug length of 800 µm, the corresponding mass transfer coefficient was $k_L a = 0.76$ s^{-1}.

The concentration of the bulk in Equation 5-26 was found to be 0.050 M and the equilibrium concentration in the absence of reaction was 0.052 M. This suggests that mass transfer limitations cause a concentration gradient of <4% in the liquid phase, in this worst case scenario. For the remaining experiments the gradient would be much less than 4% due to slower reaction rates. Therefore, the system is considered to be kinetically limited.

5.5. Octene Isomerization

Initial hydroformylation experiments were conducted using a single liquid syringe pump. The pump was loaded with a mixture of the rhodium catalyst, 1-octene, and toluene. During experimentation, an unknown peak, associated with the C-H stretch of a trans-alkene, was observed at 973 cm^{-1}. This peak increased with time, but was unaffected by reaction conditions. In addition, freshly prepared solution contained a higher concentration of 1-octene than did week old solution. The longer that the reaction mixture was stored, the larger the 973 cm^{-1} peak became. These observations suggest that 1-octene was isomerizing to 2-octene in the starting mixture in the presence of the rhodium catalyst. The lack of a temperature effect suggests that the isomerization does not occur during hydroformylation. To test this hypothesis, two liquid pumps were used to separate the catalyst from the 1-octene, prior to reaction. The streams joined in the reactor just before gas was added to the stream. The concentration of 2-octene after reaction was negligible, even after the solutions were stored for a week. This result confirmed that isomerization of 1-octene occurred in the presence of rhodium catalyst.

The hydroformylation mechanism provides some insight into the isomerization reaction. Focusing on the alkene coordination step, Figure 5.9 shows the series of reactions that occur during isomerization of 1-octene to 2-octene. This reaction is known in the literature, but not always reported in hydroformylation experiments.[157] When 1-octene reversibly coordinates to the metal center, an internal rearrangement occurs resulting in a bond forming with either the terminal or internal carbon. When the terminal bond forms, the reverse reaction will always produce the terminal alkene, 1-octene. This terminal bond is also required for the dominant linear aldehyde product to form. When the internal bond forms, the reverse reaction will form either the terminal alkene or the internal alkene. The internal bond formation is also associated with the branched product formation. At room temperature, isomerization occurs slowly, suggesting the formation of observed concentration 2-octene has not reached equilibrium.

In the absence of carbon monoxide and hydrogen, the hydroformylation reaction could not proceed past Steps 3 or 9 in Figure 5.1. To further explore the isomerization reaction, a set of experiments analogous to hydroformylation were performed. The rhodium catalyst and 1-octene were supplied from two different syringe pumps, eliminating isomerization prereaction.

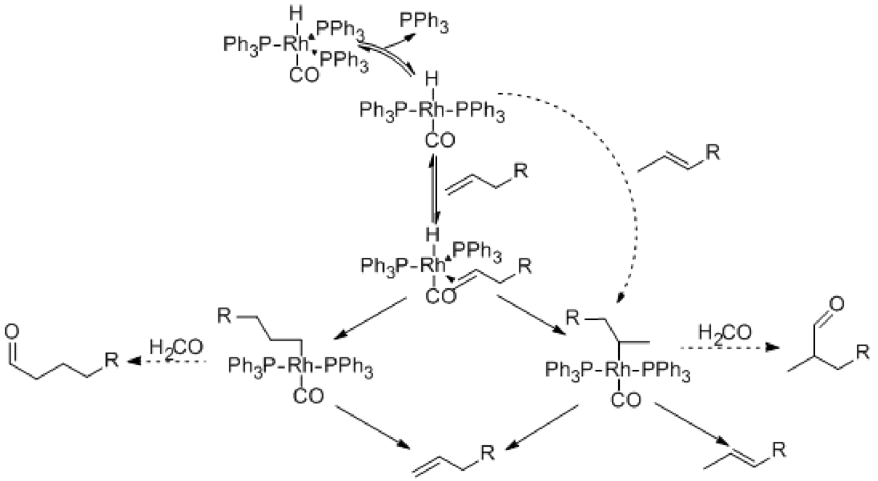

Figure 5.9. Alkene coordination on rhodium catalyst can occur at two possible carbon attachment points. When an internal carbon is coordinated, the reverse reaction can result in an internal alkene being produced.

The gas phase was comprised of nitrogen, which is inert. The temperature was varied to probe its effect on the isomerization reaction rate (Figure 5.10L). The conversion of 1-octene to 2-octene increased exponentially until the temperature passed 110 °C. As temperature increased further, the conversion decreased suggesting that the catalyst began to deactivate. Fitting only the points taken at temperatures below 110 °C (Figure 5.10R), an apparent activation energy of 16.7 kcal/mol was calculated.

During hydroformylation reactions, isomerization is not observed under the same conditions. This suggests that the addition of carbon monoxide (Figure 5.1, Step 4) is much faster than the dissociation of alkene from the rhodium complexes. It is only in the absence of carbon monoxide that isomerization is observed. Two liquid pumps were used for all hydroformylation experiments, which proved effective at preventing observable isomerization. Another solution was to add excess ligand, triphenyl phosphine, which is expected to slow the isomerization reaction significantly. A 2:1 mass ratio of ligand to catalyst was added to the catalyst solution.

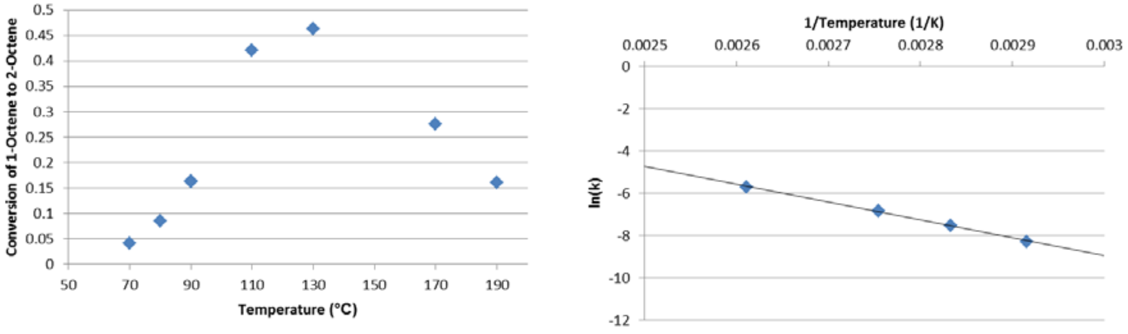

Figure 5.10. Left: The conversion of 1-octene to 2-octene is plotted as a function of temperature. At lower temperatures, an exponential relationship exists, while at higher temperature, significant catalyst deactivation is observed. Right: An activation energy of 16.7 kcal/mol is calculated using low temperature data.

Chapter 6. Heterogeneous Catalysis – Hydrogenation

6.1. Introduction and Reaction Literature

Hydrogenation is a class of reaction that adds molecular hydrogen to another compound and is a prominent three-phase heterogeneous chemistry. Hydrogen is most commonly added across a carbon-carbon double bond in an alkene. Hydrogenation reactions are of paramount importance across many different industries. They are the most important organic reaction in the production of fine chemicals.[158, 159] In the petrochemical industry, crude oil containing multiple double bonds are hydrogenated. Hydrotreating, currently heavily employed in oil refining, will remain crucially important during the upgrading of pyrolysis to biofuel.[160] Untreated pyrolysis oils contain many unstable functional groups. These groups can lead to polymerization during storage as well as increase the difficulty of blending biofuel with traditional fuels. Hydrogen can also displace oxygen in pyrolysis oil, improving its energy density. Hydrogenation is important to even the food industry, where it is used to saturate vegetable oil.[161] For example, soybean oil is completely or partially hydrogenated to improve its stability. Unsaturated oils, those containing many double bonds, are highly reactive and have short shelf lives due to oxygenation reactions.

Hydrogenation was chosen to demonstrate the high-pressure, three-phase reactor for a number of reasons. Hydrogenation reactions can be challenging reactions to run in traditional systems. Hydrogen gas has low solubility in many solvents, typically three orders of magnitude lower than the alkene substrate. This low solubility introduces mass transfer limitations under many reaction conditions. Hydrogenations are therefore typically run at pressures of up to

100 bar which improves the hydrogen concentration in the liquid phase. However, high-pressure hydrogen, contained in large reactors, increases the operational risk. In addition, hydrogenations are exothermic, making temperature control challenging. Microreactors overcome many of these challenges through improved heat and mass transfer. Hydrogenations have been previously studied in microreactors at atmospheric conditions.[120] The current three-phase microreactor system is particularly suited to operate at the higher pressures typical of hydrogenation. Even in a microreactor, the hydrogenation reaction can be so fast that mass transfer limitations are observed. Thus, by studying a known reaction such as hydrogenation, the mass transfer performance of the new microreactor can be determined

A variety of hydrogenation reactions were studied in the multiphase system. Two catalysts were prepared, 5% platinum on silica and 5% platinum on alumina, and two substrates were reacted, cyclohexene and 1-octene. Both substrates have similar heats of reaction;[162] the standard heat of reaction for cyclohexene hydrogenation is 117.78 KJ/mol and for 1-octene hydrogenation is 125.52 KJ/mol. Cyclohexene is a particularly attractive substrate because isomerization reactions, which are common under hydrogenation conditions, have no impact on its structure.

Heterogeneously catalyzed hydrogenation reactions are characterized by the addition of hydrogen to an alkene on a catalyst surface. The mechanism is well known and was first identified by Horiuti and Polanyi.[163] The Horiuti-Polanyi mechanism proceeds through a number of steps: (1) Hydrogen dissociates on the surface. (2) The carbon-carbon double bond on the alkene is broken, forming two new bonds with the metal surface. (3) Addition of the first hydrogen atom to form a reversible intermediate. (4) Addition of the second hydrogen atom releases the saturated product; this step is often considered irreversible under hydrogenating conditions.

A variety of hydrocarbon reactions can occur in the presence of platinum catalyst depending on the conditions.[164] These reactions are plotted in Figure 6.1 along with their reaction rate. The turnover rates associated with the various reactions vary greatly and their prominence can be adjusted by altering the reaction temperature. For example, more complex reactions such as isomerization, cyclization, and dehydrogenation have activation energies in the range of E_a = 35-45 kcal/mol. Hydrogenations, on the other hand, have lower activation energies in the range of of E_a = 6-12 kcal/mol. Thus hydrogenations are typically performed at lower temperatures of around 300 K to improve selectivity.

6.2. Catalyst Preparation

A classic method for catalyst preparation involves impregnating a catalyst support with a

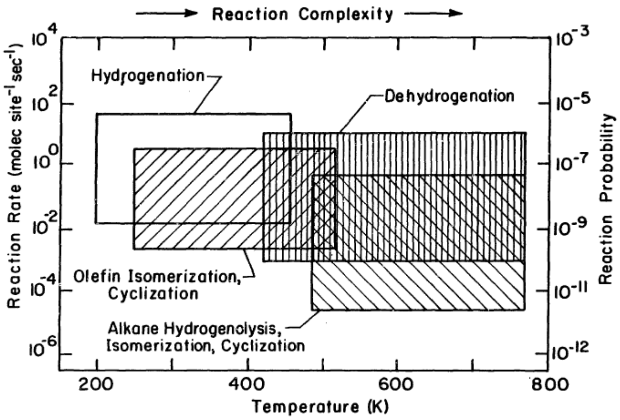

Figure 6.1. Block diagram of hydrocarbon conversion over platinum catalysts shows the approximate reaction rate range and the most commonly studied temperatures.[164]

catalytically active metal. This catalyst is then activated through a reduction reaction. Catalytic activity generally increases with the active surface area of the catalyst. Porous support materials are used as the basis for heterogeneous catalysis to take advantage of their high surface areas which are in the range of 100 to 400 m^2/g.[164] The supports are generally materials like silica, alumina, or carbon. The support material can have a larger role on the reaction than implied by its name. It can participate in the reaction and alter the rate or observed mechanism. For example, the support can help stabilize a reaction intermediate. Modern supports generally have very well defined microstructures. Impregnation of high surface area support results in highly-dispersed nanometer-sized metal clusters, ideally a single atom deep. Platinum is often used as a metal due to its high activity and low tendency to leach.

A number of high surface area supports are commercially available.[165] Alumina (aluminum oxide) is one such common support. When used as a catalyst support, gamma alumina is preferred because this structure has a much higher surface area than alpha alumina. Silica (silicon dioxide) is another traditional catalyst support. Its surface is thought to be more inert than alumina.

It is impossible to commercially procure small quantities of prepared catalyst particles with a narrow size distribution. The design of the heterogeneous reactor dictates the possible size range for the catalyst particles. The catalyst retaining weirs provide a lower bound of 20 µm for the possible particle size. In an effort to prevent channeling and other flow distribution issues, the diameter of the catalyst support should be less than 10% of the channel diameter, which provides the upper bound for the catalyst size. Instead of purchasing prepared catalyst, the desired metal is deposited on a commerically prepared support. While prepared catalyst can be sieved to isolate the desired fraction, this proves to be an expensive proposition. The metal loaded catalyst is far more expensive than the catalyst support. The support material, like the purchased catalyst, generally comes in a wide size distribution. Instead, the support is sieved prior to impregnation to ensure that no platinum is wasted on catalyst particles that are outside the desired size range.

Sieving was performed using a stack of copper mesh trays. The trays are available in standard sizes; the 38, 53, and 72 µm mesh sizes were used. The stack consisted of the three trays stacked largest to smallest from top to bottom. A pan at the bottom of the stack was used to collect the smallest particles. This tray arrangement allowed two potential fractions of the catalyst support to be recovered: 38-53 µm and 53-72 µm. Two sieving techniques were employed. The first is tapping sieving. In this method, powder is placed directly in the top sieve. The stack is moved in a horizontal circle, inducing motion of the powder over the mesh surface. The circular motion is coupled with tapping that introduces vertical motion in the sieves. This vertical motion serves to reorient the particles in an effort to find an angle in which they could pass through the sieve. Wet sieving is an alternate sieving technique in which a compatible solvent (water, ethanol, isopropanol) wets the desired species. While dry sieving is typically performed, wet sieving is employed when the sample cannot be dried or when agglomeration is an issue.

Two substrates, silica and alumina, were chosen as catalyst supports. The silica support (Alfa Aeser 42570) had a near-neutral pH and a surface area of 500-600 m^2/g. The diameter of the particles was expected to be 38-63 µm (-230+400 mesh). The alumina (Alfa Aeser 43266) was gamma-phase with a surface area of 200 m^2/g. The average particle size was 400 µm. Both supports were sieved using the techniques described above. Wet sieving was required to disrupt the static forces in the dry powder. The liquid was successful in transporting the small particles through the sieve meshes. However, wet sieving increased the difficulty of sieving the larger sized particles. Thus a staged approach was employed. Each support sample was first wet sieved, before being allowed to dry. The liquid in the bottom of the pan was discarded. Once dry, tap sieving was employed. The sample was successfully fractionated using this method.

Laser light scattering measurements were taken to characterize the fractioned silica support. Figure 6.2 shows the unsieved support and the 38-53 µm fraction after sieving. The expected particle size range of the unsieved silica was 38-63 µm. Sieving removed the very fine particles

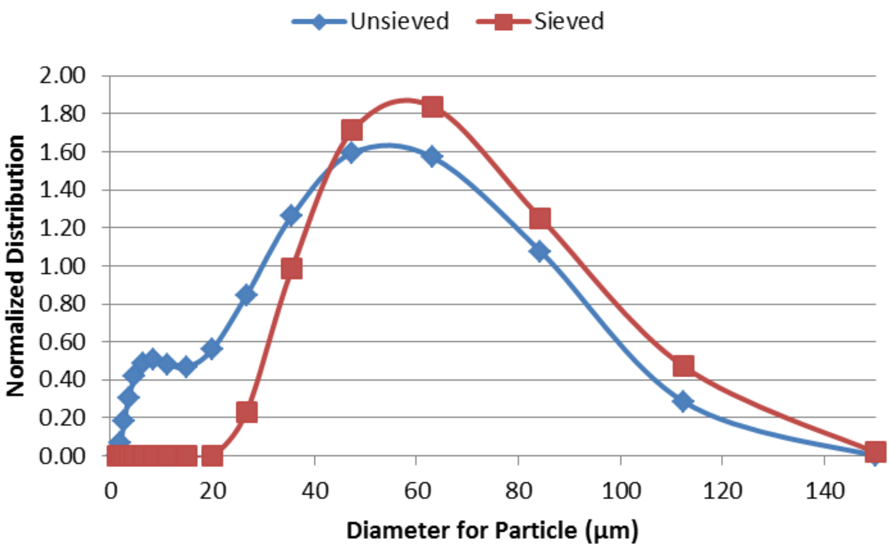

Figure 6.2. Comparison of silica support size profiles before and after sieving show that fine particles are removed.

from the distribution, while leaving the distribution of the larger particles unchanged. These smaller particles would have travelled through the retaining wall in the reactor and could potentially agglomerate and clog the system downstream of the reactor. The long tail of larger particles suggests that agglomeration reoccurred after sieving. The shape of the tail is similar for both samples.

To better understand the surface area and pore volume of the silica catalyst, BET analysis was performed. During BET analysis, the physical absorption of gas on to the surface is probed. As the temperature is varied, isotherms are recorded from which surface area is calculated. From this analysis, a number of parameters were estimated. The measured surface area was 420 m^2/g, which is somewhat below the 500-600 m^2/g specified by the supplier. The average pore volume was calculated to be 0.57 ml/g with an average pore diameter of 5.5 nm.

To prepare the final catalyst, platinum metal was deposited into the substrate to achieve a weight loading of 5%. For the catalyst to fully utilize the increased surface area of the support, the platinum must be deposited within the pore structure. Incipient wetness impregnation is a classic method for preparing catalyst with metal contained in the porous support.[166, 167] As liquid is initially added to the porous material, capillary forces draw the liquid into the pores. As the pores fill, the powdered support loses its ability to 'flow' and instead begins to cake. This caking signals the end point of incipient wetness. At this stage the pores are completely filled with liquid and a thin film wets the exterior of the particles. While this method appears simple, there is an art to properly identifying the endpoint. It has been shown that when different researchers are asked to identify the endpoint, the total volume of liquid dispensed can vary by as much as 20%.[168] To prepare a solution with the proper concentration, a good estimate of the volume that leads to incipient wetness is required. This volume can be calculated from the known pore volume.

An alternate method for estimating pore volume is described by McDaniel and Hottovy.[168] While BET analysis is more accurate, this method more closely resembles incipient wetness impregnation. They outline a highly repeatable method for determining the total porosity of silica catalysts using centrifugation. Special centrifugation tubes are required which consist of two nested tubes with a porous frit isolating the inner tube from the outer tube. When a sample is placed in this tube and centrifuged, the excess liquid can be recovered in the larger tube, while the sample retained in the smaller tube is at incipient wetness.

The centrifuge porosity measurement method was used as the basis for a new method to perform incipient wetness impregnation. Using an estimate of the available pore volume, a solution containing chloroplatinic acid hexahydrate in water was prepared. The important performance parameters are enumerated in Table 6.1. The concentration of chloroplatinic acid was chosen so that a 5% weight loading was deposited in the pores of the catalyst support. The catalyst support was dried at 115 °C overnight to ensure that the entire pore volume was available for the catalyst solution. Excess solution was prepared and added to a known amount of dry catalyst support. The wet catalyst was then loaded into VectaSpin 3 centrifuge filter tubes and centrifuged. McDaniel and Hottovy[168] show that high reproducibility in water retention volumes were achieved at both 1500 rpm and 2000 rpm. Thus the loaded centrifuge

	Silica	Alumina
Support Weight (g)	2.0	2.0
Porosity - BET (ml/g)	0.57	0.3
Porosity - Centrifuge (ml/g)	0.87	
Excess Solution (ml)	0.85	0.4
Weight %: Platinum	5.0%	5.0%
Incipient Wetness Volume (ml)	1.14	0.60
Total Volume (ml)	1.99	1.00
Weight Precursor (g)	0.46	0.44
Platinum Concentration (M)	0.45	0.85

Table 6.1. Key process parameters required to prepare 5% platinum on silica or alumina catalyst.

tubes were spun at 1500 rpm for 20 min. The samples were initially dried at 80 °C for 2 hr before the temperature was increased to 115 °C and baked overnight.

At this stage, unreduced platinum was present on the surfaces of the catalyst. Reduction under hydrogen gas transforms the platinum to the catalytically active oxidation state. The reduction was carried out at two different scales: an external gram-scale tubular reactor and an in situ multiphase microreactor capable of reducing milligram quantities prior to reaction. In the tubular reactor, a 1/4 inch tube was filled with catalyst, retained by steel wool. This tube was then placed in a quartz tubular furnace. A mixture of 10% hydrogen in nitrogen, controlled by mass flow controllers, was flowed through the reactor. The furnace temperature was ramped to 400 °C at a rate of 10 °C/min. The furnace was then held at this temperature for 5 hours, before being cooling to room temperature. A similar procedure was used to reduce the catalyst in the microreactor system. The microreactor was loaded with catalyst and connected to the high-pressure system. Hydrogen was loaded into the gas syringe pump, which was then run at a constant flow rate of 30 µl/min. The system was operated at a pressure of 5 bar. The reactor was heated to a temperature of 300 °C at a rate of 10 °C/min and held for 5 hours before the temperature was reduced to room temperature. In situ reduction allowed the post-reduction catalyst to be studied without exposure to air.

6.3. Catalyst Deactivation

During operation, catalyst deactivation was a constant challenge. Both the platinum on silica and the platinum on alumina catalysts showed deactivation over time. There are four basic deactivation methods for supported catalyst: poisoning, fouling, sintering, and leaching.[165] Poisoning is the irreversible absorption of a contaminant on an active metal site. This contamination blocks the active site, reducing the rate of reaction. Fouling occurs when a material blocks physical access to active sites on the catalyst surface. Polymerization is a common form of fouling. Fouling can generally be reversed by combusting away coked material. Sintering occurs when the catalytic metal agglomerates, reducing the exposed metal surface area, which in turn reduces the reaction rate. Sintering is most likely to occur when the metal is heated above the Hüttig Temperature. For platinum metal, the Hüttig Temperature is 340 °C. Catalyst deactivation was observed at temperatures below 115 °C suggesting that sintering is not the cause of the deactivation. The final mechanism for catalyst deactivation is the leaching of metal to the vapor or liquid stream. Metal leaching leads to the gradual reduction of metal loading on the catalyst. Platinum metal is not expected to leach.

The deactivation was probed by comparing different catalysts and different substrates. Cyclohexene hydrogenation was explored first because cyclohexene is less susceptible to side reactions than normal alkenes.[169, 170] The hydrogenation of 1-octene was subsequently explored as an alternative to cyclohexene, but rapid deactivation was observed under all conditions

6.3.1. Cyclohexene Hydrogenation

While the reactor was operated at steady state, the observed reaction rate of cyclohexene decreased with time, failing to reach steady state. Under constant conditions, the reaction rate of cyclohexene hydrogenation over platinum on alumina catalyst was shown to fall over 80% over the course of 5 hours (Figure 6.3).

Early attempts to understand and limit the deactivation focused on the contamination of cyclohexene. Infrared analysis was used to characterize the reaction. Over the course of several days of experimentation, the spectra contained increasing levels of contamination. The most apparent new peak was centered at 3300 cm^{-1} associated with an OH stretch (Figure 6.4).

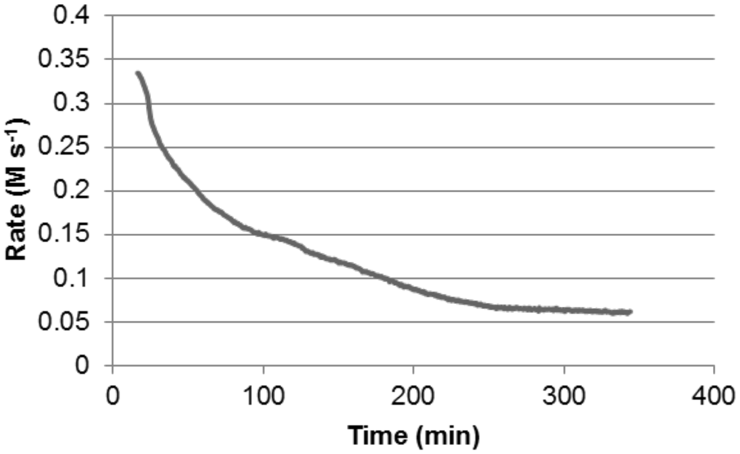

Figure 6.3. Neat cyclohexene was reacted with hydrogen at 30 bar. This room temperature reaction exhibited strong catalytic deactivation over time.

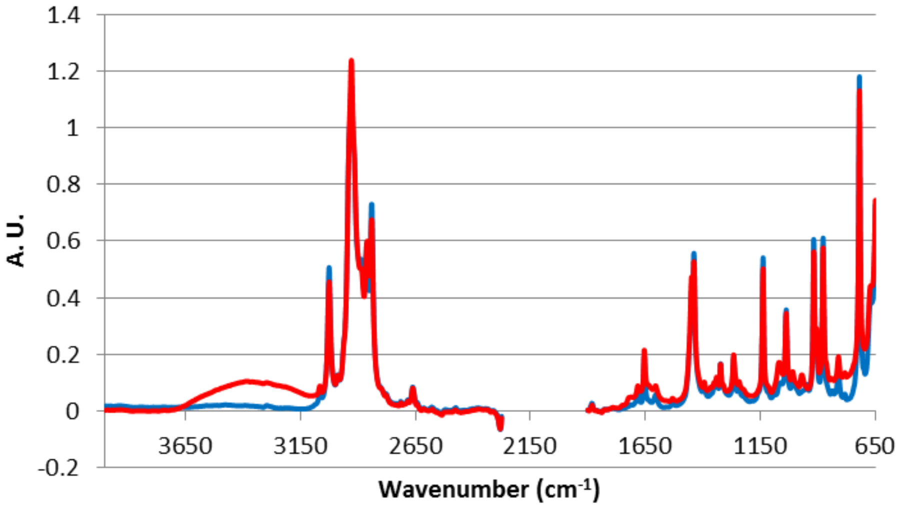

Figure 6.4. Spectral comparison of neat cyclohexene data. Contamination is evident in the red spectrum due to an OH stretch around 3300 cm^{-1}.

This stretch could be caused by water or some other hydroxide containing species. It is reported that oxygen contamination, resulting in the formation of hydroperoxides, is a common cause of catalyst deactivation during cyclohexene hydrogenation.[169, 170] When the hydroperoxide reacts with the catalyst surface, the remaining oxygen bonds irreversibly with an active platinum site.

The stock solution of cyclohexene was analyzed using GC/MS. Four contaminant peaks were observed (Figure 6.5). All of the peaks are likely associated with oxygenated cyclohexene molecules. Two samples of cyclohexene from the same source were analyzed two weeks apart (April 21 and May 4). The increased peak heights in the later sample suggest that further contamination had occurred during storage. The spectra from two of the peaks, at 2.71 and 2.95 min, were positively identified as 2-cyclohexen-1-ol and 2-cyclohexen-1-one through comparison with reference mass spectra. The spectra of the remaining two peaks are consistent with 3-cyclohexen-1-ol and 2,4-cyclohexadien-1-ol, though reference spectra do not

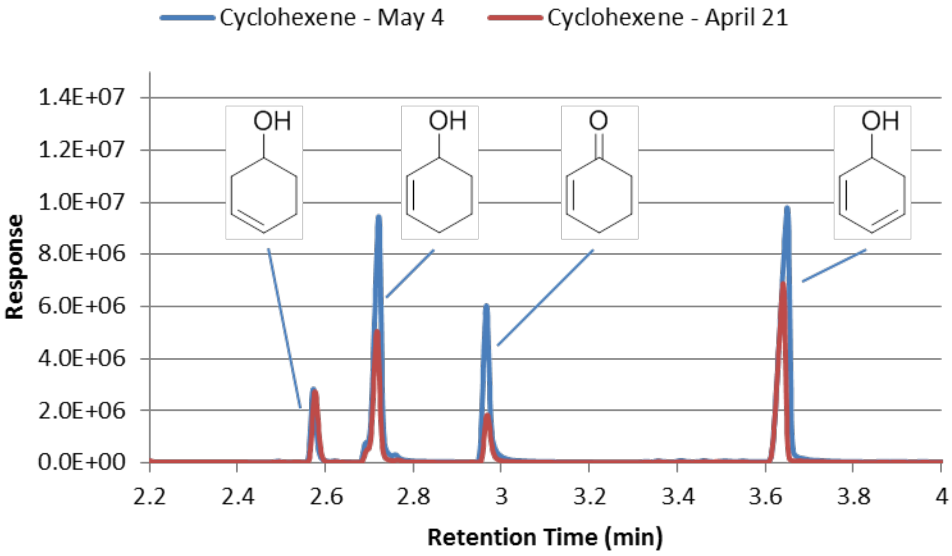

Figure 6.5. Four oxygen-containing contaminant peaks were identified using GC/MS analysis. The sample, which had been exposed to air longer (May 4), had more contamination.

exist to allow definitive identification. These results are summarized in Table 6.2. The presence of oxygenated species, which could reasonably be derived from hydroperoxides, is thought to contribute to the rapid deactivation of the platinum catalyst.

A number of methods are described in the literature for the purification of cyclohexene.[167, 169, 170] These methods rely on sparging cyclohexene with an inert gas such as helium to remove

Retention Time (min)	Proposed Molecule	Sample % (4/22)	Sample % (5/4)
1.91	Cyclohexene	97.62	95.02
2.56	3-cyclohexen-1-ol	0.33	0.34
2.71	2-cyclohexen-1-ol	0.71	1.61
2.95	2-cyclohexen-1-one	0.25	0.93
3.63	2,4-cyclohexadien-1-ol	1.08	2.11

Table 6.2. Comparison of the contamination level from two samples. The majority of the samples remain cyclohexene. Aldrich's specification was 99% cyclohexene.

molecular oxygen before contacting it with an activated bed of alumina to bind and remove oxygen-containing contaminants. Based on these methods, a number of cleaning methods were attempted. Initial purification attempts involved sparging a cyclohexene sample with nitrogen in the presence of alumina. Using a rapid IR screen, contamination similar to Figure 6.4 was still observed. A similar result was achieved using an alumina column, suggesting that the contamination level was too high, or contact time was too short to remove the contaminants. A final purification attempt was made utilizing fresh cyclohexene. Molecular sieves and alumina were added to the sample, which was then loaded into the high-pressure system. All manipulations were conducted under an inert atmosphere. The molecular sieves would remove any water contamination. Full details of this procedure are outlined in Section 4.1.2. IR analysis of this sample displays a clean background, without a hydroxide peak at 3300 cm^{-1}. Unfortunately, continued deactivation of the platinum on alumina catalyst was still observed. The platinum on silica catalyst showed more limited deactivation using this cleaned cyclohexene. Figure 6.6 shows the initial deactivation of the platinum on silica catalyst before reaching a steady state at 25 °C. The temperature was then increased to 45 °C and a flat reaction rate is again observed.

Temperature does not appear to affect the rate of catalyst deactivation when operated in a kinetically limited regime. To probe the effect of temperature on deactivation, the temperature was varied during the reaction of clean cyclohexene with the platinum on alumina catalyst (Figure 6.7). The rate of reduction in catalyst activity remained largely constant. When the temperature was raised from 50 °C to 85 °C and back to 50 °C, the rate followed the same trend as if the temperature had simply remained at 50 °C.

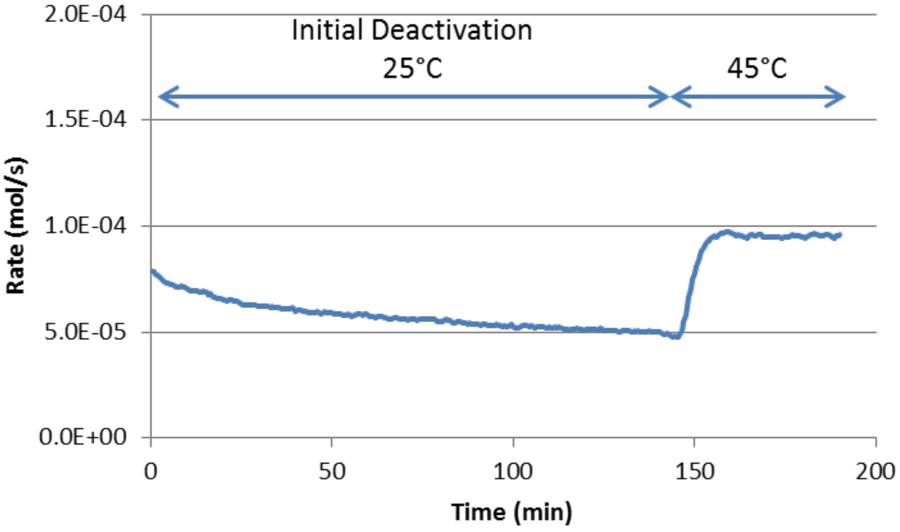

Figure 6.6. When cyclohexene is reacted with the platinum on silica catalyst in the absence of oxygen, significantly less deactivation is observed. No deactivation is observed as the temperature is increased.

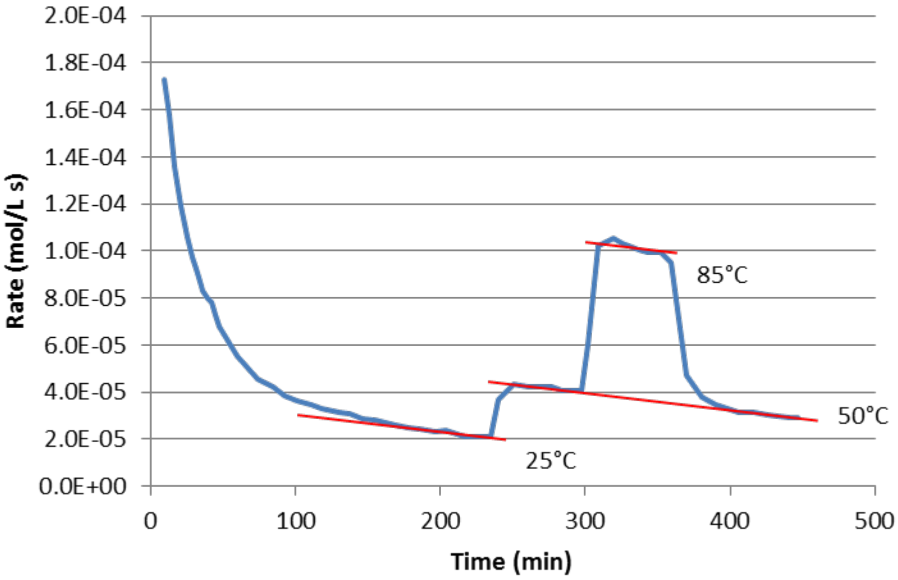

Figure 6.7. Rate of cyclohexene deactivation as the reaction temperature was varied. The three parallel red lines illustrate the rate of catalyst deactivation and show that temperature has no effect on reaction rate during kinetically limited operation.

6.3.2. Analysis of Spent Catalyst

Pulsed chemisorption of carbon monoxide is an established method for quantifying the number of platinum active sites.[171] In this method, the catalyst is loaded into a microreactor or stainless steel tube under a constant flow of helium carrier gas. A known volume of carbon monoxide diluted in helium is then introduced into the system, before being carried through the reactor. When a metal such as platinum is present, one carbon monoxide molecule can bind to each platinum atom. This uptake of carbon monoxide can be calculated by comparing the unabsorbed carbon monoxide at the detector with the known amount in a single pulse. In the absence of platinum or when carbon monoxide has bound all of the platinum sites, the measured carbon monoxide amount should be constant, since all of the carbon monoxide reaches the detector. A profile is generally observed where less of each subsequent pulse is absorbed until all pulses are the same height. A mass spectrometer was used for this analysis and was very sensitive to carbon monoxide. By summing the number of atoms of carbon monoxide consumed in each pulse, the total number of available platinum sites can be determined. It is assumed that each platinum atom provides 1.2×10^{-19} m^2 of surface area.[172]

Pulse chemisorption is particularly useful for comparing catalyst samples and understanding how the available metal changes after reaction. After deactivation, the catalyst was recovered for chemisorption analysis. The number of active sites in the spent catalyst was compared to the number in fresh catalyst. Figure 6.8 summarizes the results. From the pulsed data, it is immediately clear that the spent catalyst absorbs less carbon monoxide than the fresh catalyst. Assuming a 5% platinum loading, a platinum dispersion of 15.2% and 0.4% can be calculated for the fresh and spent catalyst, respectively. These results suggest that the available catalyst sites

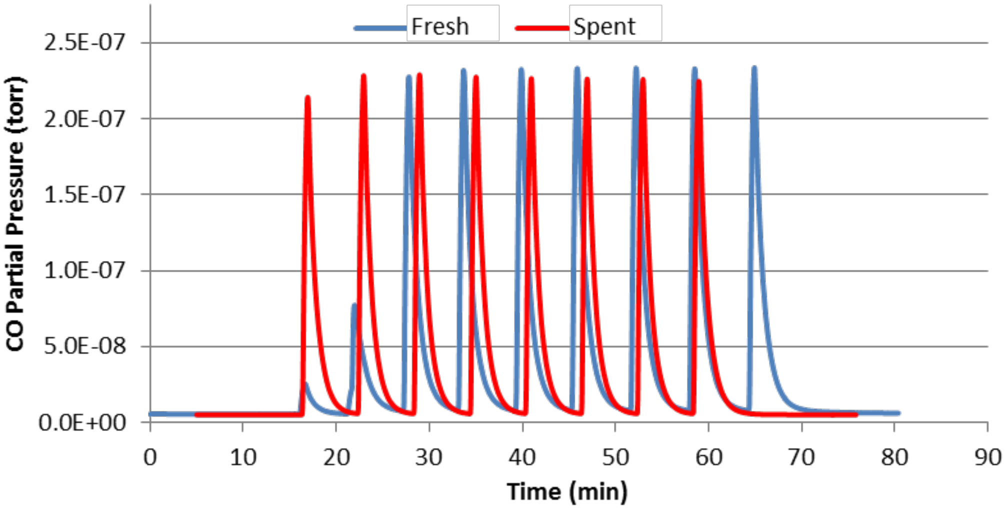

Figure 6.8. Pulse chemisorption results comparing fresh and spent catalyst. The fresh catalyst absorbs significantly more catalyst than the spent catalyst, which is consistent with the observed catalyst deactivation.

decreased 93%. In comparison, the reaction rate decreased by 66% during the experiment. The reduction in available catalyst sites is larger than the reduction in the reaction rate. This comparison is consistent with the fact that not all of the available platinum sites have the same activity, due to differences in morphology. In literature, the chemisorption and reaction of acetylene with Pt(100) and Pt(111) yielded different reactions.[173] Multiple types of platinum sites may explain the difference in reduction of the rate and the number of catalyst deactivation sites.

6.3.3. Discussion of Deactivation Characteristics

A number of deactivation pathways are likely to exist, depending on the nature of the feed. In the presence of hydroperoxides, rapid deactivation occurs through the formation of strong oxygen-platinum bonds. The poisoning of platinum metal due to hydroperoxide contamination is well reported in the literature.[169, 170] This reaction cannot explain all of the observed deactivation since deactivation still occurred after oxygen was excluded from the system. The presence of carbonaceous overlayers have been reported during hydrogenation of both cyclohexene and linear olefins.[174] Even in the presence of excess hydrogen, these dehydrogenated carbonaceous species are strongly held and unreactive. A weakly bound layer of intermediates turns over allowing reaction to proceed. The overlayer also coincides with the restructuring of the metal layer. Either the restructuring or the overlayer itself could explain the observed reduction in catalytic activity.

A related surface reaction study of gas-phase cyclohexene hydrogenation and dehydrogenation over platinum on silica catalyst has been reported in the literature.[175] The study identifies three temperature regions where only hydrogenation, only dehydrogenation, or a combination of hydrogenation dehydrogenation occurs. Specifically, at temperatures below 423 K, only hydrogenation is expected while at temperatures above 573 K, only dehydrogenation is expected. In all reaction regimes, the system was run with excess hydrogen. In the microreactor system, the operating conditions would suggest that only hydrogenation should be observed. During certain experiments, the mass transfer characteristics were probed by increasing the reaction temperature. The reproducibility of data in the kinetic regime was impacted by operation in a hydrogen starved regime. A step change in activity was observed after operation in the mass transfer regime (Figure 6.9). While the reaction rate decreased significantly, the response of reaction rate to temperature remained comparable. This data suggest that dehydrogenation and/or polymerization could occur in the absence of hydrogen at lower temperature than is reported in the literature.

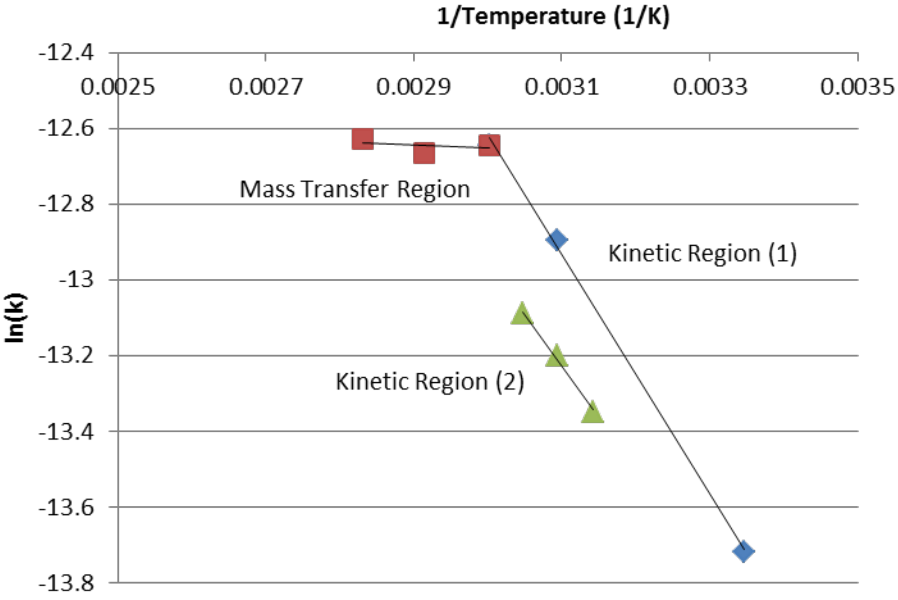

Figure 6.9. A kinetic study (in the order: ♦, ■, ▲) was performed. Significant deactivation occurred while operating in the mass transfer control region. While the reaction rate had decreased, the slope was similar for both kinetic regions.

Differences in reactivity of the support may account for the different rates of deactivation observed between the alumina and silica supports. Alumina, with its acidic sites, is a known cracking catalyst in its own right.[176] Once cracked, cyclohexene resembles any other straight chain alkene and could proceed through similar deactivation pathways as 1-octene.

6.4. Kinetic and Mass Transfer Analysis

Both kinetic and mass transfer analyses were performed in the heterogeneous microreactor system. Numerous studies of the kinetics of cyclohexene hydrogenation have been reported in the literature.[169, 170] Madon et al. propose a rate expression for the hydrogenation of cyclohexene that is 1st order in hydrogen concentration or pressure and 0th order in cyclohexene, at reasonable concentrations of cyclohexene.[169] Specifically, this implies that the rate determining step is the dissociation of a hydrogen molecule on the catalyst surface. They found no dependence on the concentration of cyclohexene. This kinetic relationship greatly simplifies analysis by allowing the rate to be directly calculated from the final conversion without considering the change in cyclohexene concentration. Thus the rate can be calculated,

$$r = {XC_{A0}}/{\tau} \qquad \textbf{(6-1)}$$

where X is the conversion, C_{A0} is the initial concentration of cyclohexene, and τ is the residence time.

While catalyst deactivation proved to be challenging, kinetic data could be collected rapidly, reducing the effect of changes in activity. A standard set of conditions were employed for the hydrogenation studies. The system pressure was maintained at 30 bar. The hydrogen flow rate was set to 80 µl/min, while neat cyclohexene flowed at 20 µl/min. The temperature was then varied, increasing the reaction rate. After crossing a critical reaction rate, the system transitioned from kinetic control to mass transfer control. This transition is shown in Figure 6.9 for cyclohexene hydrogenation over platinum on alumina catalyst. At this stage, further increasing the temperature had little effect on the observed reaction rate. For the first sweep of the kinetically controlled region, an activation energy of E_a = 6.3 kcal/mol was calculated. An activation energy of E_a = 5.4 kcal/mol was calculated for the second sweep. Both results are in reasonable agreement with the literature values of 6.0 ± 0.5 kcal/mol.[169] This estimate would likely be improved with more data points.

A similar analysis was performed for cyclohexene hydrogenation over platinum on silica catalyst. As previously discussed, this catalyst was less susceptible to deactivation making it possible to collect more data points. Figure 6.10 shows an Arrhenius plot for hydrogenation over platinum on silica. The data contain a number of repeats that are indistinguishable from each other. The activation energy calculated from the kinetically controlled region is E_a = 5.2 kcal/mol. This activation energy is comparable to the platinum on alumina results.

It proved easier to estimate the mass transfer rate. As long as the reaction rate was greater than the mass transfer rate, a constant mass transfer rate was observed for a given set of conditions. Depending on the activity of the catalyst, the temperature required to observe mass transfer limitations varied. For example, cyclohexene hydrogenation was studied on two separate days at the same conditions: gas flow rate = 80 µl/min, liquid flow rate = 20 µl/min, pressure = 30 bar. While the activity of the catalyst varied, the maximum mass transfer rate was constant. On April 23, the catalyst reached the mass transfer limiting reaction rate at 60 °C, while on April 21 the temperature had to be at least 70 °C for the rate of reaction to be mass transfer limited.

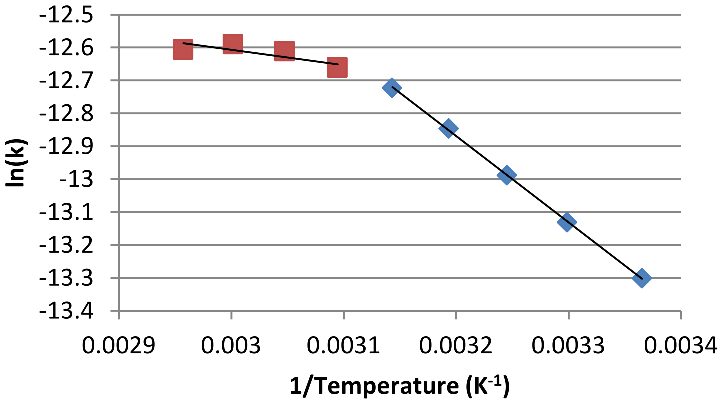

Figure 6.10. Kinetic (♦) and mass transfer (■) limited data for the hydrogenation of cyclohexene over platinum on silica catalyst. The kinetically controlled data corresponds to E_a = 5.2 kcal/mol.

The mass transfer coefficient $k_L a$ can be estimated from the reaction rate at mass transfer controlled conditions. From a closure of mass balance, the rate of mass transfer in the system can be described as follows,

$$r = k_L a\left(C_H^* - C_H\right) \tag{6-2}$$

where r is the reaction rate, C_H is the concentration of hydrogen at the reaction site and C_H^* is the equilibrium concentration, described by Henry's Law. Under mass transfer limitations, C_H is zero.

The mass transfer coefficients calculated for the two cyclohexene experiments in Figure 6.11 as well as for 1-octene are shown in Table 6.3. It was possible to determine a mass transfer rate

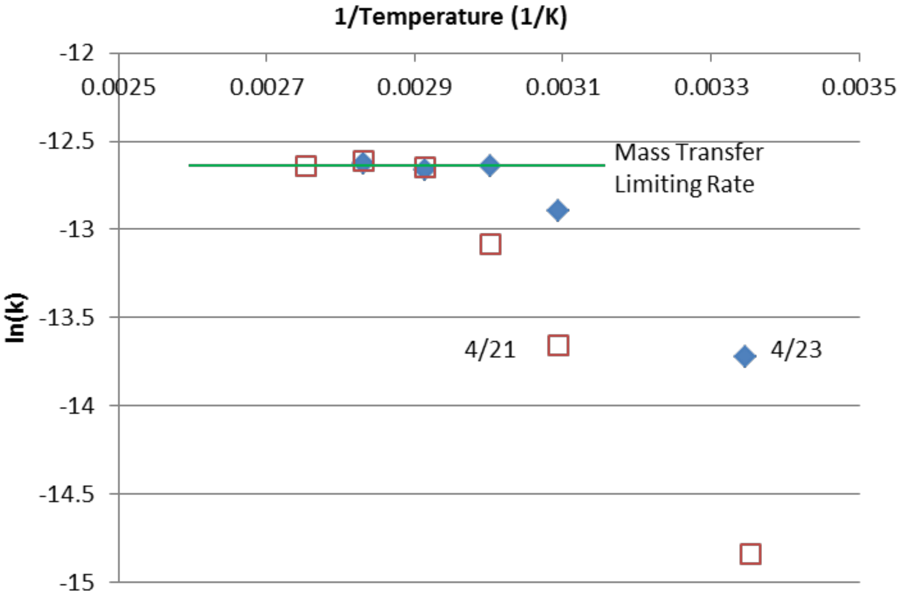

Figure 6.11. Comparison of two days of experiments at the same conditions. The mass transfer limit occurred at the same absolute rate on both days even though the activity of the catalyst varied.

Alkene	**$k_L a$ (s^{-1})**
Cyclohexene	1.7
Cyclohexene	1.8
1-Octene	2.3

Table 6.3. Mass transfer coefficients for cyclohexene and 1-octene hydrogenation over platinum on alumina catalyst.

for 1-octene in spite of rapid deactivation. The calculated mass transfer coefficients ($k_L a$) are approximately 2 sec^{-1}, which are two orders of magnitude higher than in traditional reactor systems.[18] This mass transfer rate is on the same order as those previously observed in low-pressure multiphase reactors.[120] Variations in the hydrogen diffusion coefficient are a possible explanation for the differences in the calculated mass transfer coefficients observed during cyclohexene and 1-octene hydrogenation. A number of mass transfer models exist that provide insight into the relationship between the mass transfer and diffusion coefficients.[177] Film theory provides one such relationship, suggesting that the mass transfer coefficient is proportional to the diffusion coefficient D. Penetration theory, a second mass transfer model, concludes that the mass transfer coefficient is proportional to $D^{0.5}$. Together, these two theories provide bounds for the exponents of the diffusion coefficient in empirical mass transfer coefficient expressions. The ratio of diffusivities under both mass transfer models are shown in Table 6.4. After comparing the ratio of the mass transfer coefficients to the ratio of diffusivities, it was concluded that the observed differences in the mass transfer rate are consistent with the variations in the diffusivities of hydrogen in the cyclohexene and 1-octene.

An alternate way to observe the effect of mass transfer limitations is to vary the flow rate of hydrogen at constant temperature (50 °C) and liquid flow rate (20 µl/min). The mass transfer

	$k_L a$ (s^{-1})	$D \cdot 10^5$ cm^2/s	$D^{0.5}$
1-Octene	2.3	45	0.021
Cyclohexene	1.75	22	0.015
Ratio	**1.4**	**2.0**	**1.4**

Table 6.4. Differences in the diffusivity of hydrogen in the two solvents[178] are consistent with the variation in the measured mass transfer rates.

rate increases with gas flow rate due to a thinning of the liquid boundary layer coating the catalyst particles. As this layer thins, the mass transfer resistance in the layer is also reduced. At low gas flow rates, Figure 6.12 shows that the reaction rate improves as the gas flow rate is increased. These conditions correspond to mass transfer control. At a critical gas flow rate, increases in this flow rate no longer increase the reaction rate. At these conditions, the reaction is kinetically controlled. If the reaction rate depended on the combined gas-liquid residence time, the observed reaction rate would peak. At low gas flow rates, increasing the flow rate would overcome mass transfer limitations, increasing the reaction rate. At high gas flow rates, increasing the flow rate would instead reduce the residence time, decreasing the reaction rate. The absence of this effect suggests that the gas flow rate does not affect the liquid residence time. Instead, the hydrogenation rate is controlled solely by the liquid residence time.

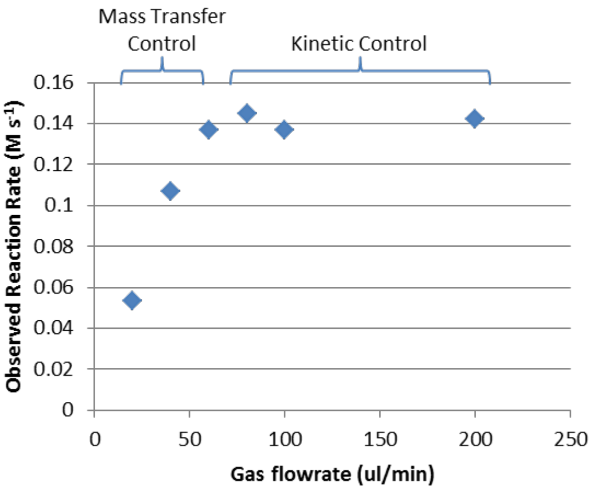

Figure 6.12. At constant temperature (50 °C) and cyclohexene flow rate (20 µl/min), the flow rate of hydrogen was varied allowing the reaction rate to transition from mass transfer control to kinetic control.

Chapter 7. Conclusion

7.1. Accomplishments

The primary accomplishment of this thesis was the development of a high-pressure, continuous flow microreactor system. This system enables studying of both homogenous and heterogeneous gas-liquid catalyst systems. This system increases the pressure and flow rate envelope that can be studied in microreactor systems to include conditions that are typical of commercial operation. Conducting kinetic research at these conditions reduces the time and cost of turning laboratory results into commercially viable processes. Specifically, precise temperature control facilitated studying conditions for 25-350 °C. It is able to operate at pressures ranging from near atmospheric to 100 bar. The system is particularly well suited to study the temperature dependence of reactions. The small reactor scale allows for rapid temperature change and up to three temperatures can be sampled in the span of an hour, which represents a substantial improvement over traditional batch systems, in the absence of parallelization.

Significant design challenges were overcome to enable the study of high-pressure reactions at the low flow rates required for microliter scale reactors. The system was constructed in a completely modular manner allowing for the addition of process components without altering its major systems. For example, when it was determined that combined gas-liquid streams led to analytic performance deterioration, a membrane separator was introduced to the system without disturbing the pressure-control and flow-delivery systems. From the design through the operating stage, reproducibility was a critical goal for the system. These goals were manifested through careful design of the temperature control system to enable computer-based control. Computer based automation and control were employed to remove variability associated with manual manipulation.

Two complementary analytic systems were demonstrated in the high-pressure system. Online Fourier transform infrared (FTIR) analysis was demonstrated to provide important real time information on system operation and enabled quantitative analysis of simple chemical mixtures, such as the cyclohexene/cyclohexane samples from the heterogeneous hydrogenation. Experimental throughput was improved by monitoring for steady state in real-time. Offline analysis, specifically gas chromatography (GC), provided highly reproducible quantitative analysis for the considered reaction systems. GC analysis is much more sensitive than IR at low analyte concentrations, widening the possible reaction conditions.

Both homogeneous and heterogeneous catalyst systems were studied. Each system required a different silicon microreactor, which was designed, fabricated, and demonstrated under flow conditions. Residence times ranging from seconds to approximately 15 minutes were observed in the homogenous reactor. The internal volume of the heterogeneous reactor was far smaller than the homogeneous reactor, resulting in residence times of up to a minute.

The hydroformylation of 1-octene was chosen to demonstrate the performance of the homogeneous system. This reaction involves the addition of a hydrogen and a carbon monoxide molecule to 1-octene with a $HRh(CO)(PPh_3)_3$ catalyst. The empirical reaction order for the dependence on catalyst, hydrogen, and carbon monoxide were determined from these experiments. The overall reaction was determined to be nearly first order in catalyst and hydrogen concentrations and inversely proportional to carbon monoxide concentration. These results were reconciled against the mechanism reported in the literature. Hydrogenolysis was observed to be the rate determining step and the inverse dependence on carbon monoxide was explained by an additional coordination of carbon monoxide to a catalyst intermediate, removing it from the cycle. Through this analysis, a rate expression was proposed which included temperature dependent terms. An activation energy of E_a = 19.2 kcal/mol and pre-exponential factor of $\ln(A_0)$ = 25.2 were determined through this analysis. The observed activation energy compares favorably with the literature for similar olefins.[136, 137]

The hydrogenation of cyclohexene to cyclohexane over platinum catalysts was chosen to demonstrate the performance of the heterogeneous reactor. The reaction was demonstrated over two catalysts, 5% platinum on alumina and 5% platinum on silica. Upon overcoming deactivation issues, an activation energy E_a = 5-6 kcal/mol was observed for both catalysts. Additionally, the reaction proceeds so rapidly that mass transfer limitation is observed even in microreactors. This limit enabled characterization of the gas-liquid mass transfer coefficient in the system. The mass transfer coefficient was shown to vary depending on substrate, which is related to the diffusivity of hydrogen in cyclohexene and 1-octene. The observed mass transfer coefficient (k_La) was approximately 2 s^{-1}, which is consistent with microreactor results at low pressure[120] and 100 times higher than in traditional systems.[18]

The system, as demonstrated, increases the range of conditions that can be studied in microreactors. These advancements allow for higher pressure and temperature experimentation than was previously possible in the laboratory.

7.2. Challenges and Recommendations

While the system is operational and providing reliable data, a number of challenges remain. It is not possible to operate the system at its design pressure when the IR system is attached. Additionally, segmented flow stability remains challenging and coalescence is unavoidable at long residence times. Finally, hour long residence times are unachievable in the current system.

When real time analysis is enabled, the system must operate at pressures below 30 bar, rather than the design pressure of 100 bar. Real time analysis provides significant additional information, making it advantageous to include some form of real time analysis. IR provides inline analysis in the current system through the integration of a flow cell. This flow cell was recently developed by Mettler Toledo and represents the state of the art in the commercial IR industry. To operate at pressures higher than 30 bar, the system was analyzed using offline analysis, which is available at any pressure. This offline nature requires that a set of experiments be performed without the benefit of early problem identification. The inability to observe steady state in real time also reduces throughput. One possible approach to overcome the pressure limitations inherent to the commercial flow cell is to directly integrate spectroscopic analysis into the microreactor. This has been previously demonstrated for low pressure applications.[67] The designs could be extended for high-pressure operation. A second option could be to use the offline sampling system to integrate a high-pressure liquid chromatography (HPLC). While this system would not provide in situ characterization, it is capable of returning a result prior to a set point change. In addition, these samples could be taken more quickly since an online HPLC system would require a smaller sample than vial sample collection.

Bubble coalescence proved to be an ongoing challenge in the long channel of the homogeneous reactor. Careful pressure control through the strategic use of pressure reduction improved the flow. To enable completely stable segmented flow, all pressure fluctuations must be removed throughout the system. One of the greatest strengths of the high-pressure system, its ability to decouple flow rate from operating pressure, is provided by the back pressure controller. This system operates by controlling the position of the valve to maintain a constant pressure in the controller. This valve is constantly vibrating as gas and liquid leave the pressurized system. It is likely that these fluctuations compound to lead to unstable flow in the system given enough residence time. In addition, gas in the bubbles is consumed during reaction, altering the size of the gas bubble and further impacting stability. Most methods for improving flow stability involve careful manipulation of pressure drops within the system. The simplest method for increasing pressure drop is to add a length of small diameter tubing. Small diameter tubing is also preferable because it reduces system volume for a given pressure drop. In practice, small tube diameters present a clogging risk in the presence of solid particles such as heterogeneous catalysts. Control of the pressure within the system remains an ongoing challenge.

The final challenge is enabling the study of slow reactions in microreactors. For example, many of the reactions that are of interest in pyrolysis oil upgrading require reaction times of greater than an hour. A number of design decisions limit the longest residence times available in the high-pressure system. For high-pressure conditions to be feasible, the width of a channel is limited to approximately 400 µm. A reasonably sized microreactor, of which a few could be fabricated on a single 6” silicon wafer, would have a maximum internal volume on the order of 250 µl. Slow reactions requiring residence times of one hour would thus require delivering total flow rates of 4 µl/min. It is possible to design larger microreactors, using wider channels, but the upper pressure limit of the system would then be reduced accordingly. There are very few products commercially available that enable both the precise control of slow flow rates as well as operation at high pressure. The high-pressure syringe pumps employed in this work are capable of driving flow at liquid flow rates of 1 µl/min, around the flow rates that would be required for studying reactions at long residence times. Unfortunately, it estimated that a typical leak rate in the system under pressure is approximately 1 µl/min, which would represent a significant percentage of the total flow.

The external system ultimately determines what flow rates are practical. Ideally, the residence time in the analytic components would be much smaller than the reactor residence time. In practice, the volume of the downstream components can rival the volume of the reactor. Between samples, a minimum of three residence times are required to ensure the system is sampling the new steady state. For slow reactions with a residence time of 60 min, it would take hours to collect a single data point. This residence time requirement is particularly important given the large cavity in the micro flow cell. This geometry is particularly susceptible to mixing due to axial dispersion. Bringing the chemical analysis on chip would increase the feasibility of long residence times.

7.3. Outlook

Microreactors systems, such as the one described in this thesis, are powerful tools for studying chemical reactions. They are most powerful when paired with an appropriate chemical reaction. Ideal chemical systems should take advantage of at least one of the three microreactor benefits: high heat transfer, high mass transfer, and low material amounts. For high heat and mass transfer to be required, the reaction must be fast. For purposes of this system, fast reactions can be defined as those with measurable conversions achieved on the order of seconds to minutes. Any traditional system is capable of overcoming mass transfer limitations for reactions that take hours to complete.

Analysis systems strive to be accurate and efficient. The hydroformylation and hydrogenation examples demonstrate that the system described in this thesis is accurate. For the system to be efficient, the number of experiments completed in a given time period must be maximized. This time can be split into experimental time and setup time. Continuous operation minimizes the effect of setup time by spreading it across a large number of experiments. The current continuous system is very efficient at studying reaction temperature dependence. Batch systems, on the other hand, are very efficient at time dependent characterization of a reaction and are easier to parallelize. The longer the desired reaction, the smaller the impact that setup time has on the overall efficiency. For maximum efficiency, it is critical to pair each chemical system with an appropriate analysis technique for the type of information desired.

The high-pressure system described in this work might still be well suited to study traditionally slower reactions. Operating at high-pressure and temperature can enable measurable conversion to be achieved more quickly than under traditional conditions, offsetting low residence times. The system is also primed to study systems where the catalyst is scarce. Today, significant research is being devoted to nanoparticle catalysts. It is often not practical to synthesize the large quantities of these materials required to enable characterization in traditional reaction systems. Microreactors may therefore prove to be the only realistic reaction platform for kinetic and mechanistic study. Improved analytic systems would only improve the feasibility for studying such catalysts in high-pressure microreactor systems. When microreactor technology is properly leveraged, significant accuracy and throughput improvements can be realized.

References

1. Bell, A.T., B.C. Gates, D. Ray and M.R. Thompson, *Basic Research Needs: Catalysis for Energy*. 2008, Pacific Northwest National Laboratory (PNNL), Richland, WA (US).

2. United States Central Inteligence Agency, *CIA World Factbook 2011: Complete Unabridged Edition*. 2010: MobileReference.

3. (EIA), E.I.A. *Voluntary Reporting of Greenhouse Gases Program*. 2011 [cited 2011 2/18/2011]; Available from: http://www.eia.gov/oiaf/1605/frntvrgg.html.

4. Perlack, R.D., L.L. Wright, A.F. Turhollow, R.L. Graham, B.J. Stokes, D.C. Erbach and O.R.N.L. TN, *Biomass as feedstock for a bioenergy and bioproducts industry: the technical feasibility of a billion-ton annual supply.* 2005.

5. Hagen, J., *Industrial catalysis : a practical approach*. 2nd, completely rev. and extended ed. 2006, Weinheim: Wiley-VCH. xviii, 507 p.

6. Parr, R.G., *Density Functional Theory.* Annual Review of Physical Chemistry, 1983. **34**: p. 631-656.

7. Norskov, J.K., T. Bligaard, J. Rossmeisl and C.H. Christensen, *Towards the computational design of solid catalysts.* Nat Chem, 2009. **1**(1): p. 37-46.

8. Hagemeyer, A., B. Jandeleit, Y.M. Liu, D.M. Poojary, H.W. Turner, A.F. Volpe and W.H. Weinberg, *Applications of combinatorial methods in catalysis.* Applied Catalysis a-General, 2001. **221**(1-2): p. 23-43.

9. Murphy, V., X.H. Bei, T.R. Boussie, O. Brummer, G.M. Diamond, C. Goh, K.A. Hall, A.M. Lapointe, M. Leclerc, J.M. Longmire, J.A.W. Shoemaker, H. Turner and W.H. Weinberg, *High-throughput approaches for the discovery and optimization of new olefin polymerization catalysts.* Chemical Record, 2002. **2**(4): p. 278-289.

10. Hoogenboom, R., M.A.R. Meier and U.S. Schubert, *Combinatorial methods, automated synthesis and high-throughput screening in polymer research: Past and present.* Macromolecular Rapid Communications, 2003. **24**(1): p. 16-32.

11. Reetz, M.T., *Combinatorial and evolution-based methods in the creation of enantioselective catalysts.* Angewandte Chemie-International Edition, 2001. **40**(2): p. 284-310.

12. Espenson, J.H., *Chemical kinetics and reaction mechanisms*. McGraw-Hill series in advanced chemistry. 1981, New York: McGraw-Hill. x, 218 p.

13. Snelgrove, D.W., J. Lusztyk, J.T. Banks, P. Mulder and K.U. Ingold, *Kinetic solvent effects on hydrogen-atom abstractions: Reliable, quantitative predictions via a single empirical equation.* Journal of the American Chemical Society, 2001. **123**(3): p. 469-477.

14. Amatore, C. and A. Jutand, *Mechanistic and kinetic studies of palladium catalytic systems.* Journal of Organometallic Chemistry, 1999. **576**(1-2): p. 254-278.

15. Grabow, L.C., A.A. Gokhale, S.T. Evans, J.A. Dumesic and M. Mavrikakis, *Mechanism of the water gas shift reaction on Pt: First principles, experiments, and microkinetic modeling.* Journal of Physical Chemistry C, 2008. **112**(12): p. 4608-4617.

16. Moulijn, J.A., P.W.N.M.v. Leeuwen and R.A.v. Santen, *Catalysis : an integrated approach to homogeneous, heterogeneous and industrial catalysis*. Studies in surface science and catalysis 79. 1993, Amsterdam ; New York: Elsevier. xviii, 460 p.

17. Montgomery, D.C., *Design and analysis of experiments*. 4th ed. 1997, New York: Wiley. xiii, 704 p.

18. Al-Dahhan, M.H., F. Larachi, M.P. Dudukovic and A. Laurent, *High-Pressure Trickle-Bed Reactors: A Review.* Industrial & Engineering Chemistry Research, 1997. **36**(8): p. 3292-3314.

19. Jessop, P.G., Y. Hsiao, T. Ikariya and R. Noyori, *Homogeneous catalysis in supercritical fluids: Hydrogenation of supercritical carbon dioxide to formic acid, alkyl formates, and formamides.* Journal of the American Chemical Society, 1996. **118**(2): p. 344-355.

20. Burcham, L.J., M. Badlani and I.E. Wachs, *The Origin of the Ligand Effect in Metal Oxide Catalysts: Novel Fixed-Bed in Situ Infrared and Kinetic Studies during Methanol Oxidation.* Journal of Catalysis, 2001. **203**(1): p. 104-121.

21. Hagemeyer, A., R. Borade, P. Desrosiers, S. Guan, D.M. Lowe, D.M. Poojary, H. Turner, H. Weinberg, X. Zhou, R. Armbrust, G. Fengler and U. Notheis, *Application of combinatorial catalysis for the direct amination of benzene to aniline.* Applied Catalysis A: General, 2002. **227**(1-2): p. 43-61.

22. Symyx. *Heterogeneous Catalysis*. [cited 2011 Feb 25]; Available from: http://www.symyx.com/products/pdfs/Heterogeneous%20Catalysis%20Overview%20Brochure.pdf.

23. ThalesNano. *X-Cube - Catalysis Made Simple*. [cited 2011 Feb 25]; Available from: http://www.thalesnano.com/products/x-cube.

24. HEL. *High Pressure Chemistry: Hydrogenation & Catalysis Tools*. [cited 2011 Feb 25]; Available from: http://www.helgroup.com/pdf/hydrogenation-catalysis/Hydrogenation_Catalysis_HEL_LR.pdf.

25. Manz, A., J.C. Fettinger, E. Verpoorte, H. Ludi, H.M. Widmer and D.J. Harrison, *Micromachining of monocrystalline silicon and glass for chemical analysis systems - A look into next century's technology or just a fashionable craze?* Trac-Trends in Analytical Chemistry, 1991. **10**(5): p. 144-149.

26. Jensen, K.F., *Microchemical systems: Status, challenges, and opportunities.* Aiche Journal, 1999. **45**(10): p. 2051-2054.

27. Ratner, D.M., E.R. Murphy, M. Jhunjhunwala, D.A. Snyder, K.F. Jensen and P.H. Seeberger, *Microreactor-based reaction optimization in organic chemistry glycosylation as a challenge.* Chemical Communications, 2005(5): p. 578-580.

28. Madou, M.J., *Fundamentals of microfabrication : the science of miniaturization*. 2nd ed. 2002, Boca Raton, Fla.: CRC Press. 723 p., [16] p. of plates.

29. Whitesides, G.M., *The origins and the future of microfluidics.* Nature, 2006. **442**(7101): p. 368-373.

30. Whitesides, G.M., E. Ostuni, S. Takayama, X.Y. Jiang and D.E. Ingber, *Soft lithography in biology and biochemistry.* Annual Review of Biomedical Engineering, 2001. **3**: p. 335-373.

31. Whitesides, G.M. and A.D. Stroock, *Flexible methods for microfluidics.* Physics Today, 2001. **54**(6): p. 42-48.

32. Qu, H.Y., H.T. Wang, Y. Huang, W. Zhong, H.J. Lu, J.L. Kong, P.Y. Yang and B.H. Liu, *Stable microstructured network for protein patterning on a plastic microfluidic channel: Strategy and characterization of on-chip enzyme microreactors.* Analytical Chemistry, 2004. **76**(21): p. 6426-6433.

33. Zhao, Y.C., G.W. Chen and Q. Yuan, *Liquid-liquid two-phase flow patterns in a rectangular microchannel.* Aiche Journal, 2006. **52**(12): p. 4052-4060.

34. Greenway, G.M., S.J. Haswell, D.O. Morgan, V. Skelton and P. Styring, *The use of a novel microreactor for high throughput continuous flow organic synthesis.* Sensors and Actuators B-Chemical, 2000. **63**(3): p. 153-158.

35. Jensen, K.F., *Silicon-based microchemical systems: Characteristics and applications.* Mrs Bulletin, 2006. **31**(2): p. 101-107.

36. Hessel, V., H. Lowe and T. Stange, *Micro chemical processing at IMM - from pioneering work to customer-specific services.* Lab on a Chip, 2002. **2**(1): p. 14N-21N.

37. Meschke, F., G. Riebler, V. Hessel, J. Schurer and T. Baier, *Hermetic gas-tight ceramic microreactors.* Chemical Engineering & Technology, 2005. **28**(4): p. 465-473.

38. Bejan, A., A.D. Kraus and Knovel (Firm). *Heat transfer handbook*. 2003; xiv, 1480 p.]. Available from: http://www.knovel.com/knovel2/Toc.jsp?BookID=725 MIT Access Only.

39. Ho, C.M. and Y.C. Tai, *Micro-electro-mechanical-systems (MEMS) and fluid flows.* Annual Review of Fluid Mechanics, 1998. **30**: p. 579-612.

40. Kovacs, G.T.A., K. Petersen and M. Albin, *Peer Reviewed: Silicon Micromachining: Sensors to Systems.* Analytical Chemistry, 1996. **68**(13): p. 407A-412A.

41. Laermer, F. and A. Schilp, *Methods for anisotropic etching of silicon*. 1994. p. 6 pp.

42. Murphy, E.R., J.R. Martinelli, N. Zaborenko, S.L. Buchwald and K.F. Jensen, *Accelerating reactions with microreactors at elevated temperatures and pressures: Profiling aminocarbonylation reactions.* Angewandte Chemie-International Edition, 2007. **46**(10): p. 1734-1737.

43. Jensen, K.F., *Microreaction engineering - is small better?* Chemical Engineering Science, 2001. **56**(2): p. 293-303.

44. Nguyen, N.T. and Z.G. Wu, *Micromixers - a review.* Journal of Micromechanics and Microengineering, 2005. **15**(2): p. R1-R16.

45. Hessel, V., S. Hardt, H. Lowe and F. Schonfeld, *Laminar mixing in different interdigital micromixers: I. Experimental characterization.* Aiche Journal, 2003. **49**(3): p. 566-577.

46. Lob, P., K.S. Drese, V. Hessel, S. Hardt, C. Hofmann, H. Lowe, R. Schenk, F. Schonfeld and B. Werner, *Steering of liquid mixing speed in interdigital micro mixers - from very fast to deliberately slow mixing.* Chemical Engineering & Technology, 2004. **27**(3): p. 340-345.

47. Hessel, V., H. Lowe and F. Schonfeld, *Micromixers - a review on passive and active mixing principles.* Chemical Engineering Science, 2005. **60**(8-9): p. 2479-2501.

48. Burns, J.R. and C. Ramshaw, *The intensification of rapid reactions in multiphase systems using slug flow in capillaries.* Lab on a Chip, 2001. **1**(1): p. 10-15.

49. Gunther, A., M. Jhunjhunwala, M. Thalmann, M.A. Schmidt and K.F. Jensen, *Micromixing of miscible liquids in segmented gas-liquid flow.* Langmuir, 2005. **21**(4): p. 1547-1555.

50. Gunther, A., S.A. Khan, M. Thalmann, F. Trachsel and K.F. Jensen, *Transport and reaction in microscale segmented gas-liquid flow.* Lab on a Chip, 2004. **4**: p. 278-286.

51. Trachsel, F., A. Gunther, S. Khan and K.F. Jensen, *Measurement of residence time distribution in microfluidic systems.* Chemical Engineering Science, 2005. **60**: p. 5729-5737.

52. Marre, S., A. Adamo, S. Basak, C. Aymonier and K.F. Jensen, *Design and Packaging of Microreactors for High Pressure and High Temperature Applications.* Industrial & Engineering Chemistry Research, 2010. **49**(22): p. 11310-11320.

53. Marre, S., J. Baek, J. Park, M.G. Bawendi and K.F. Jensen, *High-Pressure/High-Temperature Microreactors for Nanostructure Synthesis.* Jala, 2009. **14**(6): p. 367-373.

54. Marre, S., J. Park, J. Rempel, J. Guan, M.G. Bawendi and K.F. Jensen, *Supercritical Continuous-Microflow Synthesis of Narrow Size Distribution Quantum Dots.* Advanced Materials, 2008. **20**(24): p. 4830-+.

55. Murphy, E.R., T. Inoue, H.R. Sahoo, N. Zaborenko and K.F. Jensen, *Solder-based chip-to-tube and chip-to-chip packaging for microfluidic devices.* Lab on a Chip, 2007. **7**: p. 1309-1314.

56. Ajmera, S.K., M.W. Losey, K.F. Jensen and M.A. Schmidt, *Microfabricated packed-bed reactor for phosgene synthesis.* Aiche Journal, 2001. **47**(7): p. 1639-1647.

57. de Mas, N., A. Gunther, M.A. Schmidt and K.F. Jensen, *Microfabricated multiphase reactors for the selective direct fluorination of aromatics.* Industrial & Engineering Chemistry Research, 2003. **42**(4): p. 698-710.

58. de Mas, N., A. Gunther, M.A. Schmidt and K.F. Jensen, *Increasing Productivity of Microreactors for Fast Gas-Liquid Reactions: The Case of Direct Fluorination of Toluene.* Industrial & Engineering Chemistry Research, 2009. **48**(3): p. 1428-1434.

59. Zaborenko, N., E.R. Murphy, J.G. Kralj and K.F. Jensen, *Synthesis and Kinetics of Highly Energetic Intermediates by Micromixers: Direct Multistep Synthesis of Sodium Nitrotetrazolate.* Industrial & Engineering Chemistry Research, 2010. **49**(9): p. 4132-4139.

60. Arana, L.R., S.B. Schaevitz, A.J. Franz, M.A. Schmidt and K.F. Jensen, *A microfabricated suspended-tube chemical reactor for thermally efficient fuel processing.* Journal of Microelectromechanical Systems, 2003. **12**(5): p. 600-612.

61. Blackwell, B.S., *Design, fabrication, and characterization of a micro fuel processor*, in *Massachusetts Institute of Technology. Dept. of Chemical Engineering.* 2007. p. 174 p.

62. Bermel, P., M. Ghebrebrhan, W. Chan, Y.X. Yeng, M. Araghchini, R. Hamam, C.H. Marton, K.F. Jensen, M. Soljacic, J.D. Joannopoulos, S.G. Johnson and I. Celanovic, *Design and global optimization of high-efficiency thermophotovoltaic systems.* Optics Express, 2010. **18**(19): p. A314-A334.

63. El-Ali, J., P.K. Sorger and K.F. Jensen, *Cells on chips.* Nature, 2006. **442**(7101): p. 403-411.

64. Sanders, G.H.W. and A. Manz, *Chip-based microsystems for genomic and proteomic analysis.* Trac-Trends in Analytical Chemistry, 2000. **19**(6): p. 364-378.

65. Watts, P. and S.J. Haswell, *Microfluidic combinatorial chemistry.* Current Opinion in Chemical Biology, 2003. **7**(3): p. 380-387.

66. Ajmera, S.K., C. Delattre, M.A. Schmidt and K.F. Jensen, *Microfabricated differential reactor for heterogeneous gas phase catalyst testing.* Journal of Catalysis, 2002. **209**(2): p. 401-412.

67. Floyd, T.M., M.A. Schmidt and K.F. Jensen, *Silicon micromixers with infrared detection for studies of liquid-phase reactions.* Industrial & Engineering Chemistry Research, 2005. **44**(8): p. 2351-2358.

68. Kerby, M.B., R.S. Legge and A. Tripathi, *Measurements of kinetic parameters in a microfluidic reactor.* Analytical Chemistry, 2006. **78**(24): p. 8273-8280.

69. Gustafsson, T., F. Ponten and P.H. Seeberger, *Trimethylaluminium mediated amide bond formation in a continuous flow microreactor as key to the synthesis of rimonabant and efaproxiral.* Chemical Communications, 2008(9): p. 1100-1102.

70. Jensen, K.F. and P.H. Seeberger, *Microreactors for synthesis and reaction optimisation.* Nachrichten Aus Der Chemie, 2005. **53**(6): p. 628-632.

71. McMullen, J.P. and K.F. Jensen, *An Automated Microfluidic System for Online Optimization in Chemical Synthesis.* Organic Process Research & Development, 2010. **14**(5): p. 1169-1176.

72. Kreutz, J.E., A. Shukhaev, W.B. Du, S. Druskin, O. Daugulis and R.F. Ismagilov, *Evolution of Catalysts Directed by Genetic Algorithms in a Plug-Based Microfluidic Device Tested with Oxidation of Methane by Oxygen.* Journal of the American Chemical Society, 2010. **132**(9): p. 3128-3132.

73. Li, L., D. Mustafi, Q. Fu, V. Tereshko, D.L.L. Chen, J.D. Tice and R.F. Ismagilov, *Nanoliter microfluidic hybrid method for simultaneous screening and optimization validated with crystallization of membrane proteins.* Proceedings of the National Academy of Sciences of the United States of America, 2006. **103**(51): p. 19243-19248.

74. Sahoo, H.R., J.G. Kralj and K.F. Jensen, *Multistep continuous-flow microchemical synthesis involving multiple reactions and separations.* Angewandte Chemie-International Edition, 2007. **46**(30): p. 5704-5708.

75. Hartman, R.L., H.R. Sahoo, B.C. Yen and K.F. Jensen, *Distillation in microchemical systems using capillary forces and segmented flow.* Lab on a Chip, 2009. **9**(13): p. 1843-1849.

76. Zheng, B., C.J. Gerdts and R.F. Ismagilov, *Using nanoliter plugs in microfluidics to facilitate and understand protein crystallization.* Current Opinion in Structural Biology, 2005. **15**(5): p. 548-555.

77. Albrecht, J.W., J. El-Ali and K.F. Jensen, *Cascaded free-flow isoelectric focusing for improved focusing speed and resolution.* Analytical Chemistry, 2007. **79**(24): p. 9364-9371.

78. Huang, M.F., Y.C. Kuo, C.C. Huang and H.T. Chang, *Separation of long double-stranded DNA by nanoparticle-filled capillary electrophoresis.* Analytical Chemistry, 2004. **76**(1): p. 192-196.

79. Franz, A.J., K.F. Jensen and M.A. Schmidt, *Palladium based micromembranes for hydrogen separation and hydrogenation/dehydrogenation reactions.* Mems '99: Twelfth Ieee International Conference on Micro Electro Mechanical Systems, Technical Digest, 1999: p. 382-387.

80. Franz, A.J., K.F. Jensen and M.A. Schmidt, *Palladium membrane microreactors.* Microreaction Technology: Industrial Prospects, 2000: p. 267-276.

81. Quiram, D.J., I.M. Hsing, A.J. Franz, K.F. Jensen and M.A. Schmidt, *Design issues for membrane-based, gas phase microchemical systems.* Chemical Engineering Science, 2000. **55**(16): p. 3065-3075.

82. Wilhite, B.A., M.A. Schmidt and K.F. Jensen, *Palladium-based micromembranes for hydrogen separation: Device performance and chemical stability.* Industrial & Engineering Chemistry Research, 2004. **43**(22): p. 7083-7091.

83. Deshpande, K., J.H. Meldon, M.A. Schmidt and K.F. Jensen, *SOI-Supported Microdevice for Hydrogen Purification Using Palladium-Silver Membranes.* Journal of Microelectromechanical Systems, 2010. **19**(2): p. 402-409.

84. Kralj, J.G., H.R. Sahoo and K.F. Jensen, *Integrated continuous microfluidic liquid-liquid extraction.* Lab on a Chip, 2007. **7**(2): p. 256-263.

85. Gunther, A. and K.F. Jensen, *Multiphase microfluidics: from flow characteristics to chemical and materials synthesis.* Lab on a Chip, 2006. **6**(12): p. 1487-1503.

86. Ferstl, W., T. Klahn, W. Schweikert, G. Billeb, M. Schwarzer and S. Loebbecke, *Inline analysis in microreaction technology: A suitable tool for process screening and optimization.* Chemical Engineering & Technology, 2007. **30**(3): p. 370-378.

87. Leung, S.A., R.F. Winkle, R.C.R. Wootton and A.J. deMello, *A method for rapid reaction optimisation in continuous-flow microfluidic reactors using online Raman spectroscopic detection.* Analyst, 2005. **130**(1): p. 46-51.

88. Maguire, Y., I.L. Chuang, S.G. Zhang and N. Gershenfeld, *Ultra-small-sample molecular structure detection using microslot waveguide nuclear spin resonance.* Proceedings of the National Academy of Sciences of the United States of America, 2007. **104**(22): p. 9198-9203.

89. Losey, M.W., R.J. Jackman, S.L. Firebaugh, M.A. Schmidt and K.F. Jensen, *Design and fabrication of microfluidic devices for multiphase mixing and reaction.* Journal of Microelectromechanical Systems, 2002. **11**(6): p. 709-717.

90. Quiram, D.J., K.F. Jensen, M.A. Schmidt, P.L. Mills, J.F. Ryley, M.D. Wetzel and D.J. Kraus, *Integrated microreactor system for gas-phase catalytic reactions. 1. Scale-up microreactor design and fabrication.* Industrial & Engineering Chemistry Research, 2007. **46**(25): p. 8292-8305.

91. Elwenspoek, M., T.S.J. Lammerink, R. Miyake and J.H.J. Fluitman, *Towards Integrated Microliquid Handling Systems.* Journal of Micromechanics and Microengineering, 1994. **4**(4): p. 227-245.

92. Cho, S.T., K. Najafi, C.E. Lowman and K.D. Wise, *An Ultrasensitive Silicon Pressure-Based Microflow Sensor.* Ieee Transactions on Electron Devices, 1992. **39**(4): p. 825-835.

93. Kraus, T., A. Gunther, N. de Mas, M.A. Schmidt and K.F. Jensen, *An integrated multiphase flow sensor for microchannels.* Experiments in Fluids, 2004. **36**(6): p. 819-832.

94. Zhang, X.L., P. Coupland, P.D.I. Fletcher and S.J. Haswell, *Monitoring of liquid flow through microtubes using a micropressure sensor.* Chemical Engineering Research & Design, 2009. **87**(1A): p. 19-24.

95. Roberge, D.M., L. Ducry, N. Bieler, P. Cretton and B. Zimmermann, *Microreactor technology: A revolution for the fine chemical and pharmaceutical industries?* Chemical Engineering & Technology, 2005. **28**(3): p. 318-323.

96. Roberge, D.M., B. Zimmermann, F. Rainone, M. Gottsponer, M. Eyholzer and N. Kockmann, *Microreactor technology and continuous processes in the fine chemical and pharmaceutical industry: Is the revolution underway?* Organic Process Research & Development, 2008. **12**(5): p. 905-910.

97. Stankiewicz, A.I. and J.A. Moulijn, *Process intensification: Transforming chemical engineering.* Chemical Engineering Progress, 2000. **96**(1): p. 22-34.

98. Chaudhari, R.V., A. Seayad and S. Jayasree, *Kinetic modeling of homogeneous catalytic processes.* Catalysis Today, 2001. **66**(2-4): p. 371-380.

99. Bernas, A., P. Maki-Arvela, J. Lehtonen, T. Salmi and D.Y. Murzin, *Kinetic modeling of propene hydroformylation with Rh/TPP and Rh/CHDPP catalysts.* Industrial & Engineering Chemistry Research, 2008. **47**(13): p. 4317-4324.

100. Leeuwen, P.W.N.M.v., *Homogeneous catalysis : understanding the art*. 2004, Dordrecht ; Boston: Kluwer Academic Publishers. xiii, 407 p.

101. Fersht, A., *Structure and mechanism in protein science : a guide to enzyme catalysis and protein folding*. 1999, New York: W.H. Freeman. xxi, 631 p.

102. Serizawa, A., Z.P. Feng and Z. Kawara, *Two-phase flow in microchannels.* Experimental Thermal and Fluid Science, 2002. **26**(6-7): p. 703-714.

103. Hessel, V., *Micro process engineering : a comprehensive handbook*. 2009, Weinheim: Wiley-VCH.

104. Garstecki, P., M.J. Fuerstman, H.A. Stone and G.M. Whitesides, *Formation of droplets and bubbles in a microfluidic T-junction - scaling and mechanism of break-up.* Lab on a Chip, 2006. **6**(3): p. 437-446.

105. van Steijn, V., M.T. Kreutzer and C.R. Kleijn, *mu-PIV study of the formation of segmented flow in microfluidic T-junctions.* Chemical Engineering Science, 2007. **62**(24): p. 7505-7514.

106. Fries, D. and P.R. von Rohr, *Impact of inlet design on mass transfer in gas-liquid rectangular microchannels.* Microfluidics and Nanofluidics, 2009. **6**(1): p. 27-35.

107. van Steijn, V., C.R. Kleijn and M.T. Kreutzer, *Predictive model for the size of bubbles and droplets created in microfluidic T-junctions.* Lab on a Chip, 2010. **10**(19).

108. Muradoglu, M. and H.A. Stone, *Motion of large bubbles in curved channels.* Journal of Fluid Mechanics, 2007. **570**: p. 455-466.

109. Kreutzer, M.T., A. Gunther and K.F. Jensen, *Sample dispersion for segmented flow in microchannels with rectangular cross section.* Analytical Chemistry, 2008. **80**(5): p. 1558-1567.

110. Galbiati, L. and P. Andreini, *Flow Pattern Transition for Horizontal Air-water Flow in Capillary Tubes - a Microgravity Equivalent System Simulation.* International Communications in Heat and Mass Transfer, 1994. **21**(4): p. 461-468.

111. Burriel, P., J. Claret, J. Ignes-Mullol and F. Sagues, *"Bottleneck effect" in two-dimensional microfluidics.* Physical Review Letters, 2008. **100**(13).

112. Reinecke, N. and D. Mewes, *Oscillatory transient two-phase flows in single channels with reference to monolithic catalyst supports.* International Journal of Multiphase Flow, 1999. **25**(6-7): p. 1373-1393.

113. Khan, S.A. and K.F. Jensen, *Oscillatory Bubbling in a Microfluidic T-Junction*, in *Micro Total Analysis Systems 2007*. 2007, Springer: New York. p. 952-953.

114. Oztaskin, M.C., M. Worner and H.S. Soyhan, *Numerical investigation of the stability of bubble train flow in a square minichannel.* Physics of Fluids, 2009. **21**(4).

115. Thulasidas, T.C., M.A. Abraham and R.L. Cerro, *Flow patterns in liquid slugs during bubble-train flow inside capillaries.* Chemical Engineering Science, 1997. **52**(17): p. 2947-2962.

116. van Baten, J.M. and R. Krishna, *CFD simulations of mass transfer from Taylor bubbles rising in circular capillaries.* Chemical Engineering Science, 2004. **59**(12): p. 2535-2545.

117. Yue, J., L.G. Luo, Y. Gonthier, G.W. Chen and Q. Yuan, *An experimental study of air-water Taylor flow and mass transfer inside square microchannels.* Chemical Engineering Science, 2009. **64**(16): p. 3697-3708.

118. Marton, C.H., *An Air-Breathing, Portable Thermoelectric Power Generator Based on a Microfabricated Silicon Combustor*, in *Massachusetts Institute of Technology. Dept. of Chemical Engineering.* 2010. p. 247 p.

119. Ajmera, S.K., C. Delattre, M.A. Schmidt and K.F. Jensen, *Microfabricated cross-flow chemical reactor for catalyst testing.* Sensors and Actuators B-Chemical, 2002. **82**(2-3): p. 297-306.

120. Losey, M.W., M.A. Schmidt and K.F. Jensen, *Microfabricated multiphase packed-bed reactors: Characterization of mass transfer and reactions.* Industrial & Engineering Chemistry Research, 2001. **40**(12): p. 2555-2562.

121. Perry, R.H. and D.W. Green, *Perry's chemical engineers' handbook*. 8th ed. 2008, New York: McGraw-Hill. 1 v. (various pagings).

122. Wada, Y., M.A. Schmidt and K.F. Jensen, *Flow distribution and ozonolysis in gas-liquid multichannel microreactors.* Industrial & Engineering Chemistry Research, 2006. **45**(24): p. 8036-8042.

123. Sutera, S.P. and R. Skalak, *The History of Poiseuille Law.* Annual Review of Fluid Mechanics, 1993. **25**: p. 1-19.

124. Benkrid, K., S. Rode and N. Midoux, *Prediction of pressure drop and liquid saturation in trickle-bed reactors operated in high interaction regimes.* Chemical Engineering Science, 1997. **52**(21-22): p. 4021-4032.

125. AlDahhan, M.H., F. Larachi, M.P. Dudukovic and A. Laurent, *High-pressure trickle-bed reactors: A review.* Industrial & Engineering Chemistry Research, 1997. **36**(8): p. 3292-3314.

126. Kipp, D.O., *Metal Material Data Sheets*, MatWeb - Division of Automation Creation, Inc.

127. Kipp, D.O., *Plastic Material Data Sheets*, MatWeb - Division of Automation Creation, Inc.

128. O'Brien, M., N. Taylor, A. Polyzos, I.R. Baxendale and S.V. Ley, *Hydrogenation in flow: Homogeneous and heterogeneous catalysis using Teflon AF-2400 to effect gas-liquid contact at elevated pressure.* Chemical Science. **2**(7): p. 1250-1257.

129. Griffiths, P.R. and J.A. De Haseth, *Fourier transform infrared spectrometry*. Chemical analysis v. 83. 1986, New York: Wiley. xv, 656 p.

130. Cornils, B. and W.A. Herrmann, *Applied homogeneous catalysis with organometallic compounds : a comprehensive handbook in three volumes*. 2nd, completely rev. and enlarged ed. 2002, Weinheim: Wiley-VCH. 3 v. (xliii, 1450 p.).

131. Evans, D., J.A. Osborn and G. Wilkinson, *Hydroformylation of alkenes by use of rhodium complex catalysts.* J. Chem. Soc. A, 1968(12): p. 3133-42.

132. Leeuwen, P.W.N.M.v. and C. Claver, *Rhodium catalyzed hydroformylation*. 2000, Dordrecht [Netherlands] ; Boston: Kluwer Academic Publishers. xii, 284 p.

133. Dieguez, M., C. Claver, A.M. Masdeu-Bulto, A. Ruiz, P. van Leeuwen and G.C. Schoemaker, *High-pressure infrared studies of rhodium complexes containing thiolate bridge ligands under hydroformylation conditions.* Organometallics, 1999. **18**(11): p. 2107-2115.

134. Cavalieri, d.O.P., L. Raimondi, G. Pagani, G. Montrasi, G. Gregorio and A. Andreetta, *Propene hydroformylation with rhodium carbonyls and triphenylphosphine. II. Kinetics of butyraldehyde formation.* Chim. Ind. (Milan), 1980. **62**(7-8): p. 572-9.

135. Bhanage, B.M., S.S. Divekar, R.M. Deshpande and R.V. Chaudhari, *Kinetics of hydroformylation of 1-dodecene using homogeneous HRh(CO)(PPh(3))(3) catalyst.* Journal of Molecular Catalysis a-Chemical, 1997. **115**(2): p. 247-257.

136. Deshpande, R.M. and R.V. Chaudhari, *Kinetics of Hydroformylation of 1-Hexene Using Homogeneous* *$HRh(CO)(PPh_3)_3$* *Complex Catalyst.* Industrial & Engineering Chemistry Research, 1988. **27**(11): p. 1996-2002.

137. Divekar, S.S., R.M. Deshpande and R.V. Chaudhari, *Kinetics of Hydroformylation of 1-Decene Using Homogeneous* *$HRh(CO)(PPh_3)_3$* *Catalyst - A Molecular-Level Approach.* Catalysis Letters, 1993. **21**(1-2): p. 191-200.

138. Nair, V.S., S.P. Mathew and R.V. Chaudhari, *Kinetics of hydroformylation of styrene using homogeneous rhodium complex catalyst.* Journal of Molecular Catalysis a-Chemical, 1999. **143**(1-3): p. 99-110.

139. Rosales, M., G. Chacon, A. Gonzalez, I. Pacheco, P.J. Baricelli and L.G. Melean, *Kinetics and mechanisms of homogeneous catalytic reactions Part 9. Hydroformylation of 1-hexene catalyzed by a rhodium system containing a tridentated phosphine.* Journal of Molecular Catalysis a-Chemical, 2008. **287**(1-2): p. 110-114.

140. Deshpande, R.M., B.M. Bhanage, S.S. Divekar and R.V. Chaudhari, *Solvent Effects in Hydroformylation of 1-Octene Using* *$HRh(CO)(PPh_3)_3$* *- Effect of* *PPh_3* *Addition on the Rate of Reaction.* Journal of Molecular Catalysis, 1993. **78**(3): p. L37-L40.

141. Caporali, M., P. Frediani, A. Salvini and G. Laurenczy, *In situ high pressure FT-IR spectroscopy on alkene hydroformylation catalysed by* $RhH(CO)(PPh_3)_3$ *and* $Co_2(CO)_8$. Inorganica Chimica Acta, 2004. **357**(15): p. 4537-4543.

142. Sparta, M., K.J. Borve and V.R. Jensen, *Activity of rhodium-catalyzed hydroformylation: Added insight and predictions from theory.* Journal of the American Chemical Society, 2007. **129**: p. 8487-8499.

143. Kamer, P.C.J., A. van Rooy, G.C. Schoemaker and P. van Leeuwen, *In situ mechanistic studies in rhodium catalyzed hydroformylation of alkenes.* Coordination Chemistry Reviews, 2004. **248**(21-24): p. 2409-2424.

144. Van, R.A., B.J.N.H. de, K.F. Roobeek, P.C.J. Kamer and L.P.W.N.M. Van, *Rhodium-catalyzed hydroformylation of branched 1-alkenes; bulky phosphite vs. triphenylphosphine as modifying ligand.* J. Organomet. Chem., 1996. **507**(1-2): p. 69-73.

145. Vanrooy, A., E.N. Orij, P.C.J. Kamer and P. Vanleeuwen, *Hydroformylation with a Rhodium/Bulky Phosphite Modified Catalyst. A Comparison of the Catalyst Behavior for Oct-1-ene, Cyclohexene, and Styrene.* Organometallics, 1995. **14**(1): p. 34-43.

146. Rosales, M., A. Gonzalez, Y. Guerrero, I. Pacheco and R.A. Sanchez-Delgado, *Kinetics and mechanisms of homogeneous catalytic reactions Part 6. Hydroformylation of 1-hexlene by use of Rh(acac)(CO)(2)/dppe dppe=1,2-bis(diphenylphosphino)ethane as the precatalyst.* Journal of Molecular Catalysis a-Chemical, 2007. **270**(1-2): p. 241-249.

147. Decker, S.A. and T.R. Cundari, *DFT study of the ethylene hydroformylation catalytic cycle employing a HRh(PH3)(2)(CO) model catalyst.* Organometallics, 2001. **20**(13): p. 2827-2841.

148. Deshpande, R.M., S.S. Divekar, B.M. Bhanage and R.V. Chaudhari, *Effect of Solvent on the Kinetics of Hydroformylation of 1-Hexene Using* $HRh(CO)(PPh_3)_3$ *Catalyst.* Journal of Molecular Catalysis, 1992. **77**(2): p. L13-L17.

149. Murzin, D.Y., A. Bernas and T. Salmi, *Kinetic modelling of regioselectivity in alkenes hydroformylation over rhodium.* Journal of Molecular Catalysis a-Chemical, 2010. **315**(2): p. 148-154.

150. Kiss, G., E.J. Mozeleski, K.C. Nadler, E. VanDriessche and C. DeRoover, *Hydroformylation of ethene with triphenylphosphine modified rhodium catalyst: kinetic and mechanistic studies.* Journal of Molecular Catalysis A: Chemical, 1999. **138**(2-3): p. 155-176.

151. Hershman, A., K.K. Robinson, J.H. Craddock and J.F. Roth, *Continuous Propylene Hydroformylation in a Gas-Sparged Reactor.* Product R&D, 1969. **8**(4): p. 372-375.

152. Kastrup, R.V., J.S. Merola and A.A. Oswald, *P-31 NMR Studies of Equilibria and Ligand Exchange in Triphenylphosphine Rhodium Complex and Related Chelated Bisphosphine Rhodium Complex Hydroformylation Catalyst Systems*, in *Catalytic Aspects of Metal Phosphine Complexes*. 1982, AMERICAN CHEMICAL SOCIETY. p. 43-64.

153. Bhanage, B.M., S.S. Divekar, R.M. Deshpande and R.V. Chaudhari, *Kinetics of hydroformylation of 1-dodecene using homogeneous* $HRh(CO)(PPh_3)_3$ *catalyst.* Journal of Molecular Catalysis a-Chemical, 1997. **115**(2): p. 247-257.

154. Csontos, G., B. Heil and L. Markó, *Hydroformylation of Olefins with Rhodium Carbonyls as Catalysts. IV. Mechanism of the Reaction.* Annals of the New York Academy of Sciences, 1974. **239**(1): p. 47-54.

155. Jauregui-Haza, U.J., E.J. Pardillo-Fontdevila, A.M. Wilhelm and H. Delmas, *Solubility of hydrogen and carbon monoxide in water and some organic solvents.* Latin American Applied Research, 2004. **34**(2): p. 71-74.

156. Snijder, E.D., M. Riele, G.F. Versteeg and W.P.M. Vanswaaij, *Diffusion-Coefficients of CO,* CO_2*,* N_2O*, and* N_2 *in Ethanol and Toluene.* Journal of Chemical and Engineering Data, 1995. **40**(1): p. 37-39.

157. van der Slot, S.C., P.C.J. Kamer, P. van Leeuwen, J.A. Iggo and B.T. Heaton, *Mechanistic studies of the hydroformylation of 1-alkenes using a monodentate phosphorus diamide ligand.* Organometallics, 2001. **20**(3): p. 430-441.

158. Chiusoli, G.P. and P.M. Maitlis, *Metal-catalysis in industrial organic processes*. 2006, Cambridge: Royal Society of Chemistry (Great Britain),. xx, 290 p.

159. Roessler, F., *Catalysis in the industrial production of pharmaceuticals and fine chemicals.* Chimia, 1996. **50**(3): p. 106-109.

160. Bull, S.R., *The United States Department of Energy Biofuels Research Program.* Energy Sources, 1991. **13**(4): p. 433-442.

161. Veldsink, J.W., M.J. Bouma, N.H. Schoon and A. Beenackers, *Heterogeneous hydrogenation of vegetable oils: A literature review.* Catalysis Reviews-Science and Engineering, 1997. **39**(3): p. 253-318.

162. Yaws, C.L., *Chemical Properties Handbook*. 1999, McGraw-Hill.

163. Horiuti, I. and M. Polanyi, *Exchange reactions of hydrogen on metallic catalysts.* Transactions of the Faraday Society, 1934. **30**: p. 1164-1172.

164. Somorjai, G.A., *Introduction to surface chemistry and catalysis*. 1994, New York: Wiley. xxiv, 667 p.

165. Johnson Matthey. *The Catalyst Technical Handbook*. [PDF] 2008 [cited 2011 June 26]; Available from: http://www.jmcatalysts.com/pharma/pdfs-handbooks/CatalystHandbookUSA.pdf.

166. Barrett, W.T., *Process of Preparing a Silica-Alumina-Platinum Catalyst*. 1958, W R Grace & Co: United States.

167. Losey, M.W., *Novel multiphase chemical reaction systems enabled by microfabrication technology*, in *Dept. of Chemical Engineering.* 2001, Massachusetts Institute of Technology. p. 251 leaves.

168. McDaniel, M.P. and T.D. Hottovy, *Total Porosity of High-Pore-Volume Silicas by Liquid Adsorption.* Journal of Colloid and Interface Science, 1980. **78**(1): p. 31-36.

169. Madon, R.J., J.P. Oconnell and M. Boudart, *Catalytic hydrogenation of cyclohexene: Part II. Liquid phase reaction on supported platinum in a gradientless slurry reactor.* Aiche Journal, 1978. **24**(5): p. 904-911.

170. Price, R.H. and D.B. Schiewetz, *Catalytic Liquid-Phase Hydrogenation.* Industrial and Engineering Chemistry, 1957. **49**(5): p. 807-813.

171. Ertl, G., H. Knoezinger and J. Weitkamp, *Handbook of heterogeneous catalysis*. 1997, Weinheim: Wiley-VCH. 5 v. ([lxxii], 2479 p.).

172. Anderson, J.R. and K.C. Pratt, *Introduction to characterization and testing of catalysts*. 1985, Sydney ; Orlando: Academic Press. ix, 457 p.

173. Muetterties, E.L., M.C. Tsai and S.R. Kelemen, *Chemistry of acetylene on platinum (111) and (100) surfaces.* Proceedings of the National Academy of Sciences of the United States of America-Physical Sciences, 1981. **78**(11): p. 6571-6575.

174. Marsh, A.L. and G.A. Somorjai, *Structure, reactivity, and mobility of carbonaceous overlayers during olefin hydrogenation on platinum and rhodium single crystal surfaces.* Topics in Catalysis, 2005. **34**(1-4): p. 121-128.

175. Rioux, R.M., B.B. Hsu, M.E. Grass, H. Song and G.A. Somorjai, *Influence of Particle Size on Reaction Selectivity in Cyclohexene Hydrogenation and Dehydrogenation over Silica-Supported Monodisperse Pt Particles.* Catalysis Letters, 2008. **126**(1-2): p. 10-19.

176. Thomas, C.L., *Chemistry of Cracking Catalysts.* Industrial & Engineering Chemistry, 1949. **41**(11): p. 2564-2573.

177. Rousseau, R.W., *Handbook of separation process technology*. 1987, New York: J. Wiley. xvi, 1010 p.

178. Sporka, K., J. Hanika, V. Ruzicka and M. Halousek, *Diffusion of Gases in Liquids .3. Diffusion Coefficients of Hydrogen in Organic Solvents.* Collection of Czechoslovak Chemical Communications, 1971. **36**(6): p. 2130-&.

Appendix A. Microfabrication

All fabrication was carried out in the Microsystem Technology Laboratory (MTL) at MIT. The fabrication processes required for this thesis are described in detail below. The machine name corresponds to the naming conventions employed in MTL. The color code describes the process contamination level, with green indicating metal-free processing and red indicating metal-contaminated processing. All required masks are also provided and are to scale. The masks contain rotated reactors to ensure that no channels are aligned with the crystal plane. The wafer flat is aligned with edge of the mask containing the text "MIT." Stress concentrates at the corners of channel, which makes the wafer more likely to crack along the crystal plane. Two separate processes are presented below differing in how many masks are required. The homogeneous reactor was constructed using a two mask design, while the three phase reactor required three masks.

Homogeneous Reactor Process

Project Name: DRIE Nitride Microreactor

Process Lead: **Jerry Keybl (keybl)**
Previously Approved for Users: Ryan Hartman, Kevin Nagy

General process: DRIE etch of a DSP wafer followed by a through etch from the back-side to provide inlet and outlet connections. Once the etching is complete, the nitride mask is removed and fresh nitride is deposited. A pyrex wafer is anodically bonded to the frontside to form the reactor. Individual devices are finally die-sawed.

Starting material:
6-inch Double Side Polished Silicon Wafer with 2000 A low-stress nitride from the VTR tube
1 mm thick, 6-inch Pyrex Wafer

	FAC	MACHINE	ACTION	NOTES	CODE
1			***Photolithography for DRIE -Step 1***		
1.0	TRL	AcidHood	Piranha clean before processing		🟩
1.1	TRL	HMDS	Coat wafer with HMDS program 3		🟩
1.2	TRL	coater	Spin Coat photoresist 10 µm AZ 9260	Static dispense, 60 s spread at 2000 RPM, 8 s spin at 3000 RPM	🟩
1.3	TRL	prebake	Bake at 95°C for 60 minutes		🟩
1.4	TRL	EV1	Expose resist for 15 seconds, 3 times with 15 sec interval	Mask 1	🟩
1.5	TRL	photowet-1	Development, 3min		🟩
1.6	TRL	postbake	Bake at 95°C for 30 minutes		🟩
			Pattern Nitride with RIE		
1.7	ICL	LAM490	Etch nitride		🟩
			DRIE - Step-1		
1.8	TRL	STS-2	Etch using JBETCH recipe for 400 um	Approx rate ~2.5 um/min	🟩
1.9	TRL	AcidHood-1	Piranha clean to remove photoresist		🟩
2			***Photolithography for DRIE -step-2***		
2.1	TRL	HMDS	Coat wafer with HMDS program 3		🟩
2.2	TRL	coater	Spin Coat photoresist 10 µm AZ 9260	Static dispense, 60 s spread at 2000 RPM, 8 s spin at 3000 RPM	🟩
2.3	TRL	prebake	Bake at 95°C for 60 minutes		🟩
2.4	TRL	EV1	Expose resist for 15 seconds, 3 times with 15 sec interval	Mask 2	🟩
2.5	TRL	photowet-1	Development, 3min		🟩
2.6	TRL	postbake	Bake at 95°C for 30 minutes		🟩
			Pattern Nitride with DRIE		
2.7	ICL	LAM490	Etch nitride		🟩
			DRIE-Step-2		
2.8	TRL	coater	Coat silicon handle wafer with thin resist in ring shape patterns	Handle wafer attachment	🟩
2.9	TRL	prebake	Attach handle wafer and bake for 30 minutes		🟩
2.10	TRL	STS-2	Etch using JBETCH recipe for 250 um	Through etch	🟩
2.11	TRL	Solvent Hood	Acetone rinse to separate wafers	~1 hr	🟩
2.12	TRL	AcidHood-1	Piranha clean		🟩
2.13	TRL	Asher	O2 plasma	Post STS clean	🟩
2.14	TRL	AcidHood-1	Piranha clean		🟩
3			***Nitride Removal***		
3.1	TRL	AcidHood-1	Conc HF to remove all nitride	1000 A per 20 min	🟩

				Nitride Deposition		
	3.2	TRL	RCA	RCA clean		🟩
	3.3	ICL	VTR	Deposit 5000 A low stress nitride		
4				***Bonding and Die-Saw***		
	4.1	TRL	AcidHood-1	Nanostrip pyrex wafer and process wafer		🟥
	4.2	TRL	EV501	Bond silicon and pyrex wafers	1000 V at 450 C for 15 min	
	4.3	ICL	Die-saw	Die-saw to get individual devices		

Mask 1 – Frontside (negative)

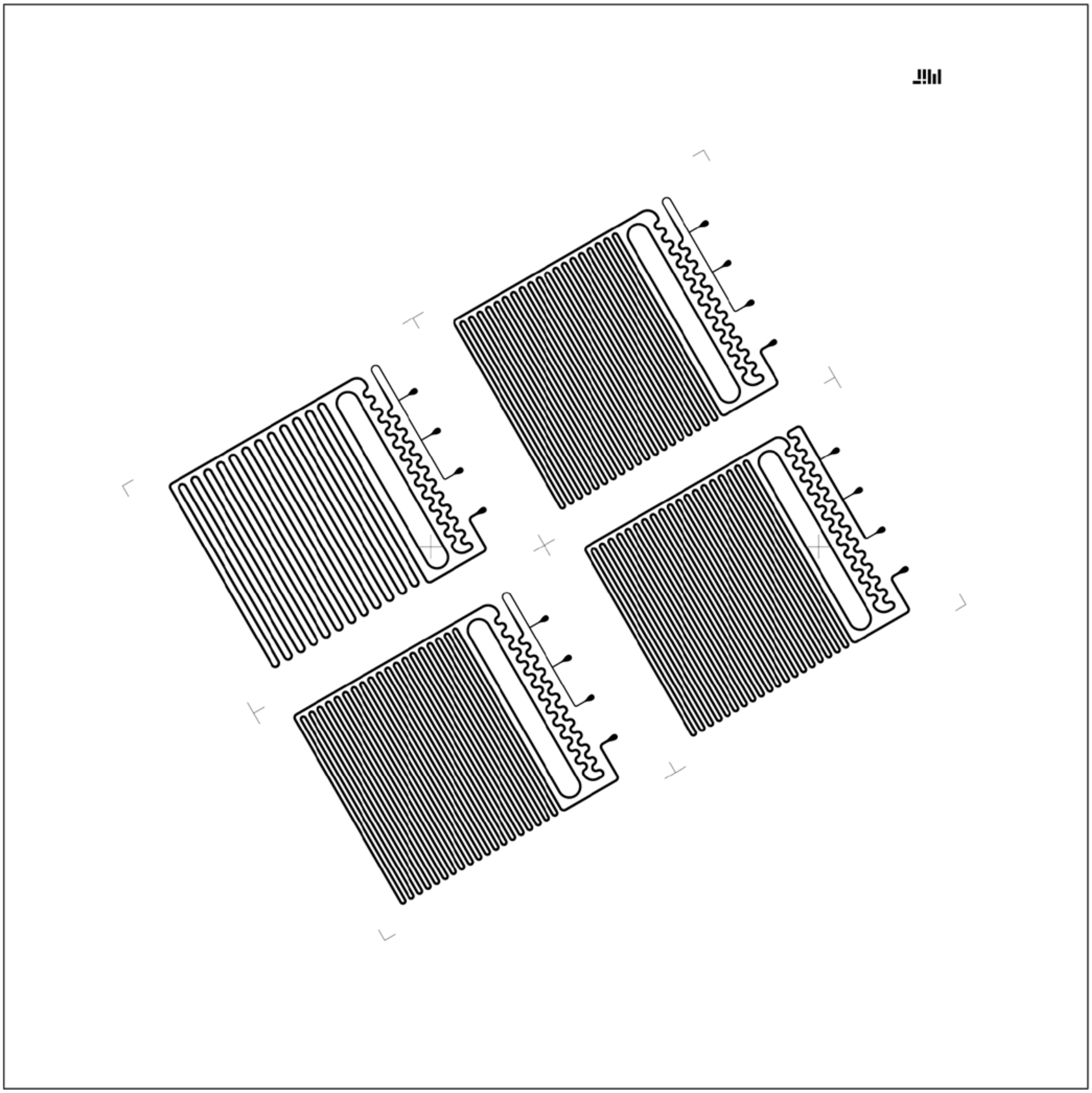

Mask 2 – Backside (negative)

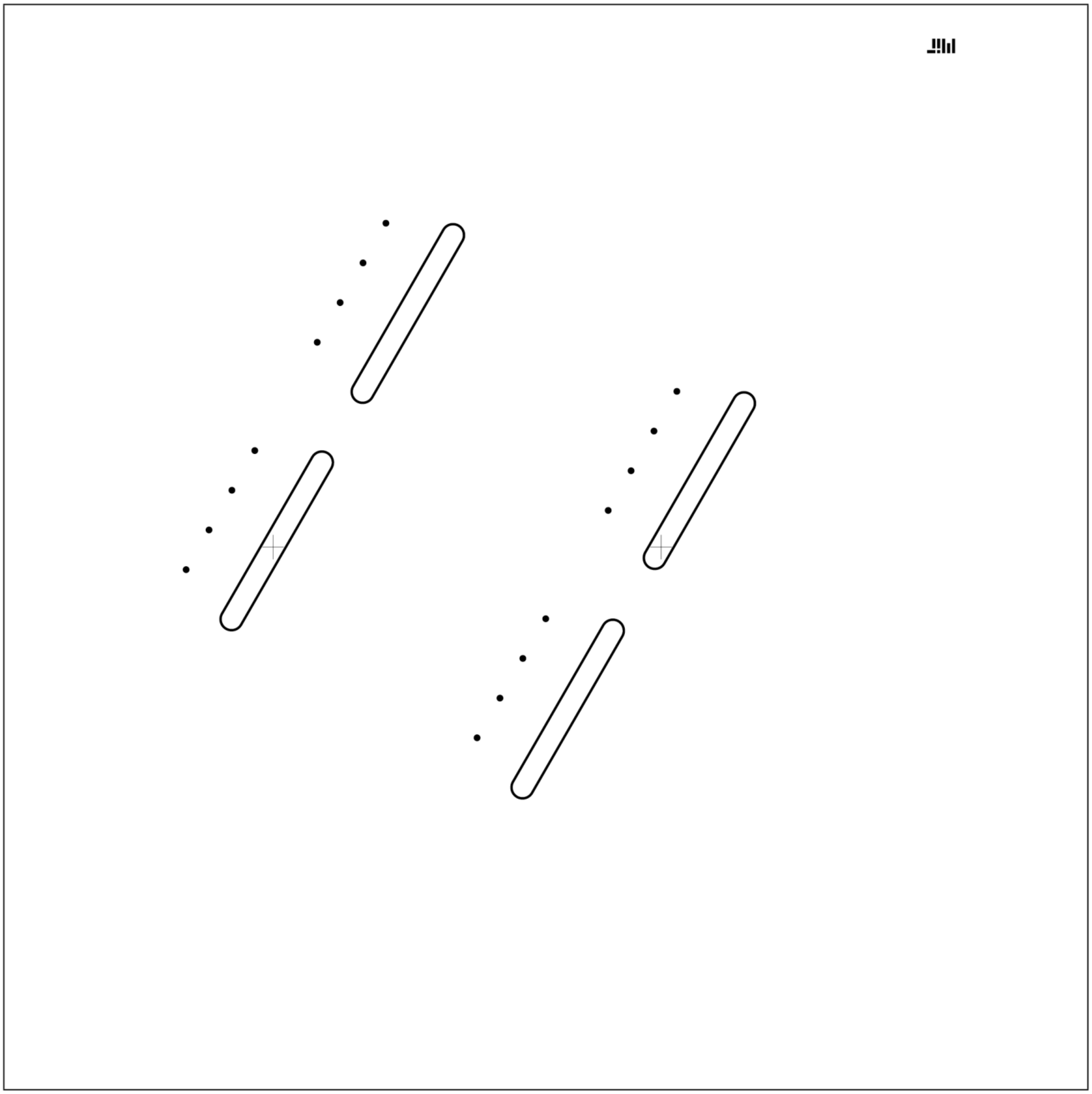

Heterogeneous Reactor Process

Project Name: Three Phase Heterogeneous Microreactor

Process Lead: **Jerry Keybl (keybl)**
Previously Approved for Users:

General process: Three mask DRIE etch of a SSP wafer followed by a through etch from the back-side to provide inlet and outlet connections. A pyrex wafer is anodically bonded to the frontside to form the reactor. Individual devices are die-sawed.

Starting material: 6-inch Single Side Polished Silicon Wafer
1 mm thick, 6-inch Pyrex Wafer

		FAC	MACHINE	ACTION	NOTES	CODE
1				***Photolithography for DRIE -Step 1***		
	1.0	TRL	AcidHood	Piranha clean before processing		🟩
	1.1	TRL	HMDS	Coat wafer with HMDS program for thin resist		
	1.2	TRL	coater	Spin Coat photoresist 1 µm thin resist	Follow Procedure on Posting near coater	
	1.3	TRL	prebake	Bake at 95°C		
	1.4	TRL	EV1	Expose resist for 1.5x Recipe	Mask 1 (MIT is always visible on surface of exposed wafers)	
	1.5	TRL	photowet-1	Development	Check to make sure 10 um features are fully developed	
	1.6	TRL	postbake	Bake at 95°C		
				DRIE - Step-1		
	1.7	TRL	STS-2	Etch using JBETCH recipe for 10 um	Took approx 2.5 min for this shallow etch	🟩
	1.8	TRL	AcidHood-1	Piranha clean to remove photoresist		
2				***Photolithography for DRIE -step-2***		
	2.1	TRL	HMDS	Coat wafer with HMDS program 3		🟩
	2.2	TRL	coater	Spin Coat photoresist 10 µm AZ 9260	2000 RPM, 8 s spin at 3000 RPM	
	2.3	TRL	prebake	Bake at 95°C for 60 minutes		
	2.4	TRL	EV1	Expose resist for 15 seconds, 3 times with 15 sec interval	Mask 2, frontside	
	2.5	TRL	photowet-1	Development, 3min		
	2.6	TRL	postbake	Bake at 95°C for 30 minutes		
				DRIE - Step-2		
	2.7	TRL	STS-2	Etch using JBETCH recipe for 400 um	Took approx 2.5 min for this shallow etch	🟩
	2.8	TRL	AcidHood-1	Piranha clean to remove photoresist		
3				***Photolithography for DRIE -step-3***		
	3.1	TRL	HMDS	Coat wafer with HMDS program 3		🟩
	3.2	TRL	coater	Spin Coat photoresist 10 µm AZ 9260	Static dispense, 60 s spread at 2000 RPM, 8 s spin at 3000 RPM	
	3.3	TRL	prebake	Bake at 95°C for 60 minutes		
	3.4	TRL	EV1	Expose resist for 15 seconds, 3 times with 15 sec interval	Mask 3, backside	
	3.5	TRL	photowet-1	Development, 3min		
	3.6	TRL	postbake	Bake at 95°C for 30 minutes		
				DRIE-Step-3		
	3.7	TRL	coater	Coat silicon handle wafer with thin resist in ring shape patterns	Handle wafer attachment	🟩

	3.8	TRL	prebake	Attach handle wafer and bake for 30 minutes		🟩
	3.9	TRL	STS-2	Etch using JBETCH recipe for 250 um	Through etch	
	3.10	TRL	Solvent Hood	Acetone rinse to separate wafers	~1 hr	
	3.11	TRL	AcidHood-1	Piranha clean	Post STS clean	
	3.12	TRL	Asher	O2 plasma		
4				***Bonding and Die-Saw***		
	4.1	TRL	AcidHood-1	Piranha pyrex wafer and process wafer		🟥
	4.2	TRL	EV501	Bond silicon and pyrex wafers	1000 V at 450 C for 15 min	
	4.3	ICL	Die-saw	Die-saw to get individual devices		

Mask 1 – Frontside 1 (negative)

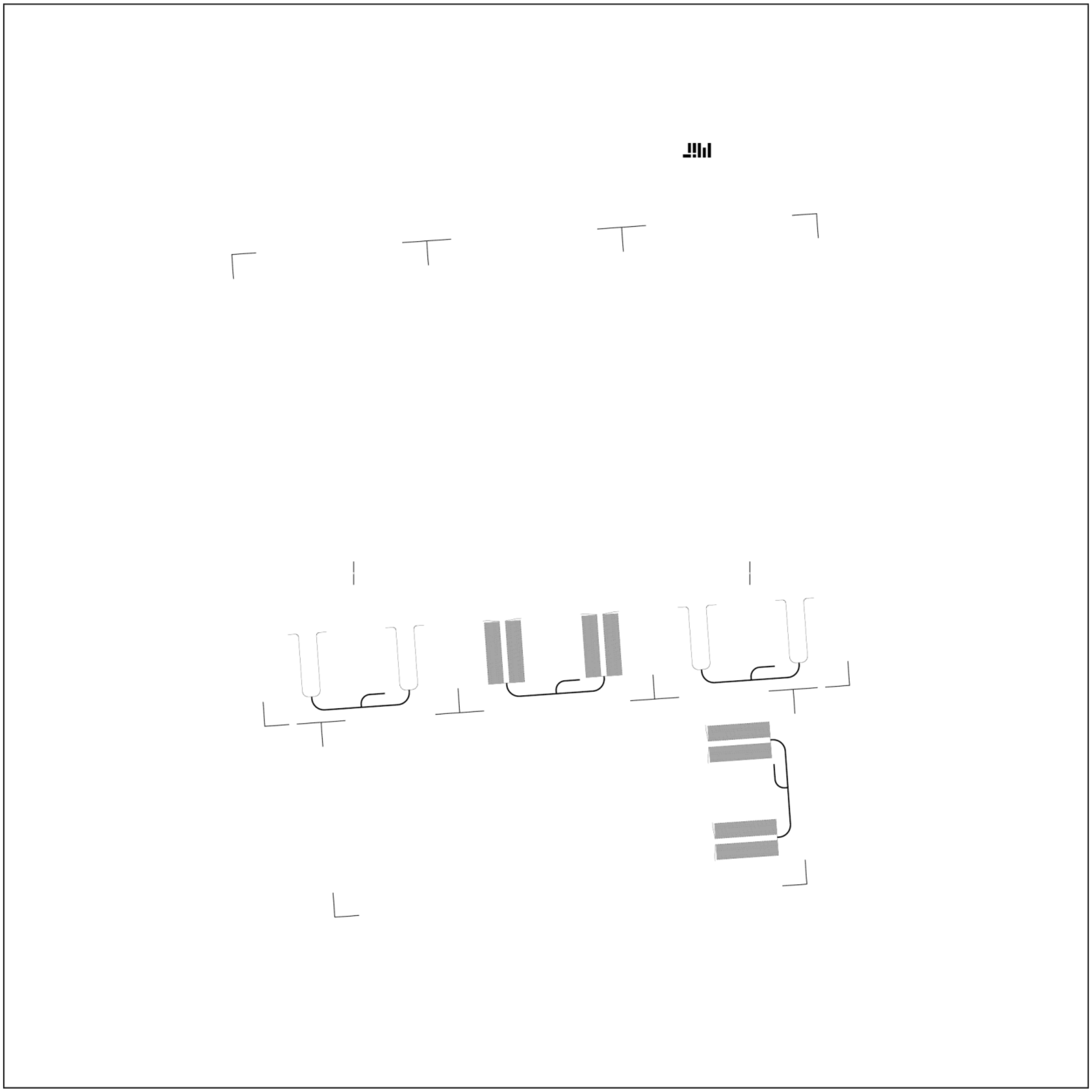

Mask 2 – Frontside 2 (negative)

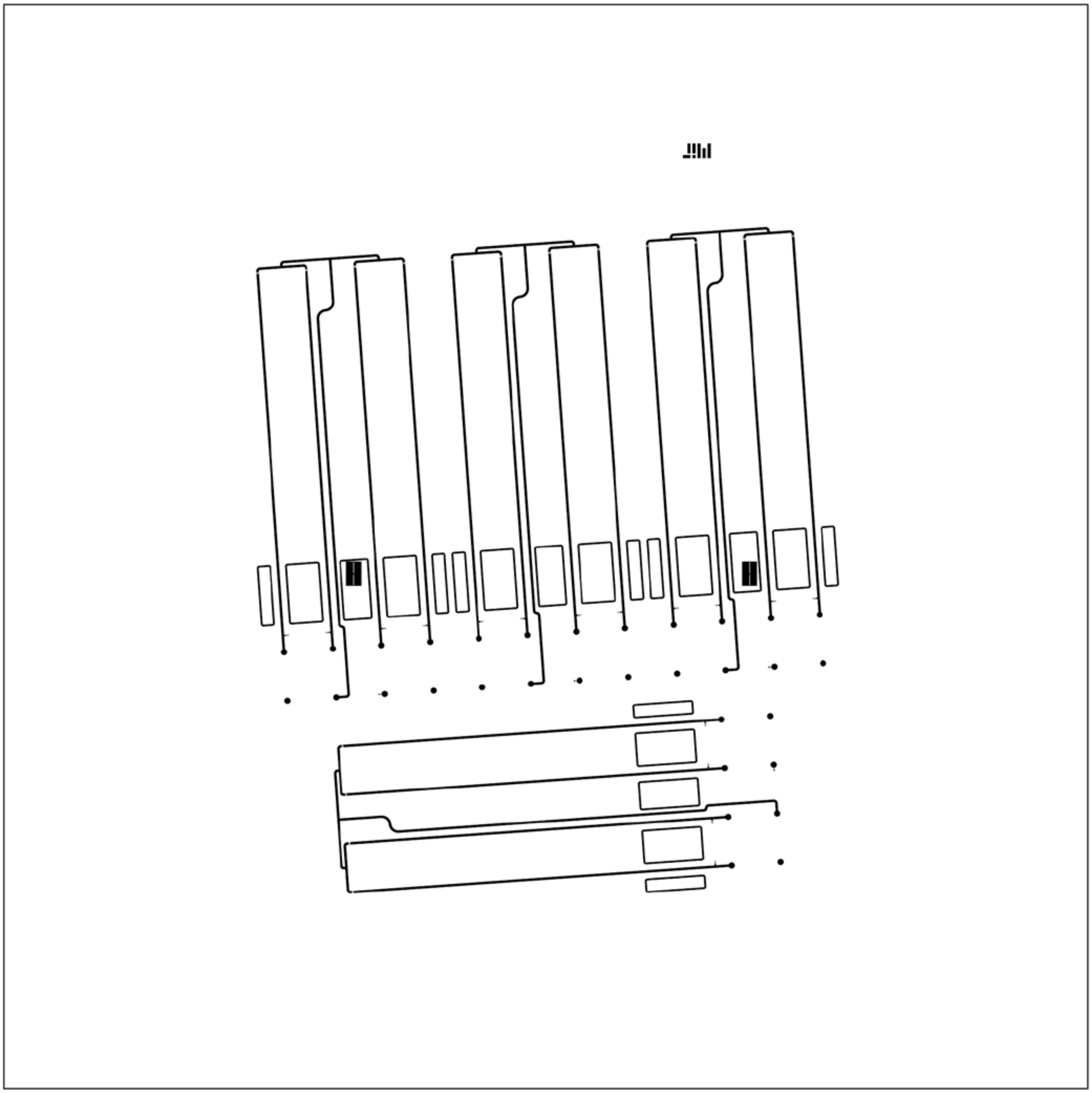

Mask 3 – Backside (negative)